FIELD AND EXPERIMENTAL INVESTIGATION OF

ATMOSPHERIC AEROSOL PROCESSES

A Dissertation

by

WILMARIE MARRERO-ORTIZ

Submitted to the Office of Graduate and Professional Studies of
Texas A&M University
in partial fulfillment of the requirements for the degree of

DOCTOR OF PHILOSOPHY

Chair of Committee,   Renyi Zhang
Co-Chair of Committee, Simon W. North
Committee Members,   Sarbajit Banerjee
                         Donald R. Collins
Head of Department,   Simon W. North

May 2018

Major Subject: Chemistry

ABSTRACT

Atmospheric aerosols profoundly impact human health, visibility, the ecosystem, and the climate. Some aerosols are directly emitted, but a majority are formed in the atmosphere by the oxidation of gaseous precursors. However, there are considerable uncertainties concerning the aerosol formation, transformation, and properties at the molecular level.

In my doctoral research, a series of laboratory measurements were conducted to investigate scientific questions, including the relation between the ambient aerosol mass concentration and light extinction, the sulfate formation under polluted environments, the light-absorption by organic aerosols under aqueous environments, the aerosol reactivity in surface reactions, and the aerosol physicochemical properties. To investigate them a series of analytical techniques were used in several scales.

For the field study, the aerosol mass concentration and aerosol light extinction were chemically apportioned with the carbonaceous aerosols being the dominant species for both. Moreover, due to the high concentration of ammonium cations relative to nitrate and sulfate anions, the low visibility, and the high relative humidity, chamber experiments were conducted to study the sulfate formation by mimicking the polluted conditions in China. It turns out that the secondary inorganic sulfate is formed by the oxidation of sulfur dioxide by nitrogen dioxide under aqueous phase. Additionally, under aqueous phase, secondary organic aerosols could be formed as showed by the bulk mixtures of α-dicarbonyls and amines model, which subsequently alter the optical properties. Furthermore, the uptake of gaseous amines and solid organic diacids reactions is studied

using a flow reactor. The results reveal that this type of heterogeneous reactions is driven by an interplay between the steric effect and the acidity/basicity strength of both the diacids and the amines.

Overall, the results indicate that atmospheric processes can efficiently alter the chemical composition, and the physical and optical properties. Detailed discussion and the further implications to the air quality and climate are presented in this dissertation. Reducing the gap in knowledge on the atmospheric aerosol process has significant implications for the development and improvement of climate-related policies and risk assessments worldwide.

DEDICATION

To my parents for their unconditional help and support.

ACKNOWLEDGEMENTS

I would like to acknowledge my research advisor Dr. Renyi Zhang for his guidance and opportunities that he provided during my graduate studies. Also, I want to thank my committee co-chair and former graduate advisor Dr. Simon W. North for his support, as well as the other committee members Dr. Donald R. Collins and Dr. Sarbajit Banerjee. Moreover, I would like to thank Dr. Min Hu, as well as her students, for hosting me in Peking University to collect data for my dissertation.

I want to thank my labmates, past and present, from who I have learned so much during this journey. Special thanks to Mario Gomez and Jeremiah Secrest for teaching me so many things related to the lab. Also, thanks to Misti Levy Zamora and Guo Song who assisted me during the broader analysis in my research and for making the field campaign an enjoyable time. Moreover, I appreciated the departmental office staff from the Departments of Chemistry and Atmospheric Sciences at Texas A&M University for helping with my academic and non-academic inquiries.

I want to express my gratitude to the Office of Graduate and Professional Studies. I have been able to participate in so many helpful programs during my graduate studies; without them, I would not know if I could get here. Thanks for administering my graduate fellowships (Diversity, NSF-LSAMP-BTD, and NSF-GRFP), helping to develop a community of amazing peers, and for providing professional developments opportunities (AGEP program, G.R.A.D Aggies, Close The Gap Program, etc.).

Finally, I appreciated all of my academic and personal mentors, as well as the ones who work inside and outside Texas A&M. Externally, I want to thank Dr. Guerrero-

CONTRIBUTORS AND FUNDING SOURCES

Contributors

This work was supervised by a dissertation committee consisting of Professor Renyi Zhang (chair), Professor Simon W. North (co-chair), and Professor Sarbajit Banerjee from the Department of Chemistry, as well as Professor Donald R. Collins from the Department of Atmospheric Sciences.

The data in Chapter II, and part of the Chapter III and IV was collected in Peking University in collaboration with Professor Min Hu, from the College of Environmental Sciences and Engineering, and her team Zhuofei Du, Jing Zheng, Guo Song, Tianyi Tan, and Tiantian Wang. In Chapter II the Mixing Layer Height data was provided by Dr. Zirui Liu and Dr. Guiqian Tang from the Institute of Atmospheric Physics, Chinese Academy of Sciences in Beijing, China. In Chapter III, the field and chamber data were processed with helped from Misti Levy Zamora and Mario Gomez, respectively. The results from this chapter were published in collaboration with Professor Gehui Wang from the Institute of Earth Environment, Chinese Academy of Science in Xi'an, China. In Chapter IV, part of the optical properties and chemical composition were performed in collaboration with Zhuofei Du (PAX), Guo Song (density), Yujue Wang (Orbitrap), Mario Gomez (TD-ID-CIMS), and Yun Lin (Mie Theory). For Chapter V, training was provided by Mario Gomez, Brittany Turner and Jeremiah Secrest; and discussion by Naruki Hiranuma.

All other work conducted for the dissertation was completed by the student independently.

Funding Sources

TABLE OF CONTENTS

LIST OF FIGURES

xiii

xiv

LIST OF TABLES

CHAPTER I

INTRODUCTION AND LITERATURE REVIEW

The world is changing at a fast pace. An increase in global population and redistribution to urban areas have led to an increase in energy and agricultural demands—that have, in turn, led to changes in emissions and have altered the composition of the atmosphere [*National Academies of Sciences and Medicine*, 2016]. These changes have provoked significant societal challenges including climate change and air pollution [*Jacob and Winner*, 2009]. The fifth Intergovernmental Panel on Climate Change (IPCC) Assessment Report states that climate change is happening and recognizes the dominant cause as human influence [*IPCC*, 2013]. Air pollution is a significant threat to human health, being responsible for one of eight deaths globally [*Fenger*, 2009].

Recently, to mitigate climate change and air pollution, there has been increased awareness of short-lived climate pollutants (SLCPs), such as black carbon, tropospheric ozone, methane, and hydrofluorocarbons. SLCPs may have a short lifetime relative to greenhouse gases, but they can contribute globally to warming and chronic illness [*Ramanathan and Feng*, 2009; *von Schneidemesser et al.*, 2015]. Taking measures to mitigate SLCP emissions can help achieve many of the Sustainable Development Goals (SDGs) proposed by the United Nations [*Haines et al.*, 2017]. To understand and respond to these environmental and societal challenges, atmospheric chemistry research is critical.

Atmospheric chemistry is concerned with describing the fundamental process that controls the chemical composition of the atmosphere, as well as how the chemical and physical properties of the atmosphere change due to human activities [*Heard and Saiz-*

Lopez, 2012]. Atmospheric chemistry research leads to discoveries about the air we breathe and environmental issues such as climate change, air pollution, photochemical smog, acidic deposition, stratospheric ozone depletion, biogeochemical cycles, etc. [*Abbatt et al.*, 2014; *Burkholder et al.*, 2017]. Moreover, atmospheric chemistry research findings have supported policy and diplomatic decisions that have significantly improved climate, human health, and welfare. For example, when the chemicals responsible for stratospheric ozone depletion became understood at a molecular level, they were banned under the Montreal Protocol, a diplomatic- scientific agreement.
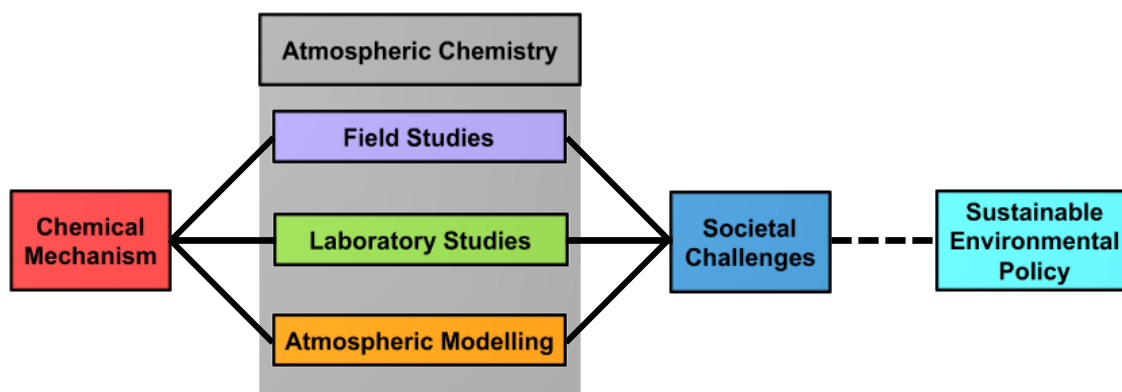
Figure 1: Schematic diagram connecting fundamental chemistry to different research approaches (branches) in the atmospheric chemistry field and to societal challenges and sustainable policy.

The atmospheric chemistry field combines knowledge from theory, laboratory experiments, field measurements, and atmospheric models to unify the understanding of the atmospheric chemical process. Therefore, a modified version of the traditional three-legged stool approach is presented in Figure 1 [*Abbatt et al.*, 2014]. The theory of chemical mechanisms underpins each branch (or stool leg), and the resulting branch combination

could help solve current societal challenges and establish sustainable environmental policies. This dissertation places particular emphasis on discussing field and laboratory studies.

Laboratory studies are an essential bridge between field measurements and models [*Burkholder et al.*, 2017]. Laboratory studies provide the techniques for field measurements and the parametrization inputs necessary for atmospheric models. However, laboratory studies are used to verify field observations and the mechanism used in models. Analogously, atmospheric models are mainly evaluated against field measurements.

During laboratory studies, several tools are used to simulate atmospheric chemical and physical transformation (aging) including chambers, bulk reactions, and flow reactors. These techniques allow chemical reactions to be made under a variety of timescales and conditions (e.g., temperature, humidity, light source, oxidant, and concentration). On one hand, chambers allow simulation of aging from hours to days, but they often are unable to achieve the degree of oxidation observed in the atmosphere. On the other hand, flow reactors could simulate the observed ambient aging within seconds or minutes by using a high concentration of oxidant (several orders of magnitude relative to ambient). Each method has its unique advantages and limitations regardless of the detailed mechanism and ambient representation, as shown in Figure 2. However, combining these tools leads to a better understanding of the formation mechanism and implications of atmospheric processes. Furthermore, the field of atmospheric chemistry is increasingly focused on much more complex chemical systems, like aerosols, than the comparatively simple gas-phase processes studied in the past [*Andreae and Crutzen*, 1997; *Burkholder et al.*, 2017; *Ravishankara*, 1997].
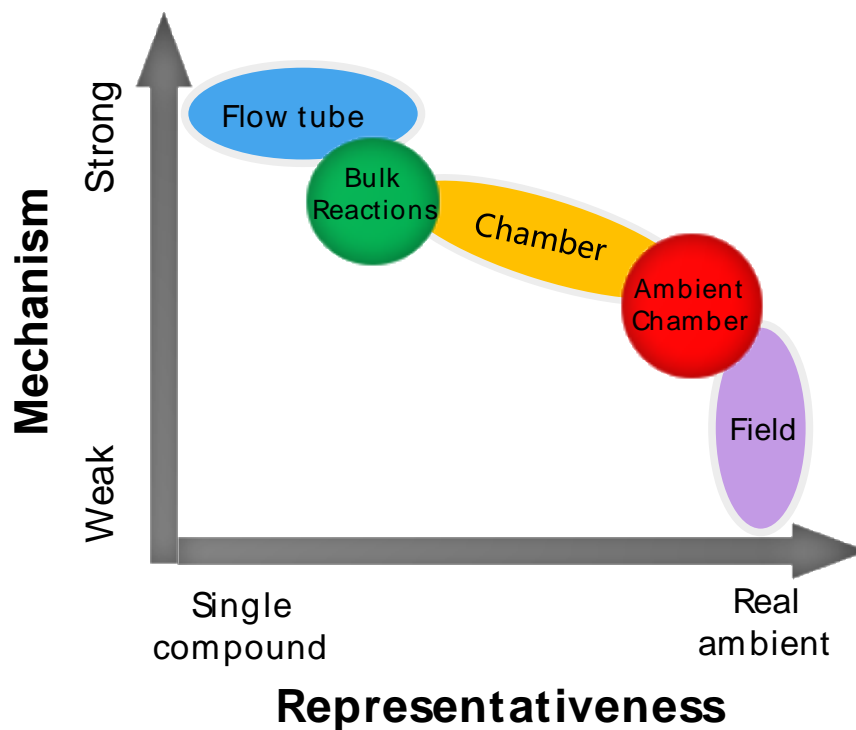
Figure 2: Two-dimensional representation of some experimental approaches currently used for chemical analyses of aerosols and their ambient representation.

Atmospheric aerosols are liquid or solid particles suspended in the air with diameters from 1 nm to 10 μm [*Finlayson-Pitts and Pitts Jr*, 2000; *Pöschl*, 2005; *Seinfeld and Pandis*, 2006]. Aerosols are formed by physical and chemical processes or are directly emitted into the atmosphere from both natural and anthropogenic sources [*Zhang et al.*, 2015b]. Due to their small size, they have little inertia and, as a consequence, may stay in the air for several days. Because of this lifetime, aerosols can undergo long-range transport and be transformed chemically via sunlight, cloud processing, and reactions, altering their physical properties [*IPCC*, 2013].

4

Depending on context, atmospheric aerosols are interchangeably called particles, atmospheric nanoparticles, and/or particulate matter (PM), as seen in this text. PM is used together with a description of aerosol size. For example, aerosols with diameters of less than 10 μm, 2.5 μm, and 1 μm are denoted by PM_{10}, $PM_{2.5}$, and PM_1, respectively. When referring to aerosols smaller than 0.5 μm, i.e., 500 nm, the term atmospheric nanoparticles is often used. Atmospheric aerosols influence the earth's radiative balance, impact cloud nucleation processes, reduce visibility, alter global biogeochemical cycles, reduce air quality, and negatively affect human health [*IPCC*, 2013; *McNeill*, 2017; *Pöschl*, 2005; *Zhang et al.*, 2015b].

Atmospheric aerosols have direct effects on public health from aggravating allergies to development of chronic diseases, to premature death [*Correia et al.*, 2013; *Gauderman et al.*, 2004; *Pope and Dockery*, 2006]. These effects are dependent on factors like particle size (whether particles can penetrate the lower airways of the human respiratory system), the intensity of the exposure, retention time of particles in the respiratory tract, the concentrations, the nature of the particles and their interaction with human tissue, and the presence/absence of pre-existing conditions, especially, diseases of the respiratory tract. Epidemiological and toxicological studies have been linked to a wide range of acute and chronic diseases, from increase morbidity and mortality, to respiratory, cardiovascular, reproductive, and mental health issues [*Burnett et al.*, 2014; *Drakaki et al.*, 2014; *Oudin et al.*, 2016; *Schlesinger et al.*, 2006; *Srám*, 1999]. Long-term exposure to aerosols in the most polluted urban areas has been linked to an increased risk of premature death and mortality from lung cancer [*Pope et al.*, 2002], a health risk comparable to long-term exposure to second-hand smoke [*Pope and Dockery*, 2006].

Moreover, aerosols play a critical role in climate—directly by scattering and absorbing solar radiation and indirectly through modifying cloud properties by acting as cloud condensation nuclei and ice nuclei, modulating photochemistry, promoting multiphase chemistry, altering the precipitation patterns and influencing the clouds' albedo [*Finlayson-Pitts and Pitts Jr*, 2000; *Seinfeld and Pandis*, 2006]. A recent study, using measurements and modelling techniques, shows that the aerosols, no matter the particle size, invigorated convective clouds [*Fan et al.*, 2018; *Rosenfeld et al.*, 2008]. Currently, aerosols' direct and indirect effects represent the largest uncertainty in climate predictions using global climate models [*Fan et al.*, 2007; *Fan et al.*, 2008]. A full understanding of aerosols and their role in the atmosphere requires a detailed physicochemical characterization.

Determining the chemical composition of ambient aerosols has been a great challenge for chemists [*Prather et al.*, 2008]. Depending on the source, the aerosol mass is composed of inorganic, biogenic, and chemically complex carbonaceous material [*Seinfeld and Pandis*, 2006]. The inorganic component consists mainly of sulfate, ammonium, nitrate, sodium, chloride, trace metals, and crustal elements [*Zhang et al.*, 2015b]. The carbonaceous fraction is mainly composed of black carbon (BC) aerosols and organic carbon aerosols (OCs or OAs). Secondary organic aerosols (SOAs), which are produced by chemical reactions, new particle formation, and gas-to-particle conversion of volatile organic compounds (VOCs) in the atmosphere, dominate the global OA burden [*Hallquist et al.*, 2009; *Kanakidou et al.*, 2005; *Shrivastava et al.*, 2017]. OAs represent a diversity of $10^4 - 10^5$ distinct compounds, and because of their chemical complexity, it is impossible to use a single analytical technique to identify all these compounds [*Nozière et al.*, 2015].

Recent technological advances, though, such as mass spectrometry [*Laskin et al.*, 2018], optical spectroscopy, and microscopy, [*Ault and Axson*, 2017] have allowed recognizing thousands of organic species, but only about 30% of OAs have been identified [*Andreae*, 2009].

The aerosols can undergo chemical reactions in the atmosphere via sunlight, cloud processing and reactions with gas phase species like oxidation and acid-base. The most important oxidants in the atmosphere are OH radicals, ozone (O_3), and nitrate (NO_3) radicals. Those chemical process could happen via gas-phase, multiphase (gas-liquid), and heterogeneous (gas-solid) reactions [*Finlayson-Pitts and Pitts Jr*, 2000; *Seinfeld and Pandis*, 2006]. Those reactions depend on the particle phase state, which can change with the relative humidity [*Kuwata and Martin*, 2012; *Shiraiwa et al.*, 2011; *Shiraiwa et al.*, 2017]. The mass transport of gasses and bulk phase diffusion can vary from seconds to years, depending if the particle is solid, semi-solid, or liquid [*Shiraiwa et al.*, 2012]. Additionally, the chemical transformation has an impact on the physical properties, which are not well understood [*Zhang et al.*, 2015b]. For example, when the organic material is oxidized, it becomes less volatile, more hygroscopic and alters the optical properties [*McNeill*, 2015; *Zhang et al.*, 2008].

Considering the ubiquity of OAs, understanding their optical properties is extremely important [*Moise et al.*, 2015]. The optical properties relevant to the aerosols include the scattering (b_{sca}) and absorption (b_{abs}) coefficients. They are expressed as a number proportional to the number of photons scattered or absorbed per unit distance (m^{-1}). The sum of both is equal to the extinction coefficient ($b_{ext} = b_{sca} + b_{abs}$). Scattering and absorption are determined by the particle size, structure, and chemical composition.

Typically, b_{sca}, b_{abs} and b_{ext} are normalize to the number particle concentration, giving the

scattering (C_{sca}), absorption (C_{abs}) and extinction (C_{ext}) cross sections (m^2). The mass

absorption cross section (MAC) is the b_{abs} normalize by the mass (m^2g^{-1}), which is

commonly used to quantify the light absorption of BC. Another parameter is the single

scattering albedo (SSA), the dimensionless ratio of the scattering to the extinction. A SSA

value of 1 indicates a purely scattering particle. A decrease in the SSA indicates an

increase in the absorption. An increase in the b_{ext} is related to a decrease in visibility

(Figure 3).

Figure 3: An example of visibility degradation due to the aerosol light extinction. The photo on the left was taken on a polluted day (PM$_{2.5}$ = 448 µg m^{-3}), and the photo on the right was taken on a clean day (PM$_{2.5}$ = 15 µg m^{-3}). The photos were taken on Peking University in Beijing, China during January 2015.

The absorption properties of carbonaceous aerosols have not been well

characterized. Light-absorbing carbonaceous aerosols include BC and brown carbon (BrC).

BC is produced by incomplete combustion and has the ability to absorb light over a broad

range of the solar spectrum [*Bond and Bergstrom*, 2006]. BrC, the light absorbing fraction

of OAs, exhibits enhanced light absorption at shorter wavelengths due to the presences of organic chromophores. Therefore, some OAs can be significant climate-forcing agents via its absorption optical properties [*Moise et al.*, 2015]. However, the overall contribution of SOA to BrC and the related climate forcing are poorly understood and are not currently included in atmospheric model studies. Additionally, the light extinction by OAs stabilize the atmosphere, leading to a negative impact on air quality and the inhibition of cloud formation [*Wang et al.*, 2013b]. Also, the chemical characterization of BrC has proven to be complex and therefore remains incomplete [*Laskin et al.*, 2015]. Such incomplete understanding is due in part to the chemical complexity of SOA, and the lack of clarity regarding SOA formation, transformation, and optical properties [*Hallquist et al.*, 2009].

The growing realization of the importance of OAs is making them a central research area in current atmospheric chemistry research. Given the large number and variability of chemical constituents, sources, and possible chemical transformations of OAs, a chemical characterization including reactivity, oxidation level, molecular weight, hygroscopicity, volatility, and optical properties presents a significant challenge for both experiments and models [*Jimenez et al.*, 2009; *Kroll et al.*, 2011]. The lack in understanding of the formation and transformation of aerosols hinder the development of predictive models and further mitigations. Reducing the gap in knowledge would improve atmospheric models and have significant implications for the development and enhancement of climate-related policies and risk assessments worldwide.

This dissertation explores different scientific questions by varying the scale of the experimental approach. Chapter II describes field measurements taken in the winter of 2015 in Beijing, China, with the purpose of investigating the optical properties and

formation mechanism of haze development episodes. Chapter III considers the heterogeneous aqueous conversion of sulfur dioxide to sulfate in polluted environments by coupling part of the field measurement data with new chamber experiments. The importance of the relative humidity (RH) and the role of aqueous reactions are discussed. Chapter IV presents a study on the formation of light-absorbing products by small α-dicarbonyls and amines under aqueous bulk reactions, focusing on optical properties and chemical composition. Chapter V examines the uptake and heterogeneous kinetics of gaseous amines on solid dicarboxylic acids using a flow reactor. A detailed discussion of the acid-base reaction and the multifunctional groups is provided. Lastly, Chapter VI presents an integrated summary of the findings and provides some perspective for future research directions.

CHAPTER II

MEASUREMENTS OF AEROSOL CHEMICAL AND OPTICAL PROPERTIES IN

BEIJING DURING WINTER 2015: A FIELD STUDY

Introduction

The poor air quality in China is linked with the rapid economic development [*Chan and Yao*, 2008; *Fang et al.*, 2009; *Zhang et al.*, 2013]. Recently, China has experienced severe haze pollution with fine particulate matter smaller than 2.5 µm ($PM_{2.5}$). The $PM_{2.5}$ had reached unprecedented high levels, exceeding the World Health Organization (WHO) limit of 10 µg m^{-3}. For example, the U.S. embassy in Beijing reported a $PM_{2.5}$ annual mean of 102 µg m^{-3} for 2013 [*U.S. Department of State*, 2018]. Furthermore, this pollution undergoes long-range transport across the Pacific Ocean into the western U.S., making it a global problem [*Lin et al.*, 2014]. In September 2013, the Chinese government stated that they will significantly improve the air quality by the end of 2017, and committed almost 300 billion USD to address it. Their goal is to reduce the annual average $PM_{2.5}$ mass concentrations in Beijing to 60 µg m^{-3} by 2017; by reducing coal consumption, updating vehicle fleet, and enforcing environmental laws, taxation and subsidies. Based on preliminary results from the early news report of this year 2018, the Chinese government accomplished their goal. Lie Baoxian, deputy director of the Beijing Municipal Environmental Monitoring Center, indicated that they reduced $PM_{2.5}$ levels by 35 %, i.e., from 90 µg m^{-3} in 2013 to 58 µg m^{-3} in 2017. The information is relatively consistent with the data from the U.S. embassy data in Beijing, which shows a $PM_{2.5}$ reduction of 31%,

i.e., from 102 μg m^{-3} in 2013 to 70 μg m^{-3} in 2017 (Figure 4) [*U.S. Department of State*, 2018].
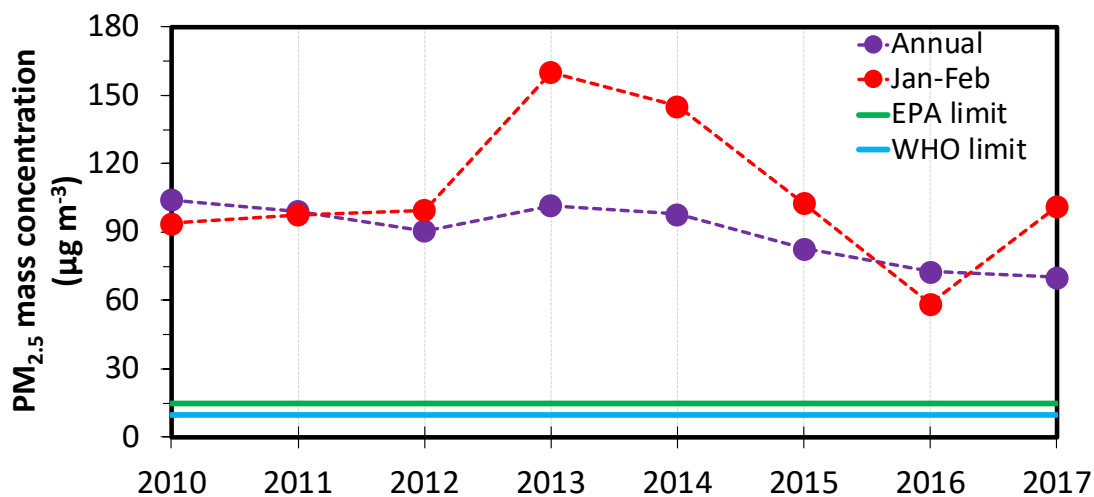
Figure 4: Comparison of the annual and winter PM$_{2.5}$ mass concentration between 2010 and 2017 in Beijing measured at the U.S. Embassy. For comparison, the green and blue line represent the average annual limits by the U.S. EPA and the WHO, respectively [U.S. Department of State, 2018].

However, the formation mechanisms leading to haze episodes remain uncertain. The abundance and chemical constituents of PM$_{2.5}$ vary considerably, depending on the meteorology, primary pollution sources, and secondary chemical processes [*Guo et al.*, 2014; *Huang et al.*, 2014; *Sun et al.*, 2013; *Zhang et al.*, 2017; *Zhang et al.*, 2015b; *Zheng et al.*, 2015]. The haze in Beijing occurs in all seasons, but with a higher frequency during the winter. Moreover, its formation mechanism is different from other well-known polluted regions, such as Houston, Los Angeles, and Mexico City, which typically exhibit a diurnal trend instead of the few days period observed in Beijing [*Zhang et al.*, 2015b]. Another remarkable distinction is the fast transition between clean to polluted conditions since the

12

PM$_{2.5}$ in China could easily increase over 100 μg m^{-3}, in less than 24 hours, which have not been observed in other urban regions [*Zhang et al.*, 2017; *Zhang et al.*, 2015b].

Most of the primary PM in China is emitted from road dust and combustion sources, such as emissions from vehicles, industries, coal and residential fuel combustion, biomass burning, and cooking [*Zhang et al.*, 2017]. However, secondary PM fraction dominates the fine PM, since primary PM contributes less than 50% of the total PM for all seasons [*Guo et al.*, 2013]. The major precursors for secondary PM are volatile organic compounds (VOCs), nitrogen oxides (NO$_x$), sulfur dioxide (SO$_2$), and ammonia (NH$_3$) [*Zhang et al.*, 2015b]. Their sources in urban areas are mainly from anthropogenic origins, except the VOCs and NH$_3$ which could vary depending on the season.

The secondary PM formation process often occurs by aerosol nucleation and subsequent growth with a periodic cycle of 4 to 7 days [*Guo et al.*, 2014]. New particle formation (NPF) events are usually comprised of three phases. First the aerosol nucleation process, which leads to a rapid increase in the particle number concentration of small particles (<20 nm); second the aerosol growth, where the particles increase their size due to condensation of gaseous species; third the decrease in particle number concentration due to coagulation and dilution [*Guo et al.*, 2014]. Gaseous sulfuric acid and organic vapors have been shown to play an essential role in the nucleation process [*Wang et al.*, 2015; *Wang et al.*, 2011; *Yue et al.*, 2010]. NPF events occur frequently, and during all seasons in Beijing, however, most of the studies have been conducted during the summer and autumn, while not many during the winter, remembering that meteorological conditions drive the pollution episodes in Beijing [*Wang et al.*, 2017b; *Wu et al.*, 2007; *Zheng et al.*, 2015].

The physical and chemical properties of PM can provide crucial information on the primary emission, atmospheric evolution, and environmental implications [*Zhang et al.*, 2015b]. For example, the chemical composition provides information about the primary and secondary aerosol sources; the effective density distinguishes between fresh primary and aged aerosol; the hygroscopicity reveals the aerosol potential to serve as a CCN; the optical properties suggest the aerosols ability to alter the visibility, radiative budget, and climate forcing. It is important to note that the aerosol properties are commonly interrelated. In Beijing during the autumn season, Guo et al. [*Guo et al.*, 2014] show that during the transition from a clean to a polluted period, the contribution from organics decreases (from 75% to 38%) and the secondary inorganics increases (from 25% to 62%). Similarly, the effective density and hygroscopicity increase from clean to polluted period, indicating the formation of an internal mixture of secondary species more hydrophilic [*Guo et al.*, 2014]. Likewise, Lee et al. [*Lee et al.*, 2007] observed an increase in the light extinction in polluted periods relative to clean.

The chemical composition of PM has been widely reported; however, the optical properties of PM are rarely explored in Beijing [*Tao et al.*, 2017]. There is an interplay between the PM chemical composition and its impact on aerosols optical properties [*Wang et al.*, 2006b]. For example, the light extinction is controlled not only by the mass concentration, but also by the chemical composition, size distribution, and hygroscopicity [*Cao et al.*, 2012; *Ma et al.*, 2012; *Meier et al.*, 2009]. Moreover, the light extinction could be apportioned using the mass concentration of the chemical species into the IMPROVE (Interagency Monitoring of Protected Visual Environments) model [*Malm and Hand*, 2007; *Pitchford et al.*, 2007]. A detailed understanding of the aerosol optical properties,

14

scattering, and absorption, could reveal the potential impact of the haze on the visibility and direct climate forcing [*Andreae and Ramanathan*, 2013; *Moise et al.*, 2015; *Wang et al.*, 2013b]. A collaboration between Texas A&M University (TAMU) and Peking University (PKU) was established to conduct ambient measurements of aerosol properties (chemical and optical) in Beijing, China during the winter of 2015.

Methodology

Ambient measurements were conducted on the campus of Peking University (PKU, 39°59'21" N, 116°18'25' E), located in northwestern Beijing, from January 20th to February 4th, 2015. The site is representative of an urban area which is heavily influenced by mobile sources, such as vehicles (a major highway is located 200 m east of the measurement site), with no significant stationary sources [*Wu et al.*, 2008]. A suite of instruments, located in an air-conditioning room on the roof of a building about 15 m above ground level, was used simultaneously to measure several aerosol properties, such as mass concentrations, chemical composition, and optical properties. Moreover, the mixing layer height (MLH), as a surrogate of the planetary boundary layer (PBL), was retrieved by using a ceilometer and a radiosonde, and following the protocol by Tang et al. 2016.

For the ambient mass concentration, a Tapered Element Oscillating Microbalance (TEOM, 1400a, Thermo, USA) with a $PM_{2.5}$ cyclone inlet was used by introducing an ambient aerosol sampling flow of 1 LPM. The TEOM measures the mass collected on a filter by monitoring the corresponding frequency changes of a tapered element. The mass

concentration was determined from the change in the oscillation frequency. The tube's natural frequency of oscillation decreased as the mass concentration increased on the exchangeable filter.

The chemical composition of size-resolved submicron particles was detected by an Aerodyne High-Resolution Time-of-Flight Aerosol Mass Spectrometer (HR-ToF-AMS). The HR-ToF-AMS operates in 5 minutes cycles to obtain the mass concentration of non-refractory species such as organics, nitrate, sulfate, chloride, and ammonium. The instrument was calibrated at the beginning, middle and end of the measurements for inlet flow, ionization efficiency, and particle sizing as suggested in the protocol [*Hu et al.*, 2016]. The detection limits of the HR-ToF-AMS is determined by passing filtered ambient air through the system and measuring the species signals for three five-minute intervals. The detection limits were 0.033, 0.004, 0.008, 0.004, and 0.026 $\mu g\ m^{-3}$, for organics, nitrate, sulfate, chloride, and ammonium respectively. Additional details about the instrument are given by DeCarlo et al. [*DeCarlo et al.*, 2006].

The optical properties were measured using a Photoacoustic Extinctometer (PAX, Droplet Measurement Technologies) at 405, 532, and 870 nm. The PAX uses in-situ photoacoustic technology and reciprocal nephelometry to measure the particle absorption and scattering, respectively. In the absorption cell, a laser beam directed through the aerosol stream is modulated at the resonant frequency of the acoustic chamber. The energy absorbed by particles is thermally transferred to the surrounding air, and the subsequent air expansion produces a sound wave, which is recorded by a microphone. In the scattering cell, the standard nephelometer is used, but the locations of the light source and detectors are reversed. The instrument was calibrated with polystyrene latex spheres and Aquadag

soot particles. An ambient aerosol sampling flow of 1 LPM passed through a series of

Nafion driers (Perma Pure, Inc.) to reduce the relative humidity of the aerosols to less than

10% before passing by the PAX. Therefore, the instrument measured the dry aerosol

absorption and scattering coefficients. The extinction is calculated from the sum of the

absorption and scattering. Additionally, other instruments were used concurrently to

measure the black carbon (BC) mass concentration, such as the aethalometer, the multi-

angle absorption photometer (MAAP), and the single particle soot photometer (SP2). More

details about those instruments are provided by Moosmüller et al. [*Moosmüller et al.,* 2009].

The light extinction of ambient aerosols could be apportioned using the revised

IMPROVE model. IMPROVE relates the light-extinction to the mass concentration of

each component and its water uptake, as shown in equation 1, assuming externally mixed

aerosols. However, the water uptake functions are not taken into consideration in this study

since the measured optical properties are from the dry aerosols.

$$
\begin{aligned}
b_{ext}(550nm) \approx\ & 2.2 \times f_S(RH) \times [Small\ (NH_4)_2SO_4] \\
& + 4.8 \times f_L(RH) \times [Large\ (NH_4)_2SO_4] \\
& + 2.4 \times f_S(RH) \times [Small\ NH_4NO_3] \\
& + 5.1 \times f_L(RH) \times [Large\ NH_4NO_3] \\
& + 2.8 \times [Small\ Organics] + 6.1 \times [Large\ Organics] \\
& + 10 \times [Black\ Carbon] + 1.7 \times f_{SS}(RH) \times [Sea\ Salt] \\
& + 0.33[NO_2] \\
& + Rayleigh\ Scattering.
\end{aligned}
\tag{1}
$$

$$[Large\ X] = [Total\ X]^2/20\ ,for\ [Total\ X] < 20 \qquad (2)$$

$$[Large\ X] = [Total\ X]\ ,for\ [Total\ X] \geq 20 \qquad (3)$$

$$[Small\ X] = [Total\ X] - [Large\ X] \qquad (4)$$

Mass concentrations of each component were taken from the mass concentration measured by the HR-ToF-AMS and summarized in Table 1. A detailed description of the IMPROVE equation is given by Pitchford et. al. [*Pitchford et al.*, 2007]. Sulfate and nitrate are assumed to be fully neutralized with ammonium, and chloride to be a sea salt surrogate. The IMPROVE model suggests a concentration apportioned in small and large size modes (equation 2-4), with a threshold value of 20 μg m^{-3}. If the total concentration of a component exceeds this threshold, all of it is assumed to be in the large mode. Black Carbon (BC) concentration was determined from the absorption measured by the PAX 870 and divided by the MAC value of 4.74 m^2 g^{-1} [*Bond and Bergstrom*, 2006].

Table 1: PM variables proposed by IMPROVE

Component	Specification
Ammonium Sulfate, $(NH_4)_2SO_4$	$1.375[SO_4^{2-}]$
Ammonium Nitrate, NH_4NO_3	$1.29[NO_3^-]$
Organics	[organics]
Sea Salt	$1.8[Cl^-]$
EC	[BC]

Results and Discussion

During the measurement period, the $PM_{2.5}$ mass concentration, chemical composition and optical properties of ambient aerosols are analyzed to understand the haze formation mechanism and its implication in the optical properties. The $PM_{2.5}$ mass concentration time series is shown in Figure 5a, along with the chemical composition obtained from the HR-ToF-AMS. In the two-week period, four pollution cycle events are observed, and the dominant chemical constituents are organics (47%), nitrate (18%), sulfate (14%), chloride (2%), ammonium (13%) and black carbon (6%). The highest mass concentration observed was about 275 μg m^{-3}, which is considered hazardous according to the US Air Quality Index, but overall it is not as high as same months from previous years episodes. This decrease in mass concentration could be due to the implementation of new regulations and mitigation strategies. The pollution episodes could occur overnight or last for several days, depending on the meteorological conditions.

The meteorological conditions such as wind speed, wind direction, relative humidity, and planetary boundary layer (PBL) height could affect the length and severity of the haze events [*Guo et al.*, 2014]. Figure 5b shows the anticorrelation between the MLH and the $PM_{2.5}$ mass concentration. When the MLH is low, the vertical mixing decreases, trapping the PM and increasing the mass concentration. The MLH is at its maximum over noon time and could decrease by almost 1,500 m reaching its minimum around midnight. Therefore, it is not surprising that the highest concentrations were often observed around midnight when the MLH is compressed.
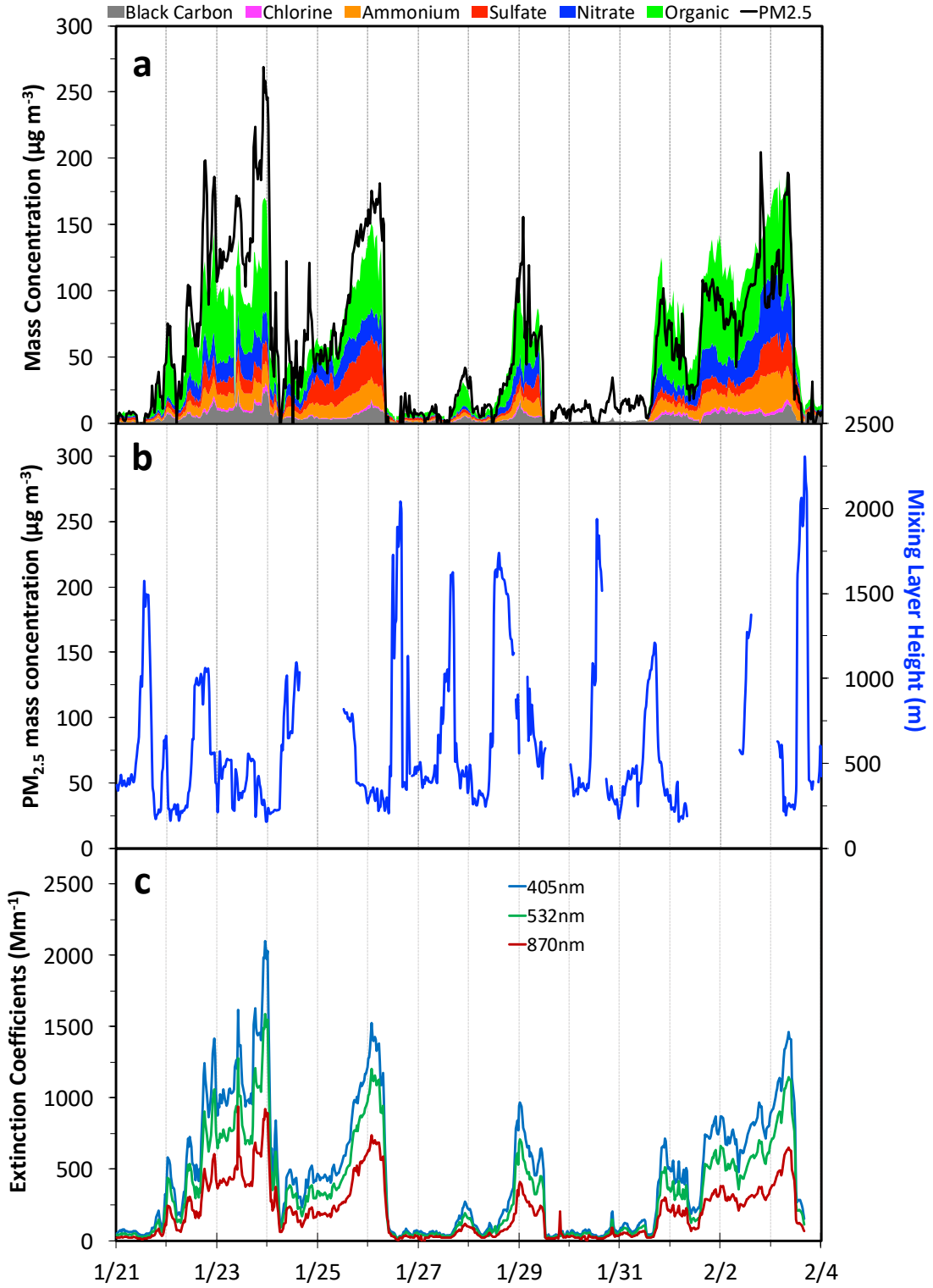
Figure 5: Time series of the PM2.5 with chemical composition (a), mixing layer height (b) and light extinction (c)

However, some days like January 23, the MLH remains low during the daytime, which in turn will compress the particles and increase the mass concentration.

The light extinction of the submicron particles is important because their particle size is close to the wavelength of the visible solar spectrum. Figure 5c shows a time series of the light extinction coefficient at three different wavelengths. The light extinction follows the same trend as $PM_{2.5}$ mass concentration, implying a proportional behavior. It is important to clarify that the extinction at 405 nm is for PM_1, while the 532 nm and 870 nm are for $PM_{2.5}$. Also, the light extinction is higher at 405 nm than 532 nm and 870 nm, indicating a higher sensitivity at shorter wavelengths. The light extinction could be decomposed into the scattering and the absorption fractions. In Figure 6 the contribution of the absorption and scattering to the extinction for each wavelength are shown, including the Single Scattering Albedo (SSA), which is the scattering divided by the extinction. The dominant contributor to the light extinction, with almost 80-90%, is the scattering component. Interestingly, the contribution of the absorption and the scattering remains relatively constant, even under haze events.
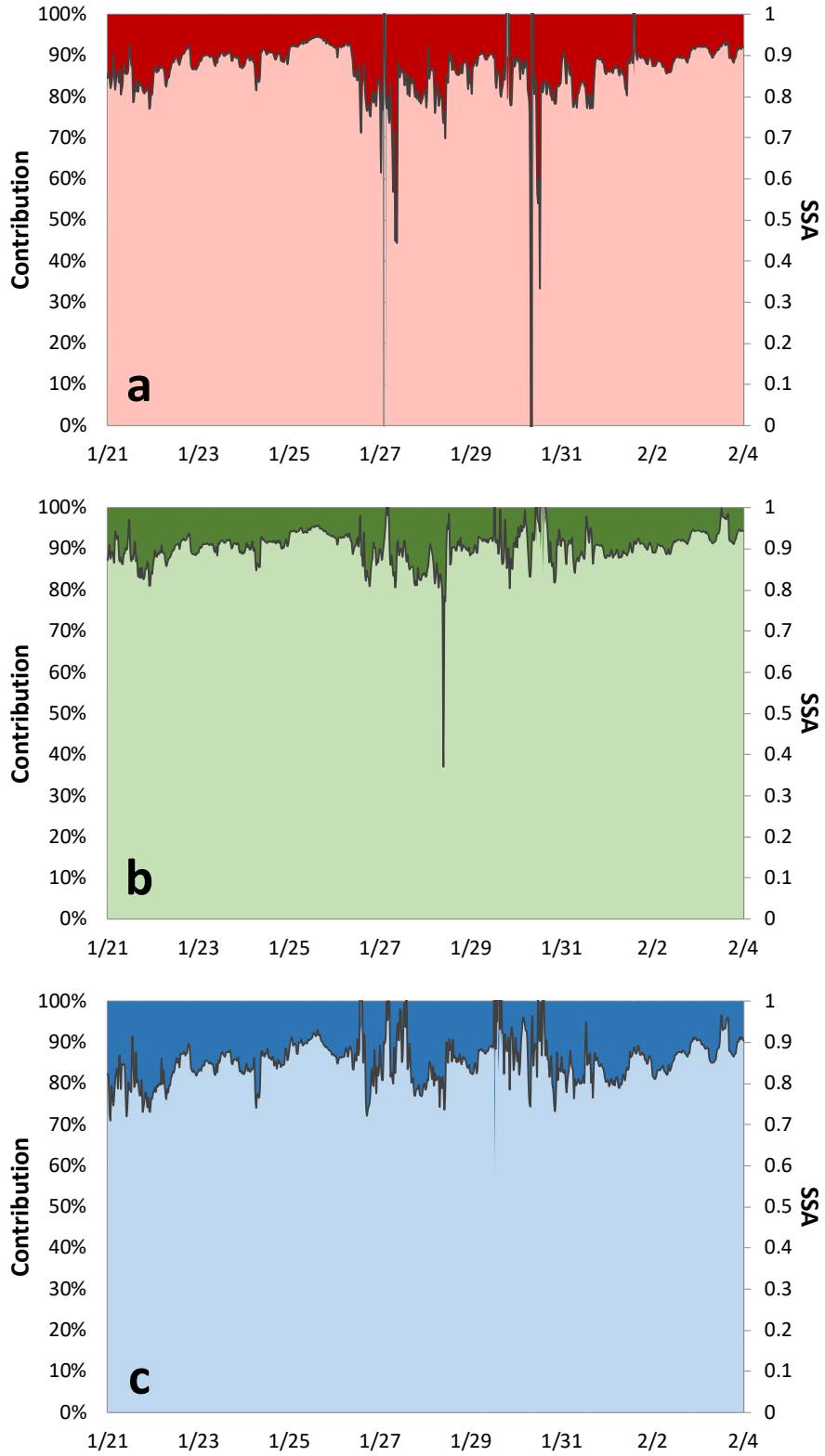
Figure 6: Time series of the scattering (clear) and absorption (dark) to the total light extinction for 870 nm (a), 532 nm (b), and 405 nm (c).
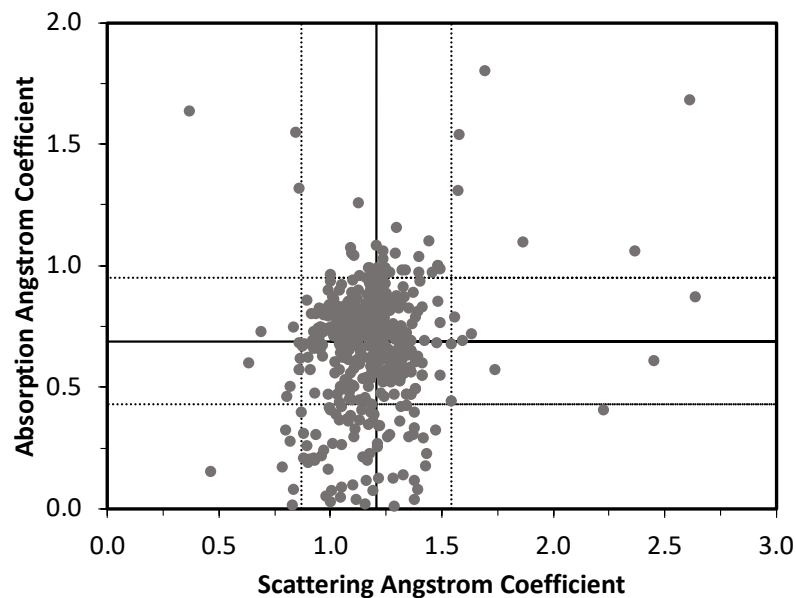
Figure 7: Comparison between the Absorption Angstrom coefficient (AAC) and the Scattering Angstrom coefficient (SAC) calculated in Beijing. The straight lines are the average and the dotted the standard deviation.

The angstrom coefficient is used to quantify the wavelength dependence of the absorption and scattering component. The scattering angstrom coefficient (SAC) is influenced by the particle size, while the absorption angstrom coefficient (AAC) depends more on the relative contribution of BC, BrC, and non-absorbing components. A comparison of the AAC and SAC is shown in Figure 7 using only 532 nm and 870 nm wavelengths. The straight lines are the average values of 0.69±0.26 and 1.21±0.34 for AAC and SAC, respectively. A significant deviation of the average values for SAC and AAC is not observed when comparing clean and polluted periods, which is consistent with the relative constant SSA for all wavelengths (Figure 6). The SAC values range from 0, for very large particles, to 4, for very small particles [*Zhu et al.*, 2015]. A SAC value higher than 1 suggests a dominance of anthropogenic fine particles. The AAC value is used to

23

identify non-BC contributors to the light absorption. In this study, the AAC values lower

than 1 indicate the abundance of BC coated and aged [*Bahadur et al.*, 2012]. Therefore, the

results indicated the contributors to the light extinction are from the anthropogenic

influence. Even though the AAC is lower than 1 [*Yuan et al.*, 2016], the estimation of the

BC mass concentration based on optical measurements (assuming 7.5 m^2g^{-1} at 550 nm with

AAC = 1) does not deviate from the values obtained by the SP_2 as shown in Figure 8. On

average, the Aethalometer slightly underestimates the BC mass concentration, while the

MAAP overestimate it.
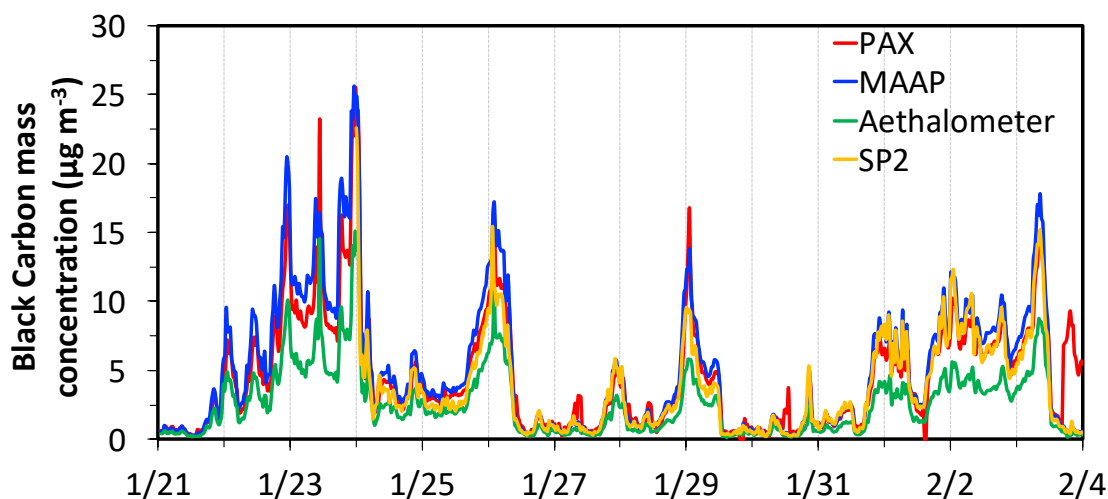
Figure 8: Times series of Black Carbon mass concentration obtained by different instruments.

The ratio of the light scattering and light absorption to the $PM_{2.5}$ mass

concentration represents the mass scattering coefficient (MSC) and the mass absorption

coefficient (MAC), respectively. The dry MSC and dry MAC at 532 nm wavelength, as a

24

function of the PM$_{2.5}$ mass concentration, is shown in Figure 9a. Each data point is the

average value for each 25 μg m^{-3} incremental interval. The average MSC and MAC values

are 5.35±1.40 and 0.55±0.16 m^2 g^{-1}, respectively. The MSC values slightly decrease with

the increase in the mass concentration. This contrasts with previous studies that had found

a direct correlation between the MSC and the mass concentration [*Jung et al.*, 2009]. The

MSC values obtained are within the ranges of the values typically observed in Chinese

urban areas (3.5 to 5.9 m^2 g^{-1}), being higher for the winter season and northern China [*Tao

et al.*, 2017]. The MAC decreases with an increase of the mass concentration until 150 μg

m^{-3}, when then the MAC value starts to increase [*Peng et al.*, 2016]. At the low mass

range, the large uncertainties in MSC and MAC is due to the extremely low light

extinction. Based on the MSC and MAC values we can calculate the SSA

[SSA=MSC/(MSC+MAC)] again. As presented in Figure 9b, the SSA as a function of the

mass concentration follows the opposite trend of the MAC. The SSA increases with the

mass concentration until 150 μg m^{-3} (same minimum as for MAC) and then starts

decreasing. A similar trend was observed by Jung et al., for PM$_{10}$. The average SSA value

is 0.91 which is higher than the values previously reported in Beijing.

The visual range (VR) parameter is used as a surrogate for the ambient visibility.

VR is estimated by using the 532 nm light extinction coefficient on the Koshmeider

equation (VR = -ln(0.02)/bext) [*Koschmieder*, 1924]. The VR decrease dramatically as the

mass concentration increases with a parametrization of VR = 593.65 × [PM$_{2.5}$]$^{-0.96}$ (Figure

10). The high VR is characterized by a low ambient RH and PM mass concentration lower

than 50 μg m^{-3}. Additionally, when the ambient relative humidity is higher than 35%, the

mass concentration is over 50 μg m^{-3} and with VR lower than 15 km. Those results are

similar to those previously reported in Beijing [*Chen et al.*, 2014; *Jung et al.*, 2009; *Zhang et al.*, 2010].
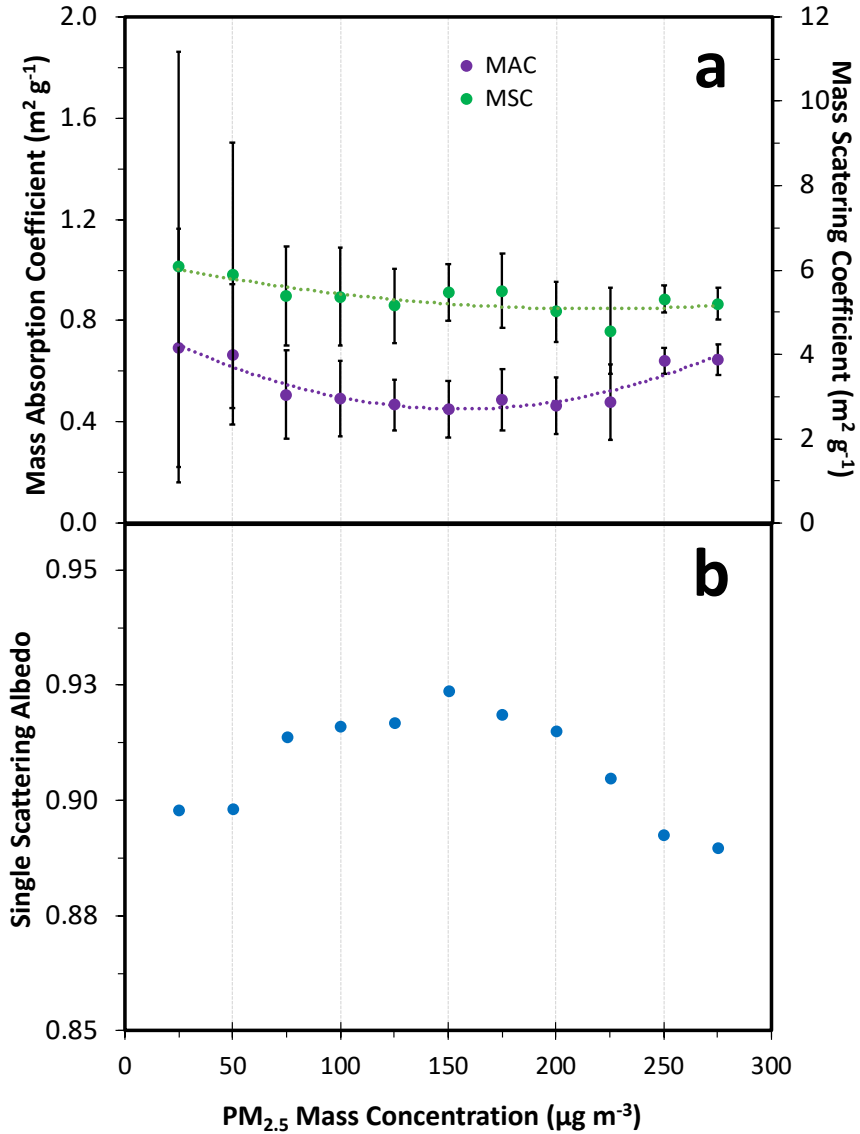
Figure 9: Optical properties as a function of the PM2.5 mass concentration. (a) Dry Mass Absorption Coefficient (MAC) and Dry Mass Scattering coefficient (MSC). (b) Single Scattering Albedo (SSA).
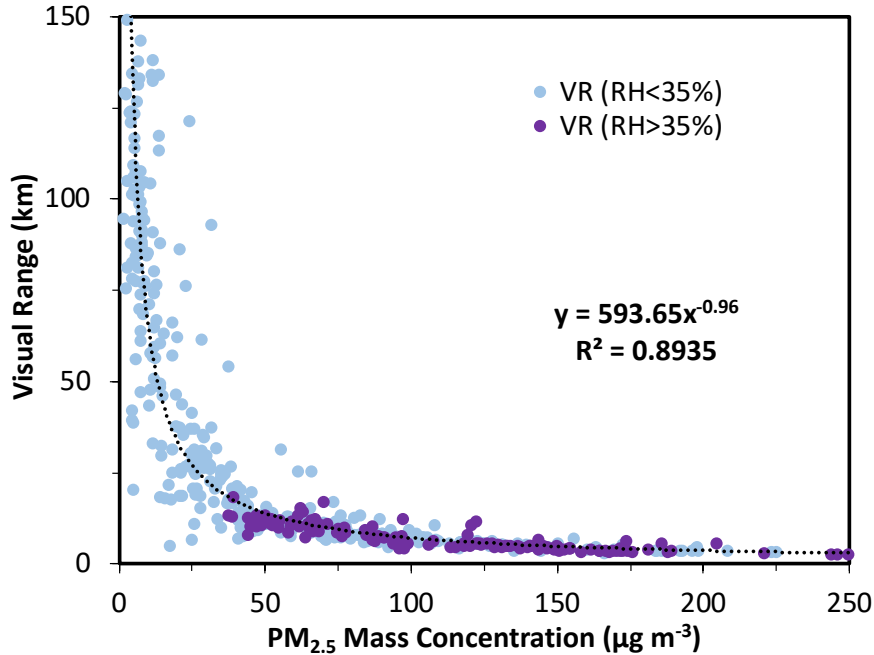
Figure 10: Visual Range as a function of the PM$_{2.5}$ mass concentration. The difference in relative humidity are presented by the blue circles (RH less than 35%) and purple circles (RH higher than 35%).

Furthermore, the light extinction could be reconstructed into the contributions of each chemical species by using their mass concentration and IMPROVE (equation 1). IMPROVE assumes that sulfate and nitrate are fully neutralized into ammonium sulfate and ammonium nitrate. To confirm if this assumption applies to our site, a scatter plot of the molar ratio of the cations (ammonium) with the anions (nitrate + 2sulfate) is presented in Figure 11a. The ratio of cations and anions is more than one; hence there was plenty NH_3 in the air to neutralize all sulfate and nitrate into ammonium sulfate and ammonium nitrate. As a consequence, the IMPROVE assumption applies under this context. In this location the NH_3 sources are anthropogenic and agricultural. The light extinction is reconstructed based on equation 1 and compared with the measured light extinction at the

same wavelength 550 nm, using the previous assumption of sulfate and nitrate, and the externally mixed aerosol. To get the light extinction "measured" at 550 nm, an interpolation between the 532 nm and 870 nm, similar to the Angstrom exponent, is used. The comparison between the light extinction measured and the light extinction calculated (Figure 11b) indicates that the IMPROVE model is able to apportion the light extinction with a slope close to 1 from the period of January 21st until 29th. A time series of the apportioned light extinction coefficient for each PM component compared with the measured one is presented in Figure 12. The mismatch in the February measurements is due to the uncertainties in the mass concentration measured by the HR-ToF-AMS similar to Figure 4a.
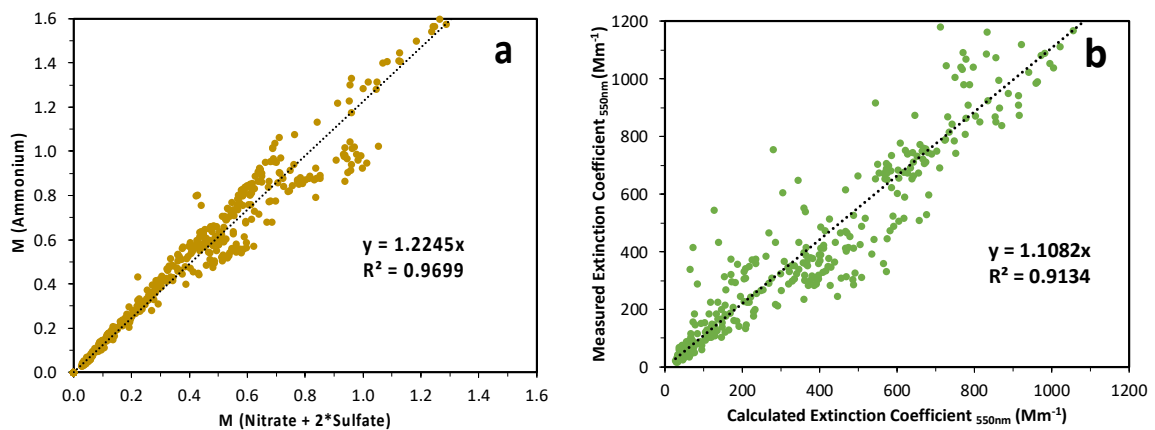
Figure 11: IMPROVE Results. (a) Molar ration between cations (ammonia) and anions (Nitrate + 2Sulfate). (b) Light scattering comparison between the measured and the IMPROVE calculated.

28
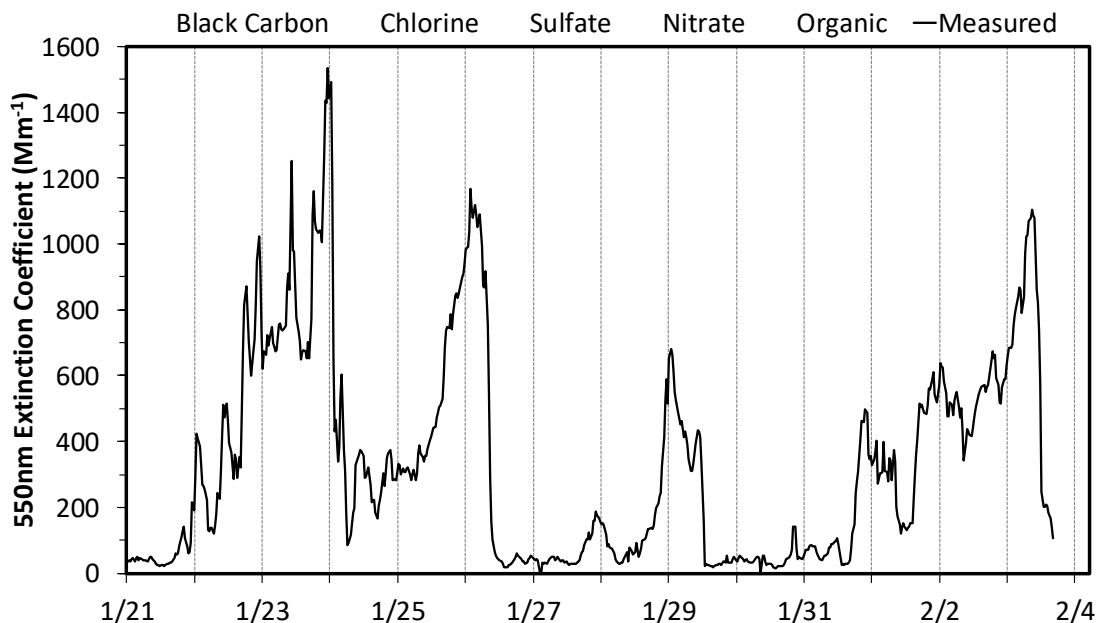
Figure 12: Time series of the light extinction coefficient and the contribution by each chemical specie.

The variations in the PM$_{2.5}$ mass concentration and light extinction budget during a pollution episode are further evaluated by examining in detail the first pollution episode (Figure 13). The clean period starts with new particle formation events and then further growth. The average PM$_{2.5}$ mass concentration and light extinction during the clean period are 31 μg m^{-3} and 154 Mm^{-1}, respectively. The dominant species contributing to the mass and the light extinction are the organics. Interestingly, BC only contributes to the mass by almost 9% but it contributes almost two times more to the light extinction. As the time progressed, there is continuous growth and a rapid accumulation over the transition period, where the mass concentration increases by almost four times higher, with an average of 123 μg m^{-3}. In the transition period, there is a decrease in the organics contribution, and an increase in the secondary inorganic contribution for both, the mass concentration and the

29

light extinction. The average light extinction during the transition period was 645 Mm^{-1} and reached to 983 Mm^{-1} during the polluted period. In the polluted period, during the daytime, the MHL remains low (figure 5b) providing stagnant conditions and provoking an increase in the mass concentration and light extinction. During the early morning of January 24, the mass concentration decreased because a weak front passed, increasing the MLH and dilution. After the front passed, the wind shifted, and MLH decreased, therefore, the second polluted period peak appears but with similar contributions to the first one. Hence, January 21-26 corresponds to a single haze episode instead of two small ones. Figure 14 shows the air mass backward trajectories estimated by the HYSPLIT model [*Stein et. al.,* 2015]. During the clean period, the wind comes from the north (shown in purple) which is surrounded by mountains, then the wind changes direction coming from the southwest (shown in turquoise), a region that is influenced by multiple coal power plants. Later, the wind direction moves from the northwest (shown in green), however, the PBL is low trapping the pollutants and leading to the transition period in which the PM$_{2.5}$ mass concentration increases. Subsequently, the pollution peak period (shown in red) corresponds to a combination of low MLH and a wind direction change from the southeast area, passing by the local emission sources near downtown Beijing. As a summary, the meteorological conditions influence the haze development, and thus the optical properties.
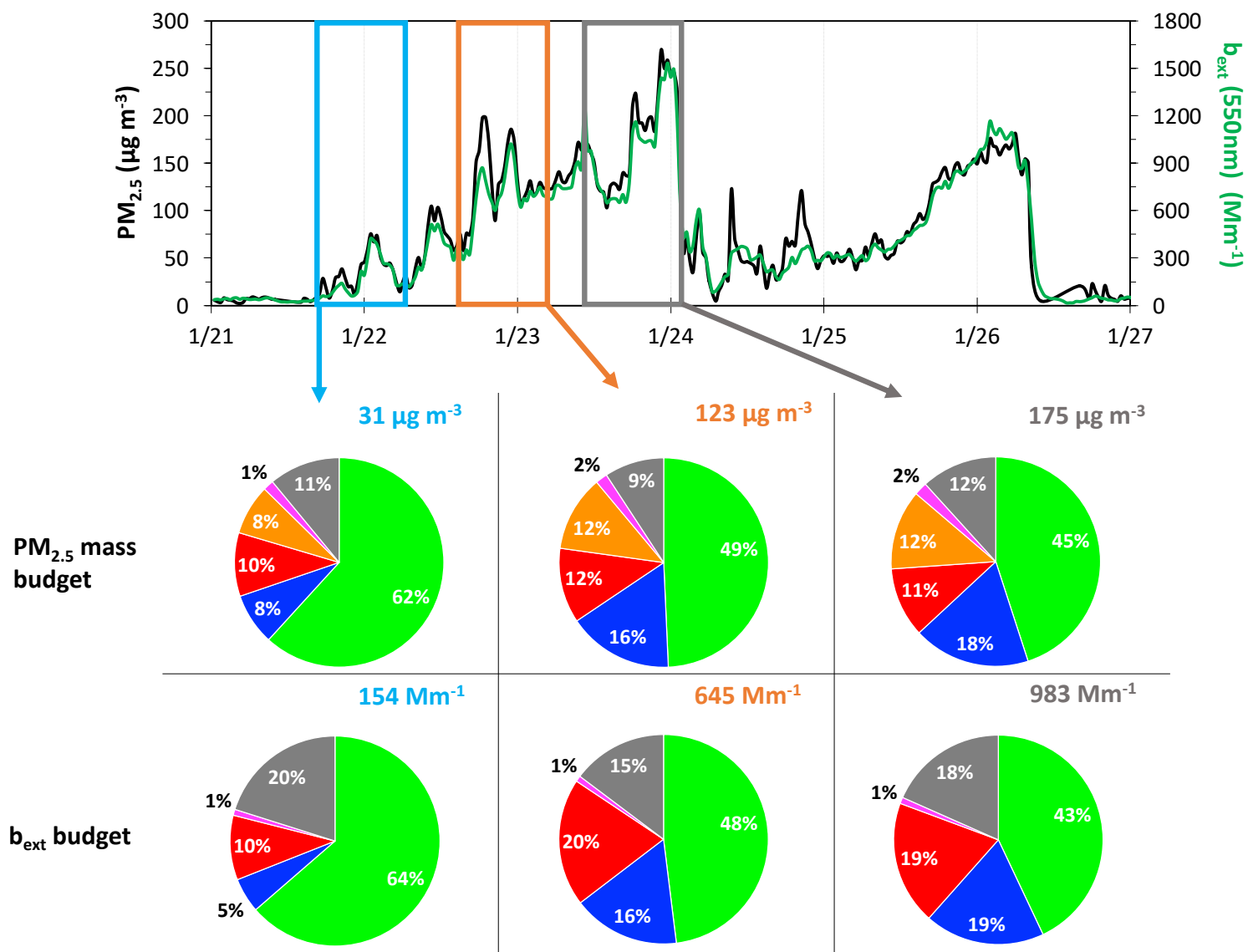
Figure 13: Variation of PM2.5 mass concentration and light extinction budget as the haze develop.

31

NOAA HYSPLIT MODEL
Backward trajectories ending at 0100 UTC 24 Jan 15
GDAS Meteorological Data
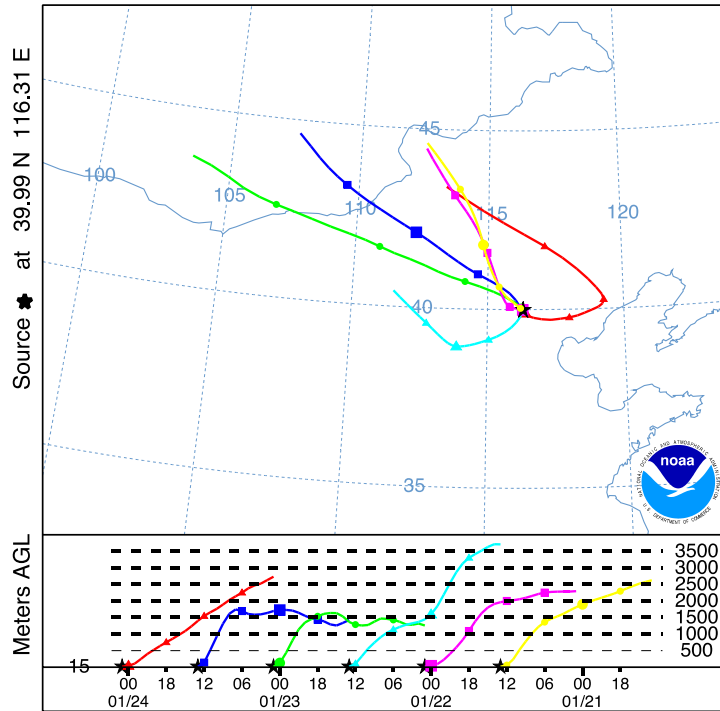
Figure 14: Air mass backward trajectories observed during the haze episode from January 21st – 24th. The red, green and magenta lines correspond to the polluted, transition and clean periods, respectively.

Atmospheric Implications

Field measurements were conducted in Beijing during the winter of 2015 to study the chemical and optical properties of the aerosols during severe haze events. The anti-correlation between the $PM_{2.5}$ mass concentration and the MLH indicates that the meteorological conditions drive the accumulation process through the polluted period. During the haze episodes, an increase of the secondary inorganic component is observed as the haze develops, while the organics decrease. The mass concentration and the light

32

extinction are directly proportional, similar to the VR. However, the SSA on average remains invariant, with a slight increase when the mas concentration increases. Therefore, during this period, the components leading to the absorption remained constant (BC), while the components leading the scattering increased (mainly inorganics). This trend is further confirmed by using the IMPROVE model. Additionally, combining the apportion of the light extinction with the SAC and AAC, the dominant species leading to absorption is BC. No evidence of other absorbing components, such as light-absorbing organics, was detected. The light extinction lead to stabilization of the atmosphere, restricting the vertical transport, trapping the pollutants close to the surface and emission sources, negatively affecting the air quality. From the pollution control perspective, the mitigation of PM (especially BC) and gaseous precursors could potentially contribute to the improvement of the air quality and climate.

CHAPTER III

CONVERSION OF SULFUR DIOXIDE TO SULFATE UNDER POLLUTED

ENVIRONMENTS: A FIELD AND CHAMBER STUDY*

Introduction

Sulfur dioxide (SO_2) is a major pollutant in the atmosphere generated by biogenic

sources (volcanic emissions and dimethyl sulfide oxidation) and anthropogenic sources

(fossil fuel burning, industry, transoceanic shipping, and power plants) [*Finlayson-Pitts

and Pitts Jr*, 2000; *Seinfeld and Pandis*, 2006; *Zhang et al.*, 2015b]. Gaseous SO_2 is

converted to particulate sulfate (SO_4^{2-}) through gas-phase oxidation or aqueous reactions,

but the detailed chemical mechanisms remain debatable. Sulfate aerosols constitute a large

fraction of fine particulate matter around the globe. As part of atmospheric particulate

matter, sulfate aerosols may exert direct and indirect effects on climate [*IPCC*, 2013].

Furthermore, a major fraction of regional acid deposition is attributed to sulfate content,

altering ecosystems [*Chang et al.*, 1987].

OH radicals dominate the gas phase oxidation of SO_2 with a reaction rate constant

of 1.5×10^{-12} cm^3 $molecule^{-1}$ s^{-1}. The typical tropospheric OH radical concentration is

$\sim 1 \times 10^6$ molecules cm^{-3}; therefore, the oxidation lifetime of SO_2 is approximately 1 week.

The aqueous phase oxidations of SO_2 may occur faster, including reactions with dissolved

ozone, hydrogen peroxide, organic peroxides, OH radicals, and nitrogen dioxide (NO_2) via catalytic or noncatalytic pathways involving mineral oxides [*Seinfeld and Pandis*, 2006; *Zhang et al.*, 2015b]. However, the aqueous pathway occurs in a two-step process: first the SO_2 must be dissolved (Henry's Law Constant = 1.23 M atm^{-1}) and later the main reaction occurs [*Seinfeld and Pandis*, 2006]. It is important to note that the SO_2 dissolution is pH-dependent [*Finlayson-Pitts and Pitts Jr*, 2000]. Most recently an interfacial SO_2 oxidation mechanism involving O_2 on acidic microdroplets has been suggested [*Hung and Hoffmann*, 2015].

Typically, atmospheric measurements show high sulfate production during severe haze events in China, but they cannot be explained by current atmospheric models [*Wang et al.*, 2014]. Moreover, high sulfate production occurred concurrently with high RH, nitrogen oxides ($NO_x = NO + NO_2$), and ammonia (NH_3), suggesting an aqueous oxidation pathway [*Quan et al.*, 2015; *Xie et al.*, 2015]. SO_2 and NO_x are coemitted products from fossil fuels, and NH_3 occurs because of agricultural activities. Under urban conditions, aqueous SO_2 oxidation by NO_2 pathways has been hypothesized as being important in the presence of a sufficient neutralizing agent such as NH_3 [*Clifton et al.*, 1988; *Lee and Schwartz*, 1983; *Seinfeld and Pandis*, 2006]. Normally, this pathway has been neglected in atmospheric models due to the limited water solubility of NO_2 (Henry's Law Constant = 1.0×10^{-2} M atm^{-1}) without a neutralizing agent [*Sarwar et al.*, 2013]. Lee and Schwarz studied the oxidation of S(IV) by NO_2 in the liquid phase and reported a bulk reaction rate constant proportional to pH.

Recent studies have pointed out that the aqueous oxidation of SO_2 by NO_2 is unlikely due to low particle acidity estimates using thermodynamic models [*Guo et al.*,

2017; *Liu et al.*, 2017]. However, in thermodynamic models, recent studies have treated the PM as a mixture dominated of inorganic salts [*Cheng et al.*, 2016; *Guo et al.*, 2017; *Liu et al.*, 2017] and neglected the contribution of organics since those thermodynamic models are incapable of representing multicomponent aerosols. In addition, the model is highly dependent on aerosol water content (AWC), but since they neglected the organic aerosol contribution [*Guo et al.*, 2017], their values for AWC might not be accurate, due to the organic-rich environment in Beijing, and some organics are water soluble. However, previous studies have reported that a significant portion of organic aerosols in China are water-soluble, such as organic acids, which in turn could react with basic species (like NH_3 and amines) and consequently enhance particle hygroscopicity [*Wang et al.*, 2009; *Wang et al.*, 2006a; *Wang et al.*, 2013a; *Yao et al.*, 2016; *Zhang et al.*, 2015a].

Using data from the previous chapter, a correlation among SO_2, NO_x, PM, and RH levels during the haze events in China was noted, which is in agreement with previous studies [*Guo et al.*, 2014]. In this chapter, a more detail discussion about the ambient measurements results and chamber experiments, aimed to explore the conversion of sulfur dioxide into sulfate under the presence of NO_2 and NH_3 using oxalic acid seeds as a surrogate for an organic-rich environment [*Meng et al.*, 2014; *Wang et al.*, 2010a]. Such experiments may help explain haze formation and PM growth in highly polluted environments such as Beijing, China.

Methodology

Ambient measurements in Beijing 2015

Ambient measurements were conducted on the campus of Peking University (PKU) located in northwestern Beijing from January 20 to February 4, 2015 [*Wang et al.*, 2016]. The site is representative of an urban area that is heavily influenced by mobile sources with no significant stationary sources. A suite of instruments was deployed to simultaneously measure several gaseous species and aerosol chemical composition. Online monitors were used for measuring ambient gas concentration. NO_x and SO_2 were measured using the chemiluminescence NO_x analyzer (Ecotech EC9841) and SO_2 analyzer (Ecotech EC9852), respectively. The chemical composition of submicron particulate matter (PM_1) was measured by an Aerodyne High-Resolution Time-of-Flight Aerosol Mass Spectrometer (HR-ToF-AMS). The HR-ToF-AMS operated in 5-minute cycles to obtain the mass concentrations of nonrefractory species such as ammonium (NH_4^+), sulfate (SO_4^{2-}), nitrate (NO_3^-), chloride (Cl^-), and organics [*DeCarlo et al.*, 2006]. The instruments were located in an air-conditioned room on the roof of a building about 15 m above ground level.

Chamber studies

Chamber experiments were conducted by exposing oxalic acid seed particles to SO_2, NO_2, and NH_3 at high RH to later measure the dry size variation of the particles, assumed to be from the sulfate formation [*Wang et al.*, 2016]. For the experimental setup (Figure 15), a 1-m^3 Plexiglass with a Teflon film covered by aluminum foil was used. The chamber was equipped with a humidifier and differential mobility analyzer (DMA) with a

condensation particle counter (CPC) to control the relative humidity and measure the size distribution and concentration, respectively. The humidifier consists of flowing 2-SLPM (standard liters per minute) nitrogen flow through a 5-gallon water reservoir with a heater set to 307 K, which produces a humidified nitrogen flow that was subsequently introduced into the chamber. The RH was monitored by using an RH probe located downstream of the chamber.

The chamber setup was operated in two modes: seeding and scanning. For the seeding mode, the particles moved from the atomizer to the DMA to the chamber. An aqueous solution of oxalic acid (1 wt%) was atomized using dry nitrogen to generate polydisperse particle. The particles were diluted with a dry nitrogen flow, heated to 343 K to remove excess humidity, and further dried using two Nafion tubes. Later, the particles were size-selected using a DMA to produce a monodisperse distribution, which was injected into the chamber. Typically, the size-selected particle number concentration inside the chamber was elevated to 5×10^4 cm^{-3} before gases were injected. For scanning mode, the flow lines were modified using three-way valves to change the direction of the aerosol flow from the chamber to the DMA and CPC. The humidified nitrogen flow was set at 2 SLPM to push the particles in the chamber into the DMA and CPC to determine the size distribution from 10 to 400 nm. Similar to the seeding mode, the particle flow was heated and dried before entering to the DMA.
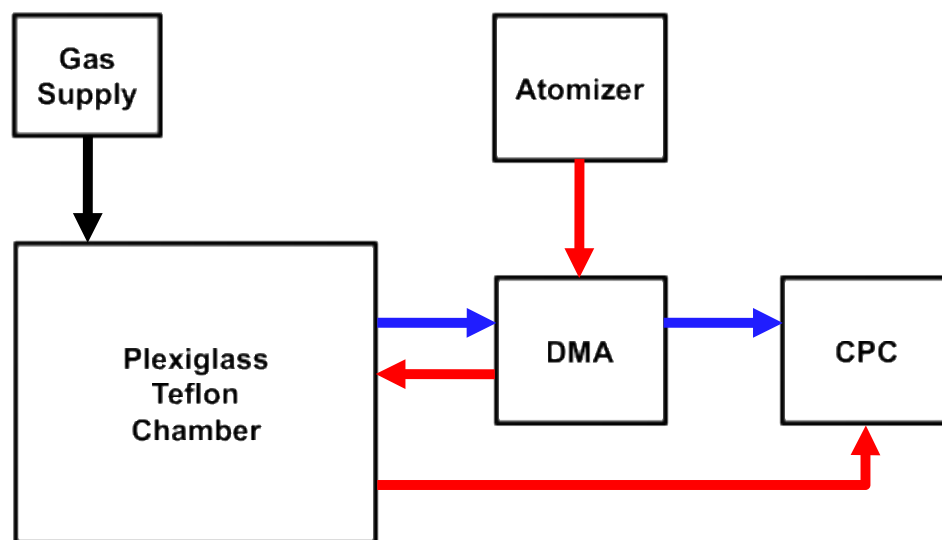
Figure 15: Schematic representation of the reaction chamber. The seeding mode is illustrated in the red-arrow process, while the scanning mode is in blue.

For the gases, SO_2 was obtained from Sigma-Aldrich, and NO_2 and NH_3 were obtained from Matheson. Gas samples of SO_2 and NO_2 were injected into the chamber from pressurized lecture bottles using a mass flow controller to monitor the gas flow into the chamber. The concentrations in the lecture bottles were prepared by a two-step dilution of SO_2 or NO_2 with dry nitrogen. Ammonia (2×10^3 ppm) was used as received without dilution. SO_2, NO_2, and NH_3 were introduced separately into the chamber with an initial concentration of 250 ppb, 250 ppb, and 1 ppm, respectively. The time to inject the gases was extended when a higher concentration was desired, and the controlled mass flow was kept constant. The particles and gas mixtures were allowed to react for at least 40 minutes before setting the instruments to scanning mode to measure the size distribution of the particles after exposure to the gases.

Results and Discussion

Field measurements

The sulfur oxidation mechanism and its role in severe haze formation by combining field measurements and laboratory experiments is investigated. For the field measurements, the $PM_{2.5}$ mass concentration and the sulfate concentration in PM_1 follows a similar trend. Figure 16 shows the temporal evolution of the mass concentrations of sulfate, showing the increases from less than 10 μg m^{-3} to greater than 20 μg m^{-3}. In this chapter, the periods of clean, transition, and polluted correspond to the SO_4^{2-} mass concentration in PM_1 of less than 10 (blue), 10 to 20 (orange) and greater than 20 (black/dark gray).

For each period, the mass fractions of the five PM_1 main nonrefractory constituents are shown in Figure 17. The sulfate mass fraction increases during the transition and polluted periods, while there is a slight decrease in the organic mass fraction. This behavior of increasing the inorganic mass fraction and decreasing the organic mass fraction, from clean to transition and polluted periods, is typical in urban areas like Beijing [*Guo et al.*, 2014; *Huang et al.*, 2014; *Sun et al.*, 2013]. However, organics still represent a large portion of the total PM_1 constituents, so it is considered an organic-rich environment. Note that during the polluted periods, sunlight is limited; therefore, the increase in sulfate mass fraction is unlikely to follow a photochemical oxidation pathway [*Tie et al.*, 2003].
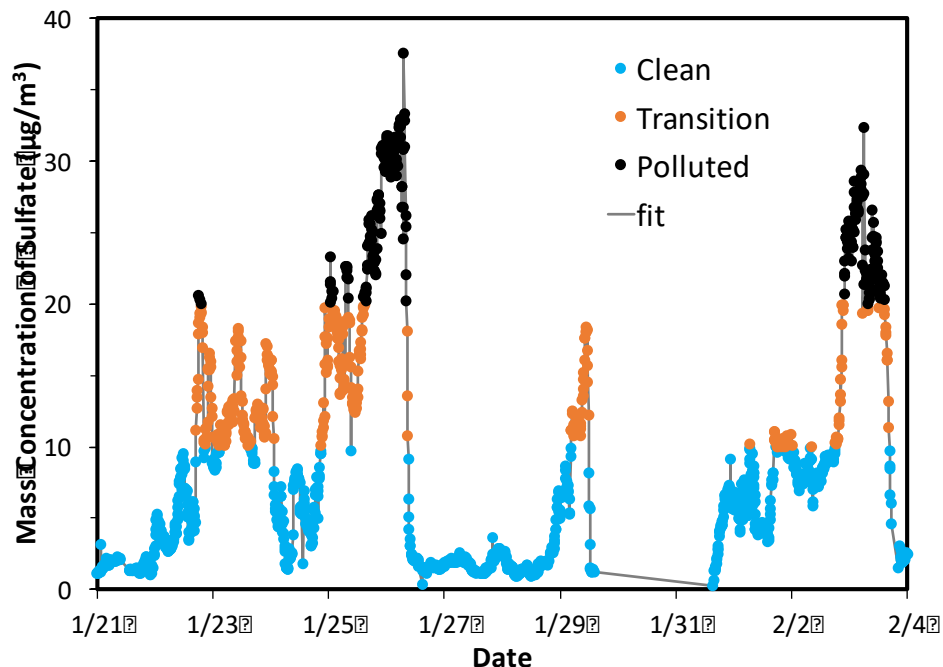
Figure 16: Time series of the sulfate (SO$_4^{2-}$) mass concentration measured in Beijing, China from January 21 to February 4, 2015. The dates on the x-axis correspond to midnight local time. The clean, transition, and polluted periods correspond to sulfate mass concentrations of <10 µg m^{-3}, 10–20 µg m^{-3}, >20 µg m^{-3}, respectively. Reprinted and adapted with permission from the National Academy of Science [Wang *et. al.*, 2016].
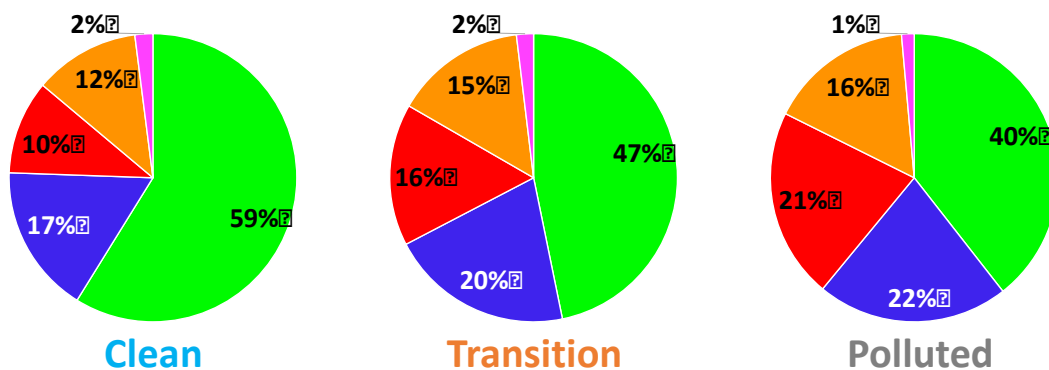
Figure 17: Mass fraction of the five main nonrefractory constituents in PM$_1$ in Beijing, China. An organic-dominant environment undergoes a slight decrease in contribution from clean to polluted, while the contribution of secondary inorganic component increases. Reprinted and adapted with permission from the National Academy of Science [Wang *et. al.*, 2016].

Also, the molar ratio of sulfate to sulfur dioxide was quantified, reflecting sulfur

partitioning between the particle and gas phase. The range of this ratio is from less than 0.1

to 1.2, exhibiting an exponential increase as a function of RH (Figure 18). Therefore,

efficient conversion of SO_2 to SO_4^{2-} occurs at high RH, implicating a possible aqueous

reaction pathway. Moreover, the mixing ratio of SO_2 decreases in the polluted period as

RH increases (Figure 19), indicating a conversion from the gas to particle phase.

Additionally, the equivalent ratio of NH_4^+ to the sum of SO_4^{2-}, NO_3^-, and Cl^- was

calculated (Figure 19d). The equivalent ratio was closed to unity in the polluted period,

indicating a neutralizing behavior. It is important to note that the equivalent ratio is only

useful to evaluate inorganic aerosol neutralization (i.e., close to unity), but is not suitable

to interpret aerosol acidity [*Hennigan et al.*, 2015; *Liu et al.*, 2017; *Murphy et al.*, 2017].
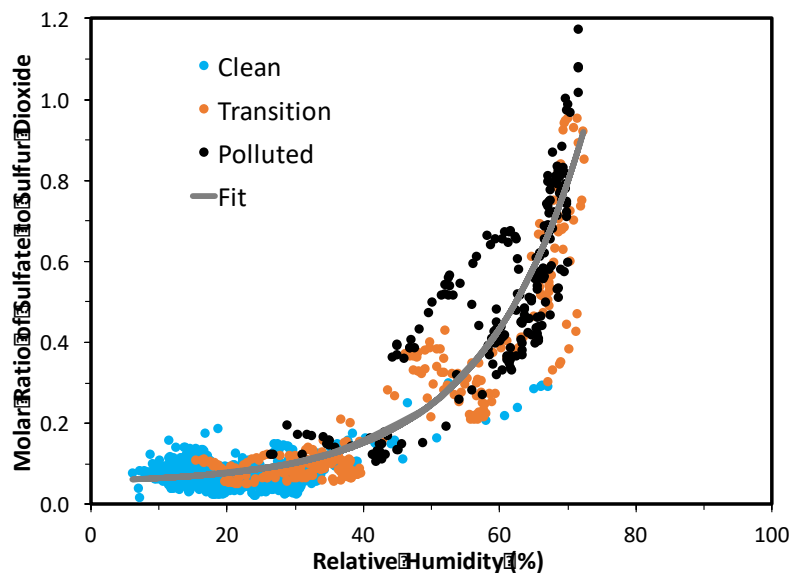
Figure 18: Molar ratio of sulfate to sulfur dioxide (SO_4^{2-} to SO_2) as a function of the RH. The exponential fit line is $y = 0.05 + [(7.0 \times 10^{-3}) \ e^{(x/15)}]$ with $R^2 = 0.88$. Reprinted and adapted with permission from the National Academy of Science [Wang *et. al.*, 2016].

42
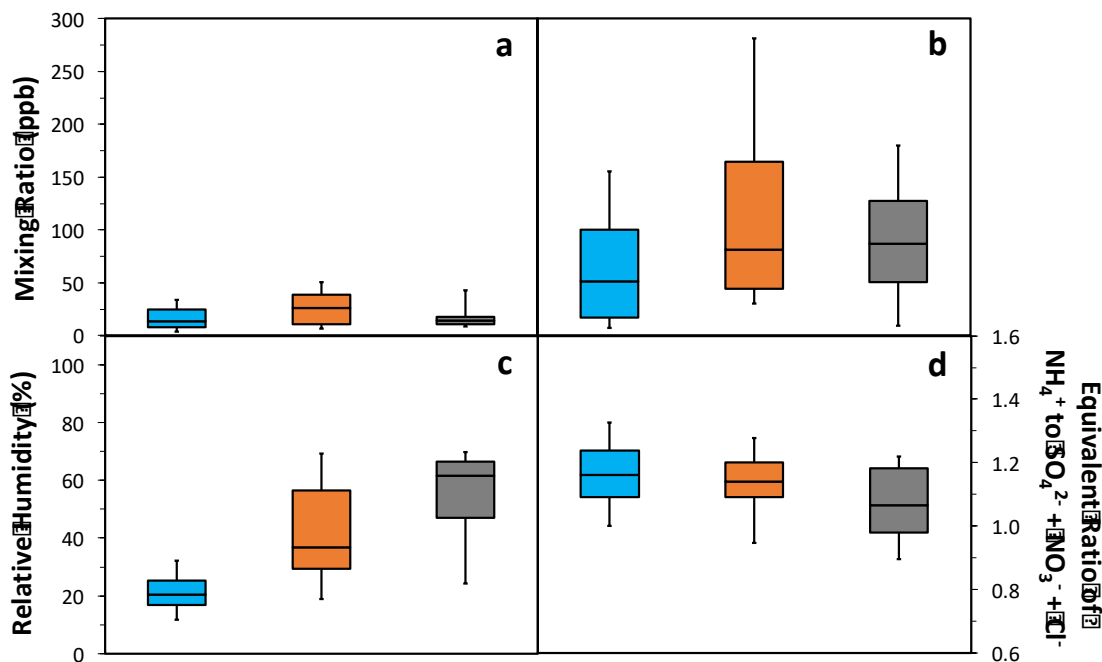
Figure 19: Mixing ratios of SO$_2$ (a), NO$_2$ (b), RH (c), and equivalent ratios (d) during the field campaign in Beijing, China. The blue, orange, and dark gray colors correspond to the clean, transition, and polluted period. The top and bottom vertical lines for each box correspond to the 95th and 5th percentiles, respectively, and the top, middle, and bottom horizontal lines of the box mark are the 75th, 50th, and 25th percentiles of the data range. Reprinted and adapted with permission from the National Academy of Science [Wang *et. al.*, 2016].

Chamber

For these experiments, analysis has been focused on the multiphase conversion of SO$_2$ into SO$_4^{2-}$ under the simultaneous presence of NO$_2$ and NH$_3$, using oxalic acid seeds as a surrogate of organic aerosols. Those conditions are representative of sulfate formation in PM under polluted environments (i.e., high levels of NO$_2$, SO$_2$, NH$_3$, and organics). Previously, a similar experiment in our group showed the detection of sulfate (m/z = 96) using TD-ID-CIMS, and this signal was proportional to the particle growth [*Fortner et al.*, 2004; *Xu et al.*, 2014]. In the present study, the particle growth was monitored by

parametrizing the particle growth factor (GF) using the DMA-CPC system coupled to the

chamber. The GF is defined as the measured ratio of the dry particle sizes (D_p/D_o), where

D_p and D_o are the values after and before exposure, respectively. The growth rate (GR) is

defined as the increase of particle size per minute of reaction. Table 2 describes the

experimental conditions, noting that the particles grow only during the inclusion of all

components. Such results suggest that the growth of PM due to the conversion of SO_2 to

SO_4^{2-} is synergetic; thus, sulfate requires the combined presence of all components (i.e.,

NO_2, SO_2, NH_3, and high RH).

Table 2: Experimental conditions for particle growth detection in the reaction chamber. The symbols ✔ and ✖ indicate whether a species is included in or excluded from the exposure, respectively.

Experimental Run	SO_2 (250 ppb)	NO_2 (250 ppb)	NH_3 (1 ppm)	Water Vapor (65% RH)	Growth Factor
1	✔	✖	✖	✔	1.0
2	✔	✖	✔	✔	1.0
3	**✔**	**✔**	**✔**	**✔**	**1.3**
4	✔	✔	✖	✔	1.0
5	✔	✔	✔	✖	1.0

The normalized size distributions of aqueous sulfate formation in the reaction

chamber are shown in Figure 20. When the oxalic acid particles, with an initial dry

diameter of 43 nm, are exposed to SO_2, NO_2, NH_3, and 65% RH for 40 minutes, the size

distribution shifts to larger sizes, indicating a particle growth attributable to sulfate

production [*Wang et al.*, 2016]. At high RH, oxalic acid particles uptake water and

subsequently react acid-base with NH_3, forming ammonium oxalate. Later, the SO_2 is

dissolved in ammonium oxalate-water containing particles and oxidized by NO_2 into SO_4^2,

which subsequently is neutralized by NH_3 to produce ammonium sulfate $((NH_4)_2SO_4)$.
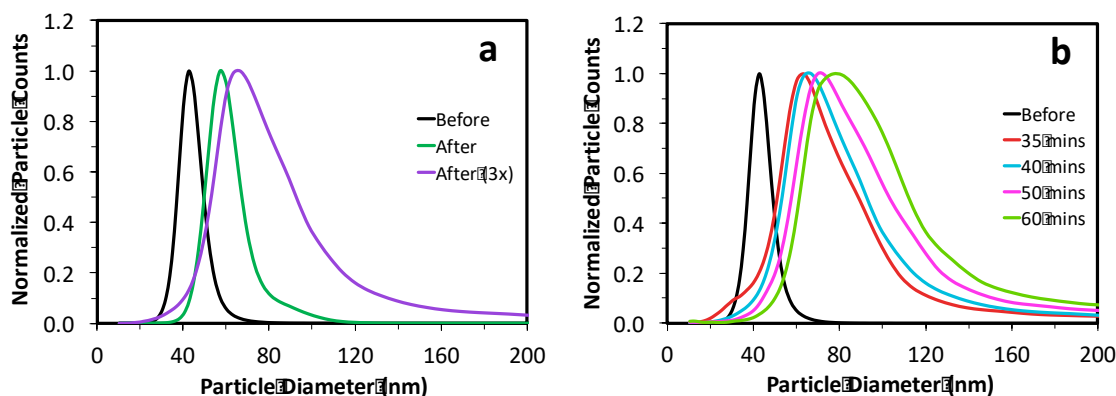
Figure 20: Evolution in the size of oxalic acid particles after exposure to SO_2, NO_2, and NH_3 at 65% RH. (a) Normalized size distribution of 43-nm size-selected oxalic acid particles before and after being exposed to SO_2, NO_2, NH_3, and 65% RH for 40 minutes. The green color represents the standard concentration of 250 ppb of SO_2, 250 ppb of NO_2, and 1 ppm of NH_3. The purple conditions were three times higher than the standard concentrations (i.e., 750 ppb of SO_2, 750 ppb of NO_2, and 3 ppm of NH_3). (b) Normalized size distribution of 43-nm size-selected oxalic acid particles before and after being exposed to 750 ppb of SO_2, 750 ppb of NO_2, 3 ppm of NH_3, and 65% RH at several reaction time frames.

For standard conditions, the concentration of gases was 250 ppb, 250 ppb, and 1 ppm for SO_2, NO_2, and NH_3, respectively. The GF for standard conditions is about 1.3 with a GR of 0.4 nm min^{-1}. However, when the gas concentrations were three times higher (i.e., 750 ppb of SO_2, 750 ppb of NO_2, and 3 ppm of NH_3), the resulting GF was about 1.6 with a GR of 0.6 nm min^{-1}. The particles grow because the formation of the aqueous phase promotes SO_2 oxidation by NO_2 with NH_3 neutralization, resulting in a continuous increase in dry particle size with increasing reaction time. At higher concentrations, the GF is less

than 1.3 for 30 minutes and 1.8 for 60 minutes; noting that not only the particle size shifts

but also the distribution broadens, as shown in Figure 20b.

Combining the field and laboratory measurements, we established the occurrence

of an overall aqueous reaction between SO_2 and NO_2:

$$SO_2(g) + 2NO_2(g) + 2H_2O(aq) \rightarrow 2H^+(aq) + SO_4^{2-}(aq) + 2HONO(g)$$
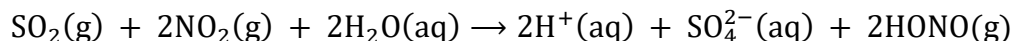
noting that the reaction rate stoichiometricaly depends on the gaseous NO_2 concentration.

Also, the solubility is inversely proportional to the temperature [*Gomez et al.*, 2015].

Moreover, the reaction is also dependent on pH, which governs not only the solubility but

also the aqueous reaction rate [*Seinfeld and Pandis*, 2006]. For example, when the pH

value varies from 6 to 4, the SO_2 effective Henry's Law Constant decreases about two

orders of magnitude, leading to a decreased oxidation rate for about two orders of

magnitude [*Seinfeld and Pandis*, 2006]. Furthermore, this reaction increases the acidity in

the aqueous phase but then reduces the solubility and reaction rate, making it self-limiting

because of the acidity effect. The nitrous acid (HONO) generated from this reaction is

released into the gas phase due to its low water solubility. However, HONO provides an

additional photochemical OH source that enhances the atmospheric oxidizing capability

during polluted periods [*Levy et al.*, 2014].

The results indicate that aqueous SO_2 oxidation by NO_2 is favored in two

atmospheric scenarios: under cloud/fog conditions and on fine aerosols with high RH and a

sufficient neutralization agent [*Wang et al.*, 2016]. The latter was shown in our chamber

studies. Since the acidity effect inhibits the oxidation of fine aerosols, the presence of a

basic species (NH_3 in this case) is necessary to maintain the oxidation:
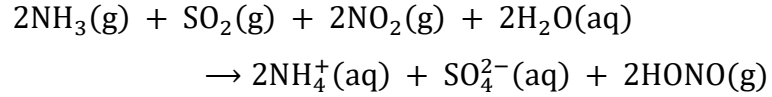
$$2NH_3(g) + SO_2(g) + 2NO_2(g) + 2H_2O(aq)$$
$$\rightarrow 2NH_4^+(aq) + SO_4^{2-}(aq) + 2HONO(g)$$

The formation of various secondary organic and inorganic constituents in fine aerosols is mutually promoting, and severe haze development involves a transition from photochemical to aqueous phase pathway (Figure 21). During the early stage or clean period, efficient photochemical oxidation of VOCs leads to SOA formation, which provides an aqueous medium for subsequent sulfate formation. Later, during the late stage (polluted), the large aerosol growth is maintained by aqueous chemistry due to high RH and low photochemical activity [*Guo et al.*, 2014; *Wang et al.*, 2016]. However, it should be pointed out that severe haze formation in China is characterized by a complex interplay between meteorological, thermodynamic, and chemical processes [*Guo et al.*, 2014; *RenHe et al.*, 2014; *Zheng et al.*, 2015].
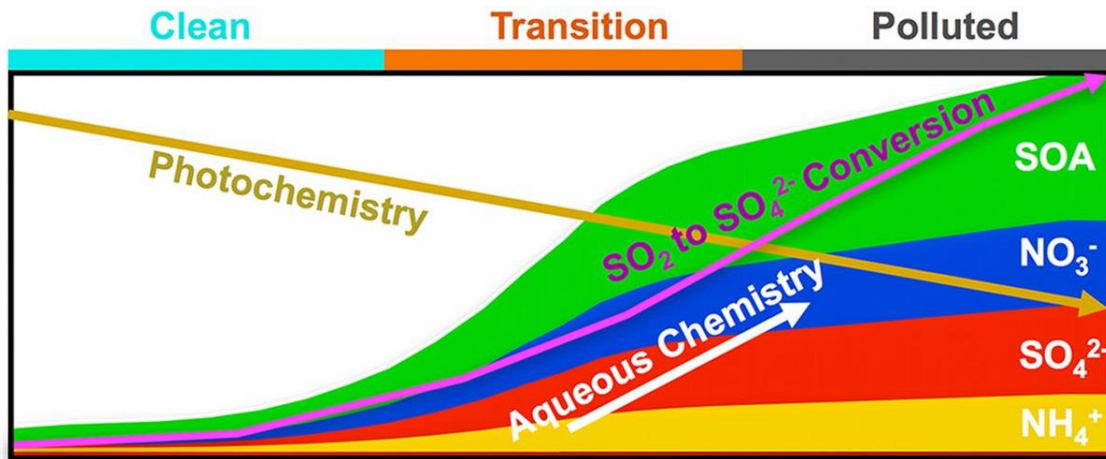
Figure 21: Anticorrelation between the photochemistry and aqueous chemistry during the severe haze evolution from a clean to polluted period in China. Reprinted and adapted with permission from the National Academy of Science [Wang *et. al.*, 2016].

Atmospheric Implications

Sulfur chemistry under atmospheric conditions has remained debatable. The results show that SO_2 oxidation by NO_2 into SO_4^{2-} is facilitated by high RH, low temperature, and large concentrations of NO_2 and NH_3. Significant sources of VOCs, NO_x, SO_2, and NH_3 include industry, traffic, and nitrogen fertilizer [*Liu et al.*, 2013; *Pan et al.*, 2016; *Zhang et al.*, 2015b]. High emissions of these organic and inorganic aerosol precursors lead to a large secondary production of SOA, NO_3^-, SO_4^{2-}, and NH_4^+ in China, combining photochemical and aqueous process.

In this chapter, evidence of ambient sulfate concentration is provided, as well as its dependence on RH. Additionally, laboratory experiments offer more evidence of the multiphase oxidation of SO_2 into SO_4^{2-} by NO_2 under high RH, leading to significant secondary growth. The sulfate production process is enhanced by NH_3 and high levels of RH and led to the particle growth of pre-existing aerosols. Although the chamber experiment used higher gaseous concentration than typically found in ambient conditions (due to the experimental setup), the results are relatively analogous to the organic-rich ambient conditions.

The results indicate that sulfate production is key to the formation of severe haze in China. Even though current efforts have been focused on minimizing SO_2 emissions, significant haze reduction may only be achievable with NH_3 and NO_2 emission controls as well. The synergetic sulfate formation pathway from this work is likely widespread globally because of the increase in emissions of SO_2, NO_x, VOC, and basic species (NH_3 and amines) in many developing countries [*Liu et al.*, 2013; *Zhang et al.*, 2015b]. Those

emission increases in turn contribute not only to air quality problems but also to enhanced

nitrogen or acid deposition with major implications to ecosystems.

CHAPTER IV

FORMATION AND OPTICAL PROPERTIES OF BROWN CARBON FROM SMALL

DICARBONYLS AND AMINES: A BULK STUDY

Introduction

The optical properties of aerosols are important not only to the direct radiative

forcing on climate but also relevant to air quality and weather [*IPCC*, 2013]. Light

absorption and scattering by aerosols stabilize the atmosphere by retarding vertical

transport, resulting in a negative feedback on air quality and inhibition of cloud formation

[*Wang et al.*, 2013b]. For example, black carbon (BC) particles, a SLCP, affect radiative

transfer in the atmosphere because of their strong ability to absorb light over a broad range

of the solar spectrum, representing the second most important climate-warming agent after

carbon dioxide [*Andreae and Ramanathan*, 2013; *IPCC*, 2013; *Pöschl*, 2005]. The

magnitude of BC direct radiative forcing depends on the mixing state (i.e., whether

particles are externally or internally mixed with other aerosol types) and atmospheric aging

by coating with secondary aerosol constituents (such as organics and sulfate), thereby

enhancing the mass absorption cross-section [*Khalizov et al.*, 2009a; *Khalizov et al.*,

2009b; *Peng et al.*, 2016]. There is growing evidence that light-absorbing organic aerosols,

known as brown carbon (BrC), also represent a significant climate-forcer [*Laskin et al.*,

2015]. Typically, BC absorption is wavelength independent, while BrC exhibits the

strongest light absorption at shorter wavelengths [*Kirchstetter et al.*, 2004]. BrC is

produced from various primary and secondary sources. The main sources of primary BrC

include biomass burning [*Ramanathan et al.*, 2007], fossil fuel combustion [*Bond*, 2001], and biogenic releases [*Andreae and Crutzen*, 1997]. Additionally, light-absorbing secondary organic aerosols (SOA) are generated by a variety of atmospheric chemical processes, such as multiphase reactions or cloud processing, yielding high molecular weight light-absorbing organic compounds [*De Haan et al.*, 2009a; *De Haan et al.*, 2011; *De Haan et al.*, 2009b; *Nguyen et al.*, 2012; *Nozière et al.*, 2007; *Powelson et al.*, 2014]. Atmospheric measurements have shown that BrC exists throughout the tropospheric column and its prevalence relative to BC is proportional to the altitude, indicating the contribution of SOA to BrC formation [*Liu et al.*, 2014]. However, light absorption by BrC has yet to be accounted for in estimation of the aerosol direct radiative forcing, since global climate models typically have assumed that SOA is purely scattering (non-absorbing) [*Corr et al.*, 2009; *Feng et al.*, 2013]. The light absorption by organics depends on their molecular structures [*Laskin et al.*, 2015; *Laskin et al.*, 2014] and is influenced by supramolecular interactions [*Phillips and Smith*, 2014]. Currently, the understanding of formation, chemical composition, and optical properties of BrC is limited.

Recent studies have shown the importance of particle-phase chemistry in producing light-absorbing high molecular weight oligomeric species [*Ervens et al.*, 2011; *Herrmann et al.*, 2015; *Lim et al.*, 2010]. Those earlier studies of aqueous chemistry have focused on water-soluble volatile organic compounds (VOC), such as small α-dicarbonyls, particularly glyoxal (GL) and methylglyoxal (MG) [*McNeill*, 2015]. As the important SOA precursors, GL and MG are produced by the photo-oxidation of anthropogenic aromatics and biogenic terpenes and isoprene [*Spaulding et al.*, 2003; *Volkamer et al.*, 2007; *Zhao et al.*, 2005]. Despite their high volatility, GL and MG undergo hydration and polymerization to produce

low-volatility oligomers [*Jang et al.*, 2002; *Zhao et al.*, 2006]. In the troposphere, particularly in urban areas, the small α-dicarbonyls likely co-exist with amines at comparable concentrations [*Munger et al.*, 1995; *Zhang and Anastasio*, 2003]. Low molecular weight aliphatic amines, such as methylamine (MA), dimethylamine (DA), and trimethylamine (TA), are the most abundant. Amines are emitted from various biogenic sources (e.g., ocean organisms, protein degradation, and biomass burning) and anthropogenic sources (e.g., animal husbandry, automobiles, industry, and treatment of sewage and waste) [*Ge et al.*, 2011; *Qiu and Zhang*, 2013]. The small α-dicarbonyls react irreversibly with ammonium salts and primary amines, forming imidazoles and other nitrogen-containing and light absorbing products, but their chemical identities have yet to be characterized [*De Haan et al.*, 2009a; *De Haan et al.*, 2011; *Loeffler et al.*, 2006; *Yu et al.*, 2011].

Previous studies by De Haan and coworkers have investigated cloud processing of GL and MG via the reactions with amino acids and MA in evaporating aqueous droplets and bulk solutions leading to the formation of BrC using nuclear magnetic resonance (NMR), electron spray ionization - mass spectrometry (ESI-MS), and aerosol mass spectrometry (AMS) [*De Haan et al.*, 2009a; *De Haan et al.*, 2011; *De Haan et al.*, 2009b]. The products were identified as imidazoles, and the imine formation was recognized as the rate-limiting step, as later confirmed by theoretical calculations [*Kua et al.*, 2011]. Laskin and coworkers have studied the bulk-phase and chemical aging of biogenic SOA in the presence of ammonia to form BrC. Using nano-desorption electron spray ionization (nano-DESI), the authors concluded that the light-absorbing properties of SOA are determined by trace amounts of strong BrC chromophores [*Laskin et al.*, 2014].

In another recent study, Lin et al. [*Lin et al.*, 2015] have identified a relationship between the optical properties and chemical composition, showing that all chromophores are nitrogen-containing compounds. It has been hypothesized that the chromophores responsible for the browning are highly conjugated nitrogen-containing compounds such as N-heterocycles [*Kampf et al.*, 2016; *Kampf et al.*, 2012; *Kua et al.*, 2011; *Laskin et al.*, 2015; *Yu et al.*, 2011]. Most previous studies have focused on primary amines, although tertiary amines are the most abundant in the atmosphere [*Ge et al.*, 2011]. Most recently, it has been suggested that formation of brown carbon from aqueous- and aerosol-phase reactions involving methylglyoxal occurs at rates that are orders of magnitude faster than that in bulk solutions [*De Haan et al.*, 2017].

In this work, particles containing BrC oligomers were synthesized from the mixtures of small α-dicarbonyls (i.e., GL and MG) and amines (i.e., MA, DA, TA). The optical properties (i.e., absorption, scattering, and extinction) were measured using a combination of photoacoustic spectrometer, nephelometer, and cavity ring-down spectrometer, and the chemical composition was measured by two complementary mass spectrometric techniques. Also, the refractive indexes at the 405 nm wavelength were derived, including the real and imaginary parts. Additionally, the relative radiative forcing of those BrC particles was estimated.

Methodology

The unbuffered model reaction systems in our study included 6 different mixtures, i.e., MG-MA, MG-DA, MG-TA, GL-MA, GL-DA, and GL-TA. All reagents were used as

received and purchased from Sigma Aldrich except for DA, which was purchased from Sinopharm Chemical Reagent. An aqueous solution of 1 M of each reagent was prepared, and 1 mL of the α-dicarbonyl (MG or GL) was combined with 1 mL of the amine (MMA, DMA, or TMA) and sonicated for about 5 hours in small vials. The resulting colored products were dried using nitrogen for several hours to yield 0.5 mL of the solution, which was then redissolved in up to 12 mL of Mill-Q water for optical and chemical composition analysis. The procedure to synthesize the samples and the concentration used in our work were similar to those used previously by De Haan and coworkers [*De Haan et al.*, 2009a; *De Haan et al.*, 2011; *De Haan et al.*, 2009b; *Zarzana et al.*, 2012].

Aliquots of 1 mL were used for determination of chemical composition using two complementary techniques, i.e., thermal desorption-ion drift-chemical ionization mass spectrometry (TD-ID-CIMS) and orbitrap-mass spectrometry (Orbitrap-MS, Thermo Scientific Inc.). The TD-ID-CIMS operated in the positive mode using the hydronium ions (H_3O^+) for analysis of a 2 μL sample. The Orbitrap-MS employed electrospray ionization in the positive mode (ESI$^+$). In the Orbitrap-MS, the sample was diluted 10 times with Mill-Q water before injection at a flow rate of 5 μL min^{-1} [*Wang et al.*, 2017a].

The experimental setup for measuring optical properties is shown in Figure 22. The main components included an atomizer (DMT portable aerosol generator), differential mobility analyzer (DMA, TSI 3081), condensation particle counter (CPC, TSI 3775), and photo-acoustic extinctometer (PAX, DMT 405). The procedures for aerosol production and processing have been described elsewhere and are described here only briefly [*Khalizov et al.*, 2009a]. Aqueous solutions of the mixtures were atomized using pre-purified nitrogen to generate poly-disperse aerosols. The particles were diluted with a dry, particle-free

nitrogen flow and passed through a silica gel diffusion dryer to reduce the relative

humidity to less than 10%. The aerosols were size-selected using a DMA to produce a

mono-disperse distribution. The mono-disperse aerosol flow was then split between the

CPC and the PAX to measure the aerosol concentration and the optical properties,

respectively.
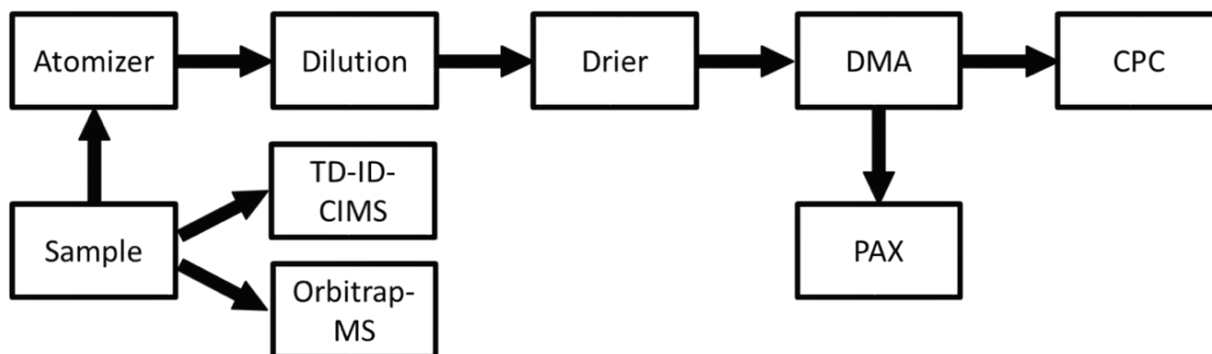
Figure 22: Experimental setup for the optical properties and chemical composition analysis.

The PAX used in-situ photoacoustic technology to measure absorption and

reciprocal nephelometry to measure scattering [*Arnott et al.*, 2003]. In the absorption cell,

a laser beam directed through the aerosol stream was modulated at the resonant frequency

of the acoustic chamber. The energy absorbed by particles was thermally transferred to the

surrounding air, and subsequent air expansion produced a sound wave, which was recorded

by a microphone. In the scattering cell, the standard nephelometer was used, but the

locations of the light source and detectors were reversed. The instrument was calibrated

with polystyrene latex spheres and Aquadag soot particles. The extinction was calculated

from the sum of the absorption and scattering.

55

The effective densities (ρ) of aerosols were measured by using a DMA-APM (aerosol particle mass APM 3600, Kanomax) analyzer [*Khalizov et al.*, 2009a]. The effective density is defined as the ratio of the measured mass to the volume, which is determined by the measured size by assuming spherical particles. Measurements were repeated for a range of particle diameters between 150 nm and 350 nm and at different concentrations. For each diameter, the optical properties (extinction, scattering and absorption), the density, and the particle concentration were determined. The data was corrected for doubly charged particles.

For a cell containing only particles in nitrogen gas, the absorption coefficient (b_{abs}) depends on the particle size (D_p) and concentration (N). The absorption cross section (C_{abs}) is calculated by normalizing b_{abs} with N. C_{abs} is a function of D_p, the wavelength of incident radiation (λ), and the complex refractive index (RI). Mass absorption cross-sections (MAC) is calculated using ρ measured,

$$\text{MAC} = \frac{6C_{abs}}{\rho \times \pi \times D_p^3} \qquad (5)$$

The complex refractive index (RI) is defined by RI = n +ik, where the real part *n* represents the scattering and the imaginary part *k* represents the absorbing component. Since RI is independent of the particle size, it is calculated by using a range of different particle sizes and concentrations. To determine RI, the absorption efficiency at each size is calculated for a given value of *n* and *k* using the Mie code for spherical particles, on the basis of the FORTRAN code from Bohren and Huffman [*Bohren and Huffman*, 2004]. The calculated

56

absorption cross-section value is determined by summing the absorption from both the doubly and singly charged particles for a given RI. The calculated total absorption is compared to the measured absorption. The best-fit refractive index is determined by minimizing the reduced cumulative fractional difference (CFD) [*Zarzana et al.*, 2012],

$$CFD_r = \frac{1}{N}\sum_{i=1}^{N}\frac{|C_{abs(theory)} - C_{abs(measured)}|}{C_{abs(measured)}} \qquad (6)$$

The CFD is calculated for a wide range of *n* and *k* values, and the lowest CFD value is taken to be the refractive index for the mixture. The uncertainty in the retrieved *n* and *k* is determined by varying C_{abs} with the uncertainty of the measurements [*Washenfelder et al.*, 2013]. To estimate direct radiative forcing due to the presence of our particles, the modified version of the Bond and Bergstrom equation by Chylek and Wong is used [*Bond and Bergstrom*, 2006; *Chylek and Wong*, 1995]. To compare the direct radiative effect as a function of size, the relative forcing equation (ΔF_{rel}) is chosen for simplicity:

$$\Delta F_{rel} = -[(1-a)^2\beta Q_{sca} - 2aQ_{abs}] \qquad (7)$$

where *a* is surface albedo, β is the backscatter fraction, Q_{sca} is the scattering efficiency, and Q_{abs} is the absorption efficiency. The surface albedo is set to 0.15, and the scattering and absorption efficiencies are calculated using the RI from the Mie Theory.

Results and Discussion

Optical Properties

The resulting mixtures of α-dicarbonyls and amines are shown in Figure 23. The optical properties of particles at the 405 nm wavelength were measured using the PAX at five concentrations and five diameters. Figure 24a shows the absorption coefficient (b_{abs}) as a function of the particle number concentration (N) for different particles sizes from the MG-DA mixture. The measured b_{abs} increases with particle number concentration and particle size, in accordance with the Beer Law. In addition, the results for all sizes and mixtures exhibit a high linearity ($R^2 \approx 0.99$) and an intercept close to zero. The similar behaviors of b_{abs} are observed for all 6 mixtures, i.e., MG-MA, MG-TA, GL-MA, GL-DA, and GL-TA. For each diameter, the C_{abs} value is determined from the slope of the lines in Figure 24a, and the results for MG-DA are plotted as a function of size in Figure 24b. The values for C_{ext} and C_{abs} increase with particle size, as is shown for the MG-DA mixture. In contrast, the single scattering albedo ($SSA = C_{sca}/C_{ext}$) decreases as a function of size, which is explained by a relatively larger increase in C_{abs} than in C_{sca}. Figure 25 shows a comparison of the C_{ext}, C_{abs}, and SSA values for all 6 mixtures. The trend of the SSA variation with particle size for MG-MA is similar to that of MG-DA, except with SSA lower values. On the other hand, the SSA is invariant with particle size for other mixtures, because of the much smaller C_{abs} values.

Figure 23: Picture of the solutions before and after mixing.

To compare the SSA values between the different mixtures, the size average SSA is shown in Figure 26a. At the 405 nm wavelength, the SSA values increase from MA, DA, to TA (ranging from 0.75 for MG-MA to near unity for MG-TA), but is nearly invariant for the GL mixtures (i.e., close to unity). For the MG mixtures, the SSA variation is consistent with the darkness of the solutions, i.e., the darkest for the primary amines and the lightest for the tertiary amines. This trend is explained by the chemical reactivity and steric effects [*Qiu and Zhang*, 2013]. The MG mixtures exhibit lower SSA than those for the GL mixtures with the respective amines, consistent with the previous studies showing that the MG reactions form light-absorbing materials more efficiently than the analogous GL reactions [*Sareen et al.*, 2010; *Shapiro et al.*, 2009].
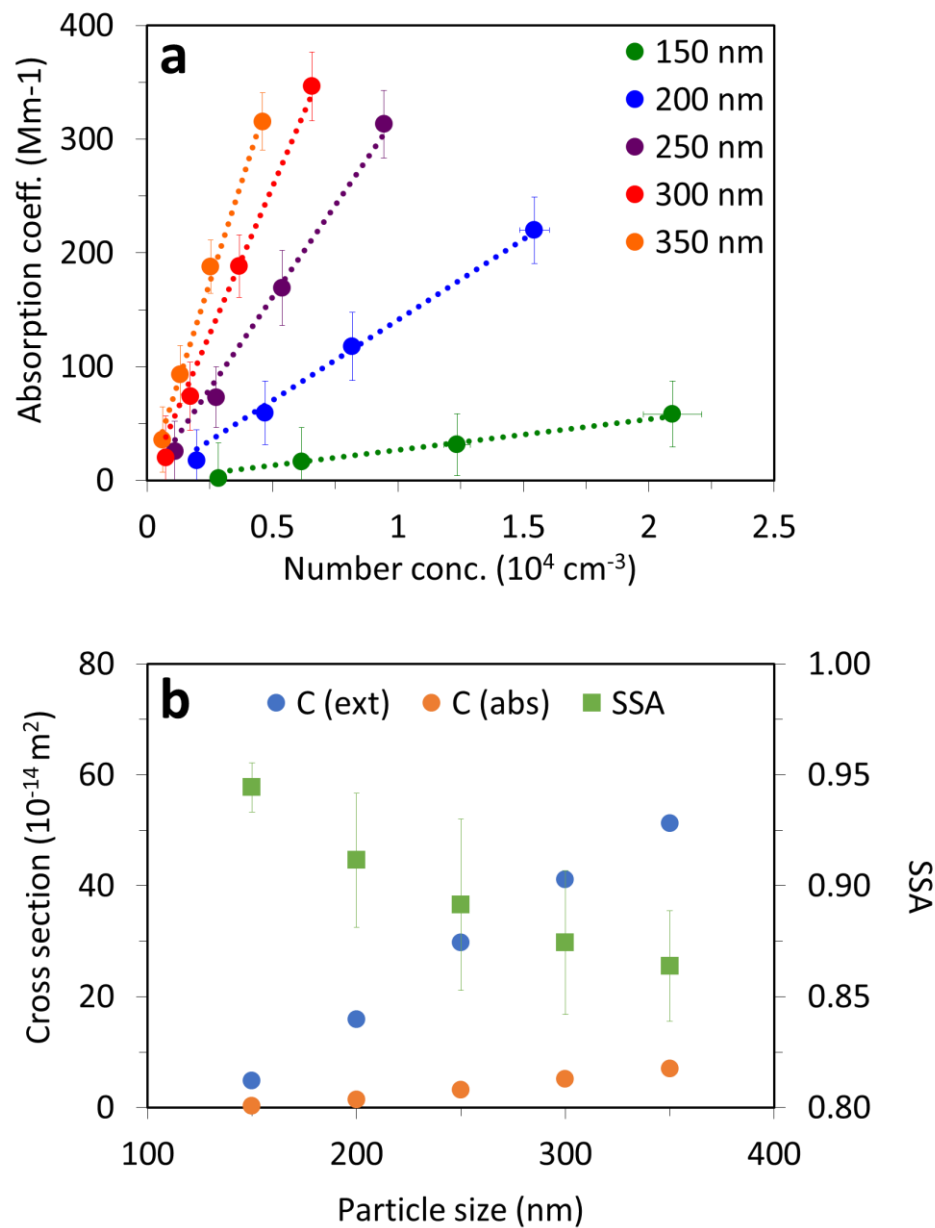
Figure 24: Measured optical properties for MG-DA at the 405 nm wavelength. (a) Absorption coefficient (b_{abs}) as a function of particle concentration. (b) Single scattering albedo (*SSA*), absorption cross section (C_{abs}), and extinction cross section (C_{ext}) as a function of particle size.
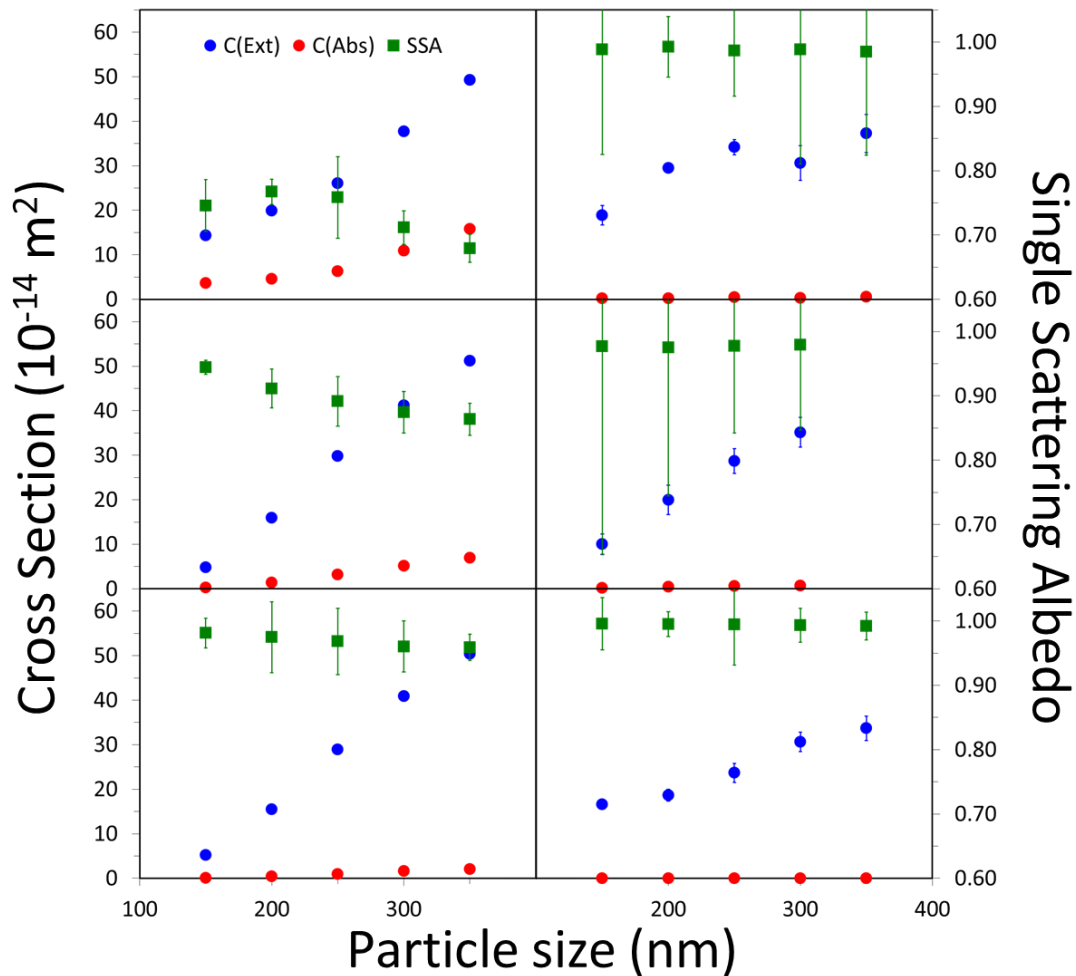
Figure 25: Summary of the optical properties measurements as a function of particle size. The left axis corresponds to the extinction cross section (blue circles) and the absorption cross section (red circles). The right axis corresponds to the single scattering albedo (green squares). The error bars correspond to the uncertainties of the measurements. The left column corresponds to the MG mixtures with MA (a), DA (c) and TA (e), while the right column corresponds to the GL mixtures with MA (b), DA (d) and TA (f).
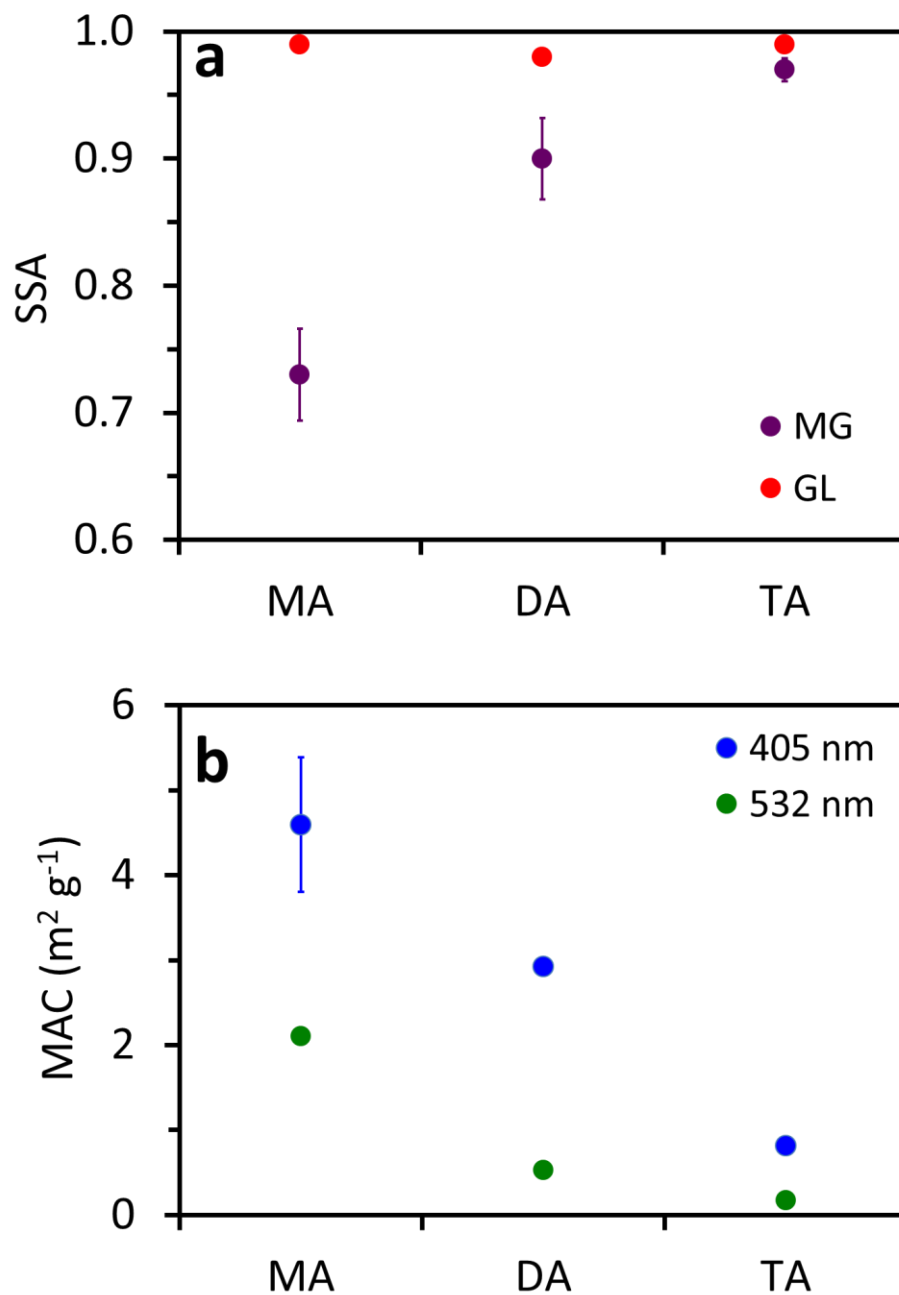
Figure 26: Dependence of the optical properties on amines. (a) Size average of SSA at 405 nm wavelength. (b) MAC values for the MG-amine mixtures for 250 nm particle size.

The wavelength dependence of MAC for 250 nm particle size is shown in Figure 26b for the MG samples. Note that measurements at the 532 nm wavelength are obtained using both PAX and a combination of a nephelometer and a custom-made cavity ring-down spectrometer [*Khalizov et al.*, 2009a]. There is an enhancement of light absorption by a factor of more than 2 at the shorter wavelength (i.e., 405 nm), which is characteristic of BrC. The sized averaged MAC values for all mixtures are also listed in Table 4, in the range of 0.079 to 4.83 g m^{-2}. Noting that the MAC value is inversely proportional to the density, according to equation (5). We measured the effective density for each particle size (table 3) and our average densities were considerably lower than those used for organic aerosols under ambient conditions (1.40 to 1.65 g cm^{-3}) [*Flores et al.*, 2014; *Nakao et al.*, 2013], therefore higher values from MAC are expected.

Table 3: Size-selected effective densities measurement for each mixture. The uncertainties correspond to the standard deviation.

Size (nm)	MG-MA	MG-DA	MG-TA	GL-MA	GL-DA	GL-TA
150	1.24	1.33	1.35	1.18	0.93	1.24
200	1.29	1.35	1.39	1.22	0.97	1.30
250	1.30	1.37	1.40	1.23	1.01	1.28
300	1.29	1.35	1.37	1.23	1.02	1.28
350	1.28	1.35	1.35	1.23	0.96	1.29
Average	1.28 ± 0.02	1.35 ± 0.01	1.37 ± 0.02	1.22 ± 0.02	0.98 ± 0.04	1.28 ± 0.02
Average	1.25 ± 0.14					

The RI values at 405 nm are determined according to equation (6), and the results are summarized in Table 4. The contour of the CFD values for the MG-MA mixture is plotted against n and k in Figure 27a. The reddest colors correspond to the lowest (best fit) CFD values. All CFD values are less than 0.01 (as shown in Figure 27a for MG-MA), indicating that the derived n and k values agree with the measured data within 1%. Both the real part (n, scattering) and the imaginary part (k, absorption) of the RI values are higher for the MG mixtures than for the analogue GL mixtures (Table 4). For example, the retrieved RI is 1.64 ($\pm$0.1) + 0.195i ($\pm$0.023) for MG-MA and 1.53 ($\pm$0.05) + 0.004i ($\pm$0.001) for GL-MA. The k values follow the same trend as the SSA values, similarly to the darkness of the solutions. The best-fit RI is employed to calculate C_{abs} as a function of particle size and is compared with the experimental data. Figure 27b shows a good agreement between the measured and calculated values of C_{abs} for MG-MA. Figure 28 shows a comparison of the C_{abs} values for all 6 mixtures. The C_{abs} values for the MG mixtures decrease with the methyl substitution (i.e., from primary to tertiary amines), and the values for the GL mixtures are about an order of magnitude lower. Some of the differences between the measured and calculated C_{abs} values may be explained by the assumption of monodisperse particles and doubled charged particles. Note that the C_{abs} values for GL-DA are larger than those for GL-MA. Interestingly, our measurements for the particle density also show the smallest density for GL-DA (0.98 g cm^{-3}), compared to the averaged value of 1.25 g cm^{-3} for all mixtures.
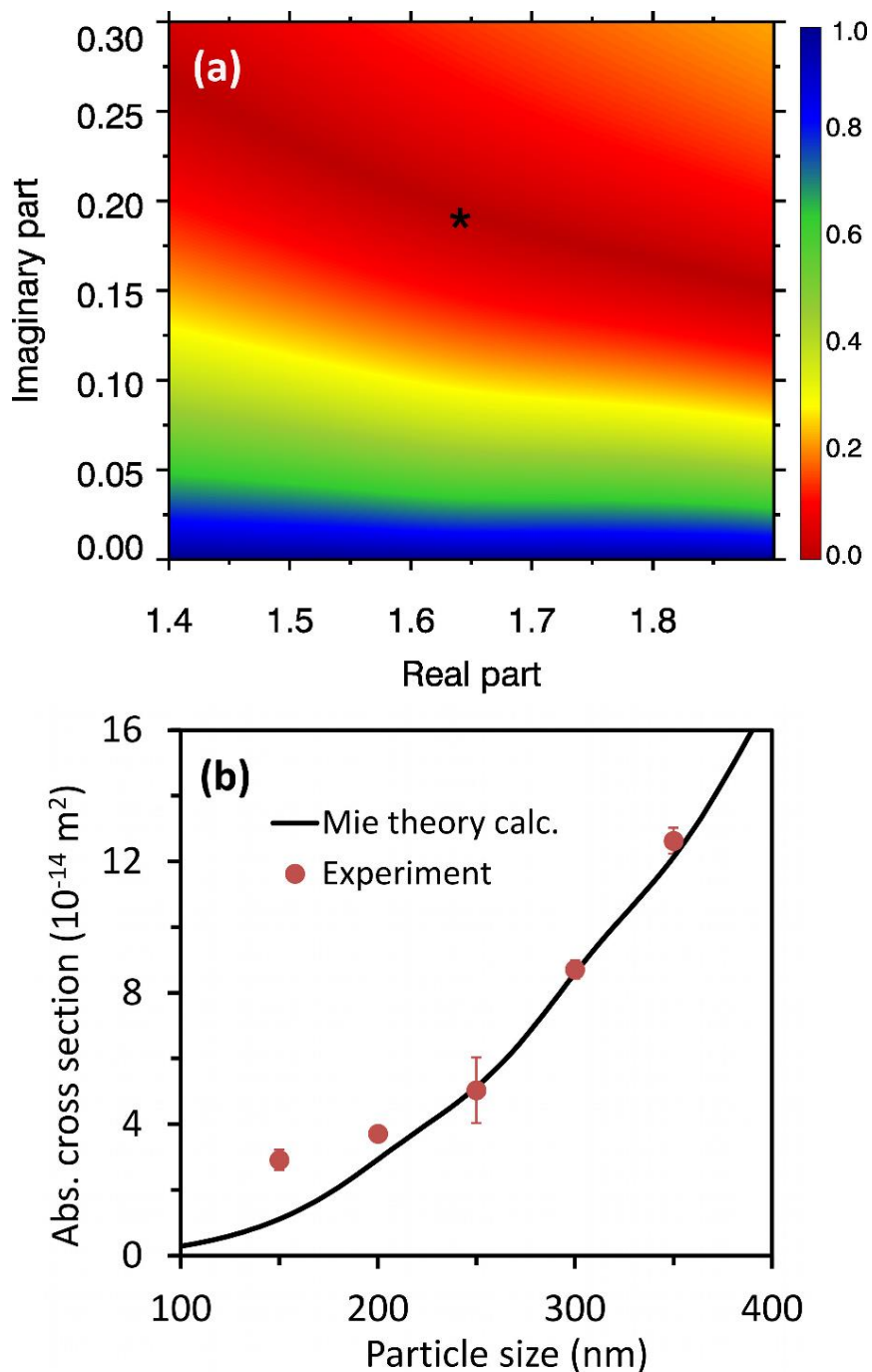
Figure 27: Derived refractive index and calculated absorption cross section using Mie theory. (a) Contour plot of CFD as a function of *n* (real part) and *k* (imaginary part) for MG-MA. The reddest color corresponds to the lowest CFD. (b) Comparison between the experimental and calculated *C*_{abs} as a function of particle size.
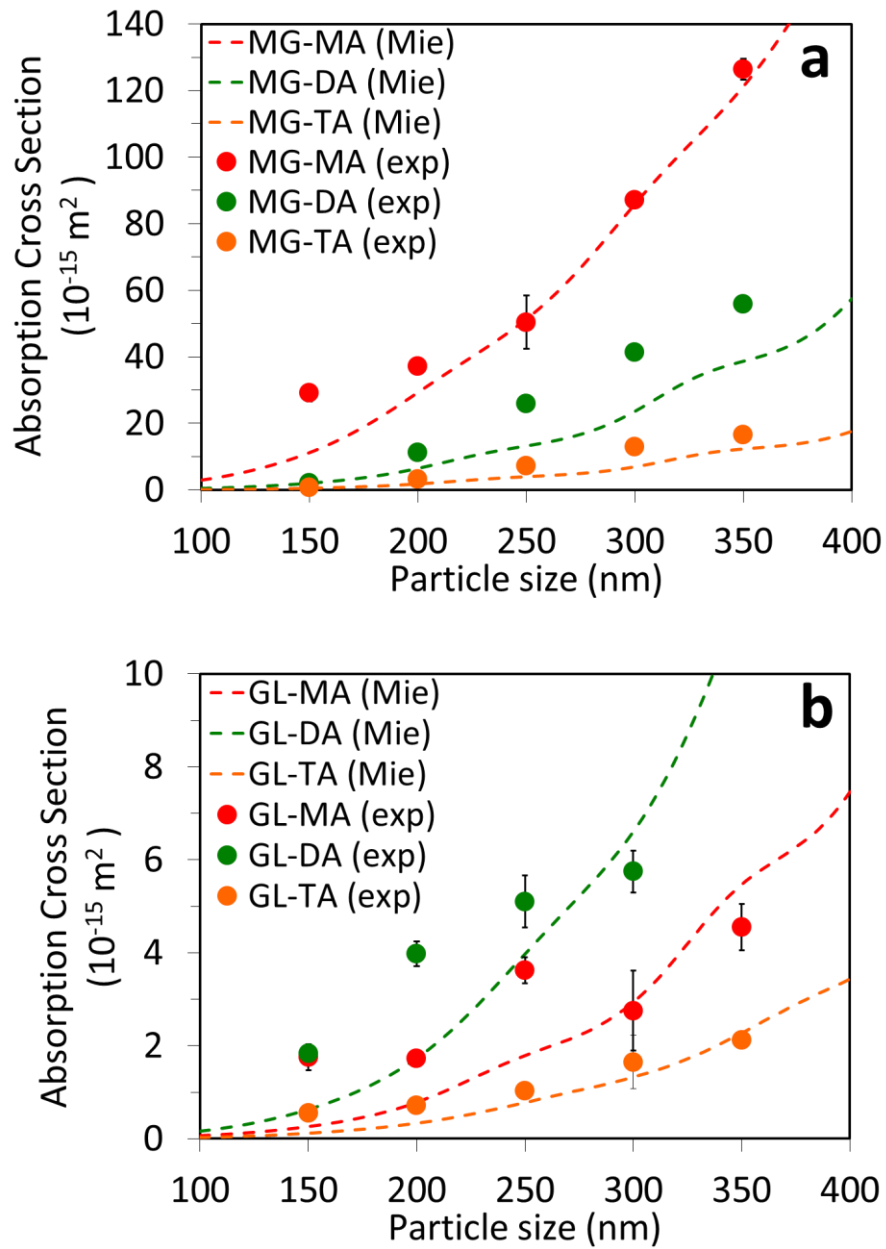
Figure 28: Absorption cross section experimental measurements (circles) and the MIE theory calculation fit (lines) for the MG mixtures (a) and the GL mixtures. The colors correspond to the different amines, MA (red), DA (green), and TA (orange).

Table 4: Summary of the refractive indexes retrieved together with the measured effective density and mass absorption cross section for each of the system. All values are for λ = 405 nm. For comparison we include the calculated bulk properties.

Mixtures[a]	MIE Theory		Experimental		Bulk Comparison [c]	
	n	k	ρ (g m^{-3}) [b]	MAC (m^2 g^{-1})	k_c	MAC_c (m^2 g^{-1})
MG-MA	1.64 ± 0.1	0.195 ± 0.023	1.28 ± 0.02	4.72 ± 0.3	0.195	4.73
MG-DA	1.60 ± 0.01	0.032 ± 0.006	1.35 ± 0.01	2.39 ± 0.2	0.104	0.74
MG-TA	1.58 ± 0.07	0.009 ± 0.001	1.37 ± 0.02	0.71 ± 0.1	0.031	0.20
GL-MA	1.53 ± 0.05	0.004 ± 0.001	1.22 ± 0.02	0.129 ± 0.04	0.005	0.10
GL-DA	1.44 ± 0.06	0.010 ± 0.002	0.98 ± 0.04	0.366 ± 0.12	0.012	0.32
GL-TA	1.41 ± 0.01	0.002 ± 0.001	1.28 ± 0.02	0.077 ± 0.01	0.003	0.02

[a] Mixture abbreviations correspond to MG-MA (methylglyoxal – methylamine), MG-DA (methylglyoxal – dimethylamine), MG-TA (methylglyoxal – trimethylamine), GL-MA (glyoxal – methylamine), GL-DA (glyoxal – dimethylamine), and GL-TA (glyoxal – trimethylamine).
[b] Size average of the measured effective densities. Average between systems is 1.25.
[c] Calculated using MAC = $4\pi k/\rho\lambda$.

The measurements show a large range of values for RI, i.e., 1.41 to 1.64 for the real part and 0.002 to 0.195 for the imaginary part for the various mixtures of α-dicarbonyls and amines. Except for MG-MA, the uncertainty for the real part of RI ranges from 0.01 to 0.07. The large uncertainty (0.1) for the real part of RI for MG-MA may be attributable to the fact that only absorption was employed in determining RI in our calculation. Zarzana et. al. [*Zarzana et al.*, 2012] reported the RI value of (1.55 + 0.114*i*) for MG-MA at 532 nm on the basis of extinction measurements, which is smaller than our values at 405 nm wavelength. Such a difference is explainable because absorption is enhanced at shorter wavelengths (Figure 26b). For ambient humic-like substances (HULIS), Dinar et al. [*Dinar et al.*, 2008] derived the RI values at 532 nm and 390 nm, which are within the ranges of our *k* values at 405 nm. For comparison, we also calculated the *k* using the equation for

bulk relationship ($MAC = 4\pi k/\rho\lambda$) and the MAC values obtained experimentally. Similarly, we calculate MAC using the k obtained via the MIE Theory Calculations. The values of MAC and k shown in table 4 are comparable to the ones obtained experimentally and MIE theory, respectively.

Because the reactions between the α-dicarbonyls and the amines lead to multiple products, the RI values determined from these experiments represent those of the various products within each mixture. However, errors likely occur when the RI for a mixture is determined from the RI of the individual components when k is not equal to zero [*Abo Riziq et al.*, 2007; *Freedman et al.*, 2009]. Most previous studies used the extinction data to retrieve RI, likely leading to large uncertainty, particularly for k [Zarzana et al., 2014]. Additionally, the uncertainty in the n values is large because the real component for absorbing aerosols is difficult to retrieve, especially at larger sizes [*Washenfelder et al.*, 2013].

Chemical Composition

In the present work, two complementary mass spectrometer techniques were used for the chemical composition analysis. The MG-MA and GL-MA spectra from the TD-ID-CIMS and the Orbitrap-MS are shown in Figure 29. The detail peak assignments are presented in Tables 5 – 10. For the same chemical composition, the spectra obtained with both techniques show similar peaks in the low mass range, i.e., 111 and 125 m/z for MG-MA and 143 m/z for GL-MA corresponding to the N-heterocycles. The TD-ID-CIMS shows well-defined peaks typically at the lower mass range, possible because of thermal decomposition. In contrast, the spectra from the Orbitrap-MS technique exhibit many

peaks in the high mass range, because the ionization method does not rely on thermal desorption. For the results of MG-MA using Orbitrap-MS, all the products with more than 20% relative intensity contain 6 to 8 carbon atoms for the estimated chemical formula; the product distribution corresponds mainly to dimers, instead of a combination of dimers and trimers. In general, the GL spectra are much cleaner than the MG spectra (Figure 29, 31 and 33), indicating lower reactivity of GL with amines.

The likely pathways leading to the identified products for MG-MA and GL-MA are illustrated in Figure 30 (see also Figures 32 and 34). The reactions likely involve nucleophilic attack of amines at the reactive carbonyl site, followed by dehydration before/after intermolecular cyclization of dimers or trimmers [*Kampf et al.*, 2016]. The dehydration likely regulates the kinetics for the reactions between α-dicarbonyls and amines [*Sedehi et al.*, 2013]. MG reacts quickly with the amines, leading to the formation of chromophores, which are identified as nitrogen-containing heterocycles (N-Heterocycles) by both the TD-ID-CIMS and Orbitrap-MS techniques. However, during drying, GL-dihydrate is converted into GL-monohydrate, yielding a carbonyl reactive site [*Galloway et al.*, 2009; *Loeffler et al.*, 2006]. For GL, there is a competing reaction between the hydration process and the nucleophilic attack of amines at the carbonyl site.

For MG, the N/C ratio is higher for the primary amines than for the tertiary amines, but the O/C ratio is higher for the tertiary amines (Table 11). These ratios are explained by the reactivity and steric effect of amines at the reactive carbonyl site. The Double Bond Equivalent (DBE) is proportional to the N/C ratio for MG. However, between α-dicarbonyls, the DBE is nearly identical, suggesting that the optical properties depend not only on the molecular structure but also on the supramolecular interaction.

69
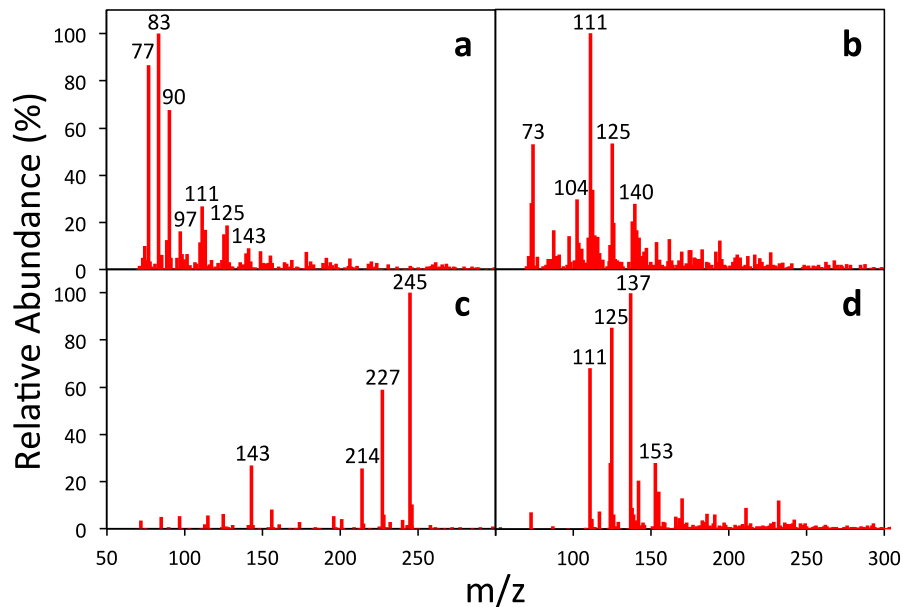
Figure 29: Mass spectra from two complementary methods for MA mixtures. TD-ID-CIMS spectra for (a) GL-MA and (b) MG-MA. Orbitrap-MS spectra for (c) GL-MA and (d) MG-MA.
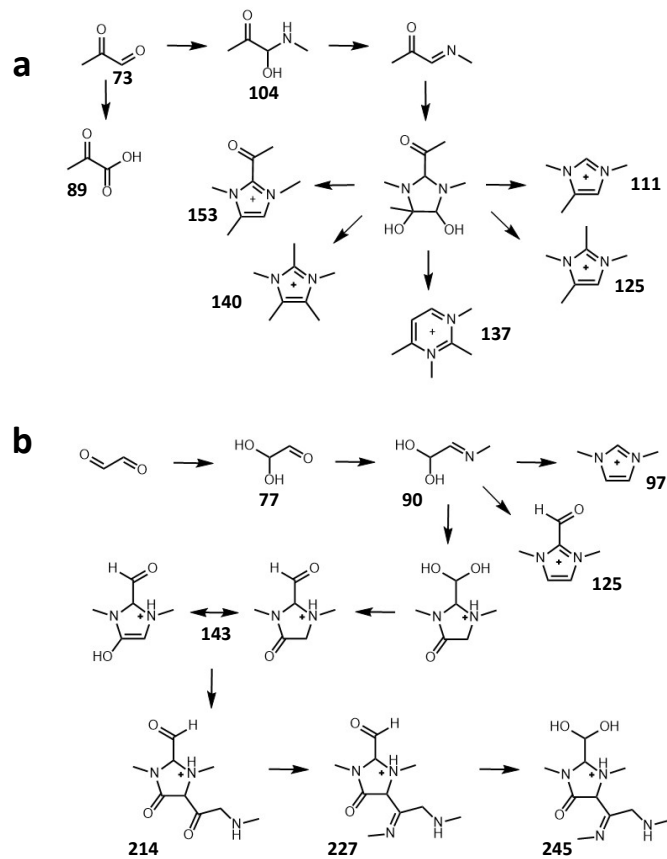
Figure 30: Proposed chemical mechanism for methylamine (MA) reaction with (a) methylglyoxal (MG) and (b) glyoxal (GL). The numbers correspond to the m/z.

70

Table 5: Peaks detected for MG-MA mixture with their corresponding mass to charge ratio (m/z), chemical formula, nitrogen to carbon ratio (N/C), oxygen to carbon ratio (O/C), hydrogen to carbon ratio (H/C), double bond equivalent (DBE) and aromaticity. The structures identified were in color red.

TD-ID-CIMS	Orbitrap-MS	m/z	Formula	N/C	O/C	H/C	DBE	Aromaticity
✔		73	$C_3H_5O_2$	0.00	0.67	1.67	1.5	0.3
✔		104	$C_4H_{10}O_2N$	0.25	0.50	2.50	0.5	-0.8
✔	✔	111	$C_6H_{11}N_2$	0.33	0.00	1.83	2.5	0.1
	✔	124	$C_7H_{10}ON$	0.14	0.14	1.43	3.5	0.4
✔	✔	125	$C_7H_{13}N_2$	0.29	0.00	1.86	2.5	0.1
	✔	137	$C_8H_{13}N_2$	0.25	0.00	1.63	3.5	0.3
✔		140						
	✔	153	$C_8H_{13}ON_2$	0.25	0.13	1.63	3.5	0.2
	✔	155	$C_8H_{15}ON_2$	0.25	0.13	1.88	2.5	0.0
	✔	170	$C_8H_{16}ON_3$	0.38	0.13	2.00	2.5	-0.2
	✔	232	$C_{13}H_{18}ON_3$	0.23	0.08	1.38	6.5	0.3
			Average	*0.24*	*0.18*	*1.78*	*2.90*	*0.06*

Table 6: Peaks detected for GL-MA mixture with their corresponding mass to charge ratio (m/z), chemical formula, nitrogen to carbon ratio (N/C), oxygen to carbon ratio (O/C), hydrogen to carbon ratio (H/C), double bond equivalent (DBE) and aromaticity. The structures identified were in color red.

TD-ID-CIMS	Orbitrap-MS	m/z	Formula	N/C	O/C	H/C	DBE	Aromaticity
✔		77	$C_2H_5O_3$	0.00	1.50	2.50	0.5	-2.00
✔		83						
✔		90	$C_3H_8O_2N$	0.33	0.67	2.67	0.5	-1.50
✔		97	$C_5H_9N_2$	0.40	0.00	1.80	2.5	0.17
✔		111						
✔		125	$C_6H_9ON_2$	0.33	0.17	1.50	3.5	0.29
✔	✔	143	$C_6H_{10}O_2N_2$	0.33	0.33	1.67	3.0	0.00
	✔	214	$C_9H_{15}O_3N_3$	0.33	0.33	1.67	4.0	-0.11
	✔	227	$C_{10}H_{18}O_2N_4$	0.40	0.20	1.80	4.0	-0.20
	✔	245	$C_{10}H_{20}O_3N_4$	0.40	0.30	2.00	3.0	-0.56
	✔	246	$C_{10}H_{20}O_3N_4$	0.40	0.30	2.00	3.0	-0.56
			Average	*0.33*	*0.42*	*1.96*	*2.67*	*-0.50*
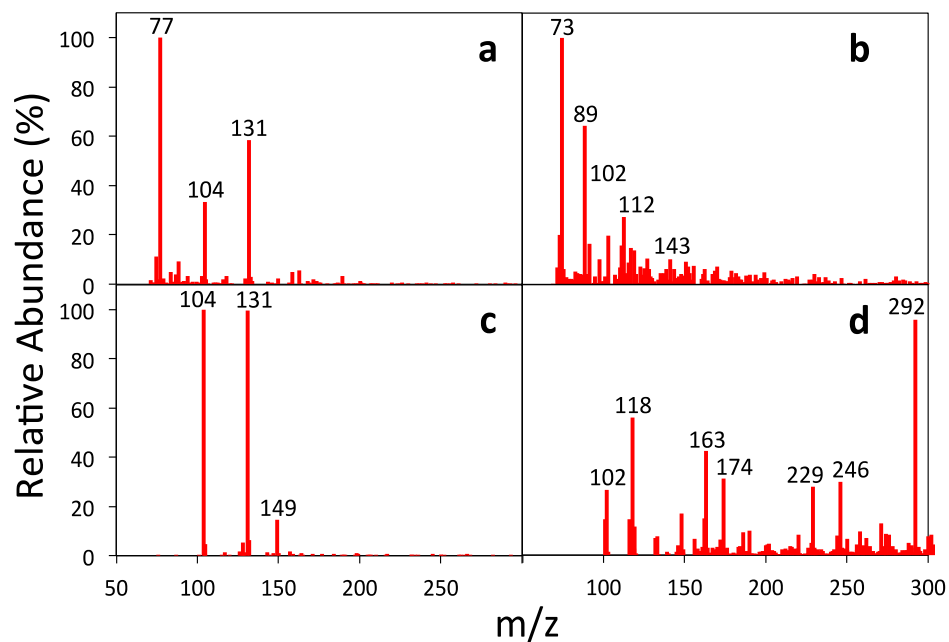
Figure 31: Mass spectra from the TD-ID-CIMS for GL-DA (a) and MG-DA (b), and with the mass spectra from the Orbitrap-MS for GL-DA (c) and MG-DA (d).
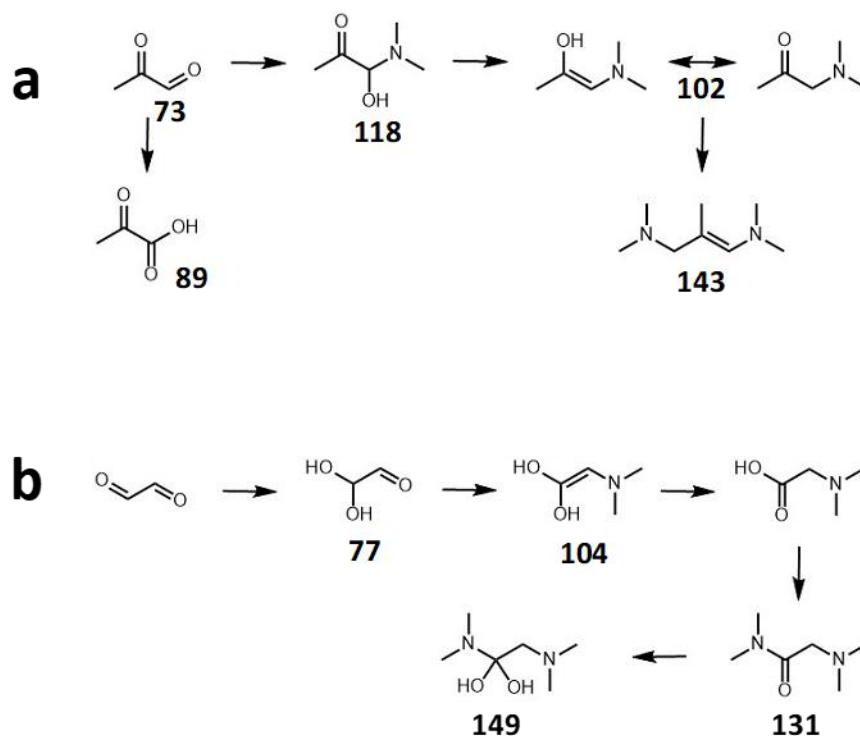
Figure 32: Proposed chemical mechanism for dimethylamine (DA) reaction with methylglyoxal (a) and glyoxal (b). The numbers correspond to the m/z.

Table 7: Peaks detected for MG-DA mixture with their corresponding mass to charge ratio (m/z), chemical formula, nitrogen to carbon ratio (N/C), oxygen to carbon ratio (O/C), hydrogen to carbon ratio (H/C), double bond equivalent (DBE) and aromaticity. The structures identified were in color red.

TD-ID-CIMS	Orbitrap-MS	m/z	Formula	N/C	O/C	H/C	DBE	Aromaticity
✔		73	$C_3H_5O_2$	0.00	0.67	1.67	1.5	0.3
✔		89	$C_3H_5O_3$	0.00	1.00	1.67	1.5	0.0
	✔	101	$C_5H_{13}N_2$	0.40	0.00	2.60	0.5	-0.5
✔	✔	102	$C_5H_{12}ON$	0.20	0.20	2.40	0.5	-0.3
✔		112						
	✔	116	$C_6H_{14}ON$	0.17	0.17	2.33	0.5	-0.2
✔	✔	118	$C_5H_{12}O_2N$	0.20	0.40	2.40	0.5	-0.5
	✔	119	$C_5H_{15}ON_2$	0.40	0.20	3.00	-0.5	-1.2
✔		143	$C_8H_{19}N_2$	0.25	0.00	2.38	0.5	-0.3
	✔	148	$C_6H_{14}O_3N$	0.17	0.50	2.33	0.5	-0.6
	✔	162	$C_7H_{16}O_3N$	0.14	0.43	2.29	0.5	-0.4
	✔	163	$C_7H_{19}O_2N_2$	0.29	0.29	2.71	-0.5	-0.9
	✔	174	$C_8H_{16}O_3N$	0.13	0.38	2.00	1.5	-0.2
	✔	229	$C_{11}H_{21}O_3N_2$	0.18	0.27	1.91	2.5	-0.1
	✔	246	$C_{11}H_{20}O_5N$	0.09	0.45	1.82	2.5	-0.1
	✔	271	$C_{13}H_{23}O_4N_2$	0.15	0.31	1.77	3.5	-0.1
	✔	292	$C_{12}H_{22}O_7N$	0.08	0.58	1.83	2.5	-0.3
		Average		*0.18*	*0.37*	*2.19*	*1.13*	*-0.34*

Table 8: Peaks detected for GL-DA mixture with their corresponding mass to charge ratio (m/z), chemical formula, nitrogen to carbon ratio (N/C), oxygen to carbon ratio (O/C), hydrogen to carbon ratio (H/C), double bond equivalent (DBE) and aromaticity. The structures identified were in color red.

TD-ID-CIMS	Orbitrap-MS	m/z	Formula	N/C	O/C	H/C	DBE	Aromaticity
✔		77	$C_2H_5O_3$	0.00	1.50	2.50	0.5	-2.00
✔	✔	104	$C_4H_9O_2N$	0.25	0.50	2.25	1.0	-0.50
✔	✔	131	$C_6H_{14}ON_2$	0.33	0.17	2.33	1.0	-0.43
	✔	149	$C_6H_{16}O_2N_2$	0.33	0.33	2.67	0.0	-1.00
		Average		*0.23*	*0.63*	*2.44*	*0.63*	*-0.98*
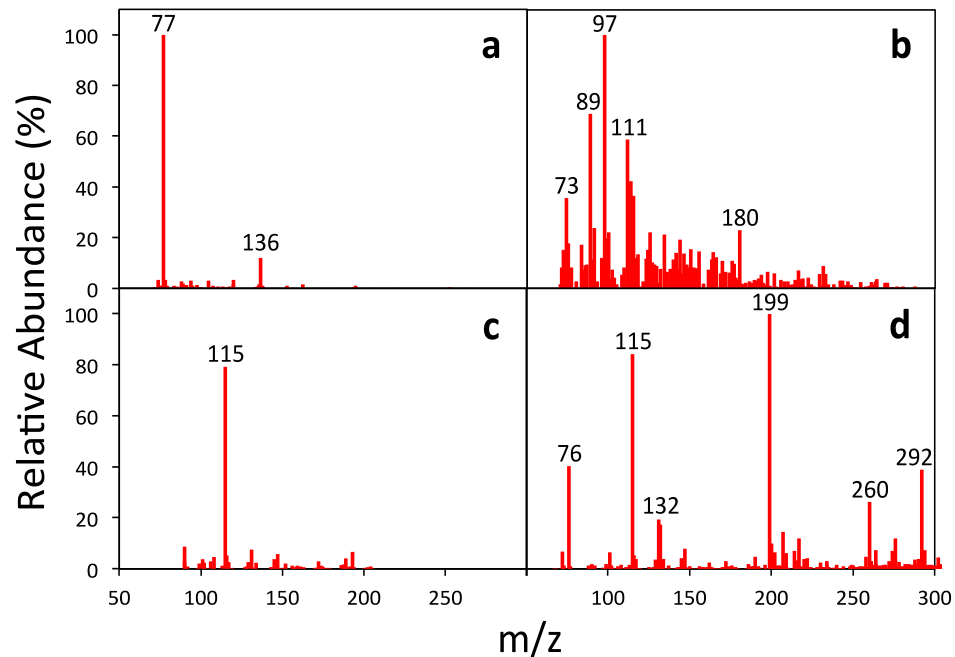
Figure 33: Mass spectra from the TD-ID-CIMS for GL-TA (a) and MG-TA (b), and with the mass spectra from the Orbitrap-MS for GL-TA (c) and MG-TA (d).
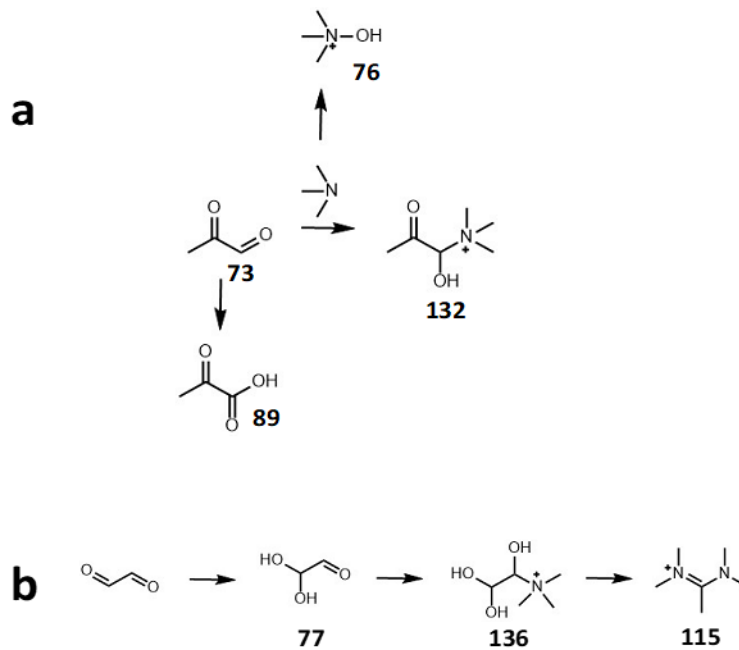
Figure 34: Proposed chemical mechanism for trimethylamine (TA) reaction with methylglyoxal (a) and glyoxal (b). The numbers correspond to the m/z.

Table 9: Peaks detected for MG-TA mixture with their corresponding mass to charge ratio (m/z), chemical formula, nitrogen to carbon ratio (N/C), oxygen to carbon ratio (O/C), hydrogen to carbon ratio (H/C), double bond equivalent (DBE) and aromaticity. The structures identified were in color red.

TD-ID-CIMS	Orbitrap-MS	m/z	Formula	N/C	O/C	H/C	DBE	Aromaticity
✔		73	$C_3H_5O_2$	0.00	0.67	1.67	1.5	0.3
	✔	76	$C_3H_{10}ON$	0.33	0.33	3.33	-0.5	-1.3
✔		89	$C_3H_5O_3$	0.00	1.00	1.67	1.5	0.0
✔		97						
✔		111						
	✔	115	$C_6H_{15}N_2$	0.33	0.00	2.50	0.5	-0.4
	✔	131	$C_6H_{11}O_3$	0.00	0.50	1.83	1.5	0.0
	✔	132	$C_6H_{14}O_2N$	0.17	0.33	2.33	0.5	-0.4
✔		180						
	✔	199	$C_9H_{11}O_5$	0.00	0.56	1.22	4.5	0.3
	✔	207	$C_9H_{23}O_3N_2$	0.22	0.33	2.56	-0.5	-0.7
	✔	217	$C_9H_{13}O_6$	0.00	0.67	1.44	3.5	0.1
	✔	260	$C_{12}H_{22}O_5N$	0.08	0.42	1.83	2.5	-0.1
	✔	276	$C_{12}H_{22}O_6N$	0.08	0.50	1.83	2.5	-0.2
	✔	292	$C_{12}H_{22}O_7N$	0.08	0.58	1.83	2.5	-0.3
	✔	332	$C_{15}H_{26}O_7N$	0.07	0.47	1.73	3.5	-0.1
	✔	348	$C_{15}H_{26}O_8N$	0.07	0.53	1.73	3.5	-0.2
		Average		*0.10*	*0.49*	*1.97*	*1.93*	*-0.21*

Table 10: Peaks detected for GL-TA mixture with their corresponding mass to charge ratio (m/z), chemical formula, nitrogen to carbon ratio (N/C), oxygen to carbon ratio (O/C), hydrogen to carbon ratio (H/C), double bond equivalent (DBE) and aromaticity. The structures identified were in color red.

TD-ID-CIMS	Orbitrap-MS	m/z	Formula	N/C	O/C	H/C	DBE	Aromaticity
✔		77	$C_2H_5O_3$	0.00	1.50	2.50	0.5	-2.00
	✔	115.12	$C_6H_{15}N_2$	0.33	0.00	2.50	0.5	-0.38
✔		136	$C_5H_{14}O_3N$	0.20	0.60	2.80	-0.5	-1.20
		Average		*0.18*	*0.70*	*2.60*	*0.17*	*-1.19*

Table 11: Summary of the average nitrogen to carbon ratio (N/C), oxygen to carbon ratio (O/C), hydrogen to carbon ratio (H/C), double bond equivalent (DBE), aromaticity, and single scattering albedo (SSA) per mixture

	N/C	O/C	H/C	DBE	Aromaticity	SSA
MG-MA	0.24	0.18	1.78	2.90	0.06	0.73
MG-DA	0.18	0.37	2.19	1.13	-0.34	0.90
MG-TA	0.10	0.49	1.97	1.93	-0.21	0.97
GL-MA	0.33	0.42	1.96	2.67	-0.50	0.99
GL-DA	0.23	0.63	2.44	0.63	-0.98	0.98
GL-TA	0.18	0.70	2.60	0.17	-1.19	0.99

Atmospheric Implications

BrC represents an important component of atmospheric fine aerosols and affects the Earth's radiative balance, directly by interfering with solar and terrestrial radiation and indirectly by altering cloud formation and microphysics. In this work, BrC particles containing the mixtures of small α-dicarbonyls and amines were synthesized, and the optical properties of BrC particles were measured. The single scattering albedo for MG is smaller than that of GL and increased with methyl substitution of amines. The extinction and absorption cross-sections increase with the particle size from 150 nm to 350 nm. The mass absorption cross-section for MG are two times higher at 405 nm wavelength than that at 532 nm wavelength. The refractive indexes at the 405 nm wavelength are in the range of 1.40-1.64 for the real part and 0.002-0.195 for the imaginary part. The analysis of the chemical composition of the α-dicarbonyl-amine mixtures with two complementary techniques reveals that N-heterocycles are the dominant chemical composition.

76

To evaluate the impact of the optical properties and radiative forcing of BrC particles, a modified version of the Chylek and Wong equation [*Bohren and Huffman*, 2004; *Zarzana et al.*, 2012] is used to estimate the relative forcing (ΔF_{rel}). The ΔF_{rel} values for the six α-dicarbonyl-amine mixtures as a function of the particle size are shown in Figure 35, with the positive and negative values representing warming and cooling, respectively. Also, for comparison, four additional cases are considered using the RI values previously reported at the 405 nm wavelength, including ambient nucleation ($1.55 + 0i$) [*Peng et al.*, 2016], chamber nucleation of α-pinene-OH photo-oxidation ($1.40 + 0i$) [*Lambe et al.*, 2013], suwanee river fulvic acid (SRFA, $1.68 + 0.05i$) [*Washenfelder et al.*, 2013], and BC ($1.95 + 0.79i$) [*Bond et al.*, 2013]. All results examined in this study are within the range of BC (most absorbing) and nucleation of organic aerosols (less absorbing, mainly scattering).

The MG mixtures exhibit significantly less cooling than that for the GL mixtures. The MG-MA mixture shows a warming effect similar to that of BC, whereas the other five cases show a cooling effect. For particles size less than 300 nm, the magnitude of cooling is similar for most of the α-dicarbonyl-amine mixtures (except for MG-MA), but for particle larger than 500 nm, the ΔF_{rel} values are distinct for the various mixtures. SRFA and MG-DA show a cooling effect for small sizes but a warming effect for larger sizes. Hence, the results indicate that BrC aerosols formed from MG-MA likely contributes to significant atmospheric warming. The results may be more applicable to urban areas because of high concentrations of the aerosol gaseous precursors, i.e., those for the aged pollution plume [*Flowers et al.*, 2010], HULIS (urban and rural) [*Dinar et al.*, 2008], biomass burning [*Lack et al.*, 2012], urban plume [*Cappa et al.*, 2012; *Guo et al.*, 2014], or

for newly formed SOA [*Lambe et al.*, 2013]. While a full radiative transfer atmospheric model is needed to accurately determine the direct radiative forcing for BrC particles, the results provide the key optical properties (i.e., size-dependent SSA, MAC, and RI) for incorporation of the α-dicarbonyl-amine mixtures into atmospheric models.
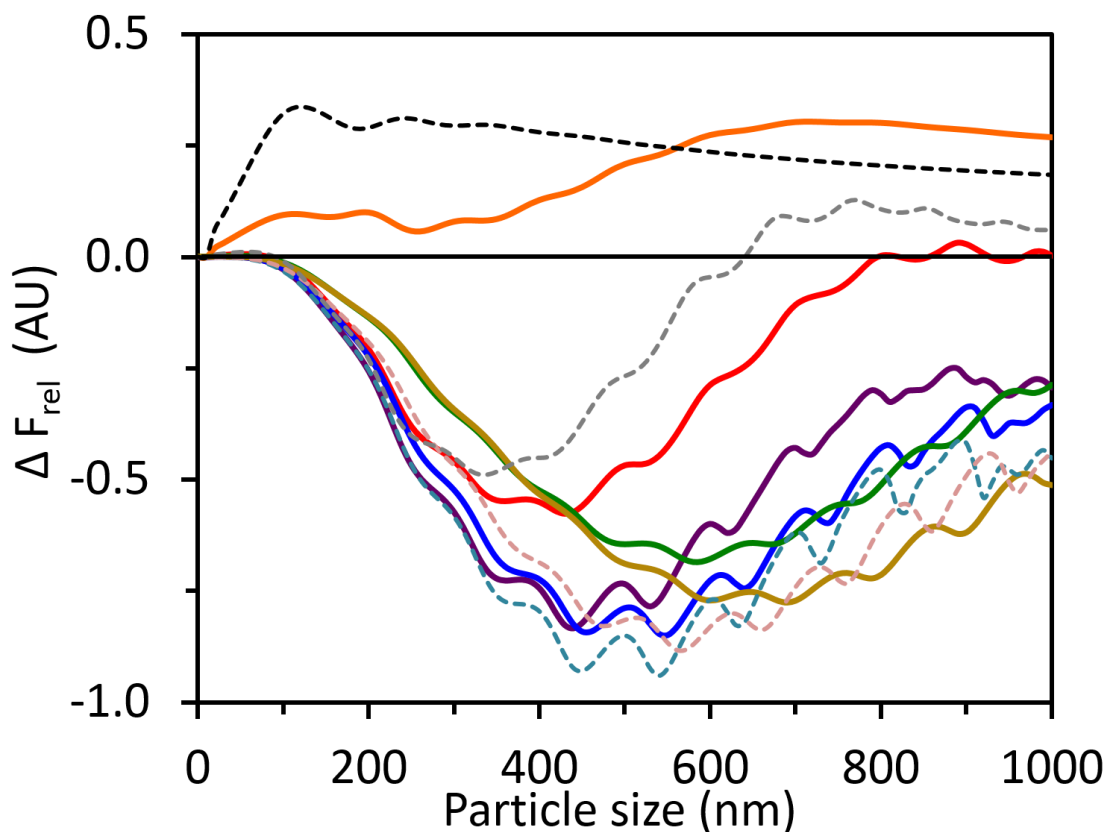
Figure 35: Relative forcing ratios (solid lines) calculated from the complex refractive index at 405 nm wavelength as a function of particle size. Positive and negative values indicate net warming and cooling effects, respectively. MG-MA (orange), MG-DA (red), MG-TA (purple), GL-MA (blue), GL-DA (green), and GL-TA (olive). The dashed lines represent published values for BC (black), SRFA (gray), ambient NPF (light blue), and chamber NPF (light pink).

CHAPTER V

UPTAKE OF AMINES WITH DICARBOXYLIC ACIDS RELEVANT TO

SECONDARY ORGANIC AEROSOLS: A FLOW TUBE STUDY

Introduction

Heterogeneous reactions of volatile organic compounds (VOCs) lead to the

formation of secondary organic aerosols (SOAs) and aerosol growth, which are not well

understood [*Abbatt et al.*, 2012; *George and Abbatt*, 2010; *Ravishankara*, 1997; *Shen et

al.*, 2013]. This type of reaction could alter physical and chemical properties such as

hygroscopicity, thermal stability, nucleation ability, and optical properties—resulting in

different implications to the climate. Moreover, the inability to account for complex

heterogeneous chemistry may lead to an underprediction of ambient SOA by atmospheric

models [*Heald et al.*, 2005; *Volkamer et al.*, 2006].

Amines are important organic components of atmospheric aerosols globally and

account for up to 20% of organic aerosols [*Docherty et al.*, 2011; *Qiu and Zhang*, 2013].

Amines are emitted from various biogenic sources (e.g., ocean organisms, protein

degradation, and biomass burning) and anthropogenic sources (e.g., animal husbandry,

automobiles, industry, and sewage/waste treatment) [*Ge et al.*, 2011]. Low-molecular-

weight aliphatic amines, such as methylamine (MA), dimethylamine (DA), and

trimethylamine (TA), are the most abundant, with global emissions of 83 ± 26, 33 ± 19, and

169 ± 33 Gg N y^{-1}, respectively [*Cornell et al.*, 2003; *Ge et al.*, 2011]. Based on field

measurements, laboratory measurements, and theoretical studies, amines are involved in

the nucleation and growth of aerosols [*Qiu and Zhang*, 2013; *Wang et al.*, 2010b; *Zhang et al.*, 2012]. For example, amines can enhance aerosol nucleation in the sulfuric acid-water system more effectively than ammonia by forming more stable clusters [*Kurtén et al.*, 2008]. Additionally, organic aminium salts found in ambient particles explain 23% and 47% of observed new-particle-formation events in the cities of Hyytiala, Finland and Tecamac, Mexico, respectively [*Smith et al.*, 2010]. The very presence of aminium salts in newly formed particles provides evidence of organic acid-amine interactions and also indicates that they may play an integral role in the early development of secondary aerosols. Moreover, because of their volatility, amines undergo heterogeneous reactions (gas-solid interaction) faster than multiphase reactions (gas-liquid interaction) [*Abbatt et al.*, 2012; *Davidovits et al.*, 2006; *Ravishankara*, 1997]. Also, due to their basicity, amines can participate in acid-base reactions with acidic aerosols. Thus, gaseous amines undergo heterogeneous reactions with particle-phase acids (organic and inorganic) to form salt particles.

Dicarboxylic acids (diacids) are the most abundant type of organic acid in the atmosphere and have been found in several regions around the world [*Kawamura et al.*, 1996; *Limbeck et al.*, 2005]. The general formula for diacids is $HOOC—(CH_x)_n—COOH$, where x is the number of hydrogens and n is the number of carbons in the chain length. Several structural types of diacids have been detected with additional functional groups, such as hydroxyls [*Bilde et al.*, 2015]. Diacids also play an important role in the nucleation and growth of aerosols. Although diacids are classified as water-soluble organic compounds, the most abundant diacids have a deliquescence point higher than 70% RH [*Bilde et al.*, 2015; *Prenni et al.*, 2001]. Thus, diacids are likely to exist in the aerosol

80

particle phase, allowing them to serve as available sites for heterogeneous reactions in dry conditions.
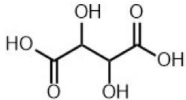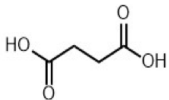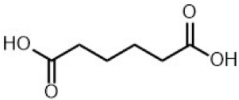
The acid-base neutralization of prevalent diacids by low-molecular-weight amines results in the formation of low-volatility aminium carboxylate salts in atmospheric particles [*Barsanti et al.*, 2009; *Gomez-Hernandez et al.*, 2016; *Lavi et al.*, 2015]. Therefore, it is expected that diacid ions often coexist with aminium ions in the aerosol particle phase [*Schlag et al.*, 2017; *Smith et al.*, 2010]. As a consequence, a deeper understanding of the diacid-amine interaction at a molecular level is imperative. Also, heterogeneous acid-base reactions have been understudied in the atmospheric chemistry field when compared with oxidations.

In 2012, Lui et al. [*Liu et al.*, 2012] investigated the heterogeneous uptake of MA, DA, and TA at 298 K by citric and humic acid utilizing a Knudsen cell reactor coupled to a quadrupole mass spectrometer. The acid-base reactions were confirmed, resulting in observed uptake coefficients ranging from $(6–7) \times 10^{-3}$, and $(5–15) \times 10^{-6}$ for citric and humic acid, respectively. However, the uptake coefficients for citric acid showed a sample-mass-independent behavior, while the uptake coefficient for humic acid increased linearly with sample mass. While steric effects governed the reactivity between amines and organic acids, citric acid demonstrated a higher reactivity than humic acid because it had a stronger acidity. Recently, Fairhurst and coworkers [*Fairhurst et al.*, 2017a; *Fairhurst et al.*, 2017b] studied the reaction of gaseous amines (methylamine, ethylamine, dimethylamine, trimethylamine) with a series of solid dicarboxylic acids (malonic acid, succinic acid, glutaric acid, adipic acid, pimelic acid), and their uptake coefficients ranged from 0.7 to less than 10^{-6}. Their studies also revealed an odd-even carbon dependence, being larger for

the odd carbon diacid, and their increase was related to the formation of ionic liquid layers

in the surface. Moreover, they explained the importance of the diacid crystal structure

since neither basicity nor structure is enough to explain the effect of amine uptake.

However, no previous study has assessed systematically the role of multifunctional groups,

like hydroxyl and carbon chain lengths, in the diacid behavior in heterogeneous reactions.

In this study, the growth of SOAs was investigated by measuring the heterogeneous

uptake of amines (MA, DA, and TA) by particle-phase Tartaric (TarAc), Succinic (SucAc),

and Adipic (AdiAc) acids employing an ion drift chemical ionization mass spectrometer

(ID-CIMS). The acidic species were chosen because of their atmospheric prevalence,

solubility, and low vapor pressures, as well as to systematically asses the role of the

functionality groups (hydroxyl vs. chain length) [*Bilde et al.*, 2015]. Relevant physical

properties of the diacids and amines used for this study are in table 12 and 13. The

heterogeneous reaction kinetics were expressed as uptake coefficients, γ, describing the

probability in which gas phase amines will be lost due to collisions with the stationary acid

particles [*Abbatt et al.*, 2012; *Davidovits et al.*, 2006]. The resulting kinetic data provides

insight into whether the proposed acid-base neutralization reactions are feasible and occur

at a rate that expedites the growth of new and existing aerosols.
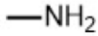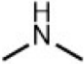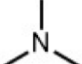
Table 12: Physical properties of the Dicarboxylic Acids (diacids).

	Tartaric Acid	Succinic Acid	Adipic Acid
Molecular Weight[a]	150.087 g mol^{-1}	118.089 g mol^{-1}	146.141 g mol^{-1}
Density[a]	1.79 g cm^{-3}	1.57 g cm^{-3}	1.36 g cm^{-3}
pK$_a$[a]	2.98 (4.34)	4.21 (5.64)	4.41 (5.41)
Water Solubility[b]	150 g L^{-1}	83.5 g L^{-1}	23 g L^{-1}

a, from CRC handbook
b, from Sigma Aldrich

Table 13: Physical properties of the Aliphatic Alkylamines (amines)

	Methylamine	Dimethylamine	Trimethylamine
Molecular Weight[a]	31.058 g mol^{-1}	45.084 g mol^{-1}	59.110 g mol^{-1}
Density[a]	0.656 g cm^{-3}	0.6804 g cm^{-3}	0.627 g cm^{-3}
pK$_b$[a]	3.34	3.27	4.20

a, from CRC handbook

Methodology

Heterogeneous reactions were studied using a low-pressure, fast-flow reactor

coupled to an ID-CIMS (Figure 36) [*Qiu et al.*, 2011; *Zhang and Zhang*, 2005]. As

depicted in Figure 36, a sandblasted glass cylinder tube coated with 5 to 40 mg of acid is

inserted into a 33-cm-long Pyrex flow reactor for heterogeneous uptake measurements.

The independent uptake experiments were performed under dry conditions at 298 K at an

average flow reactor pressure between 1.4 and 1.6 torr with a total flow velocity of 490 to

560 cm s^{-1}.
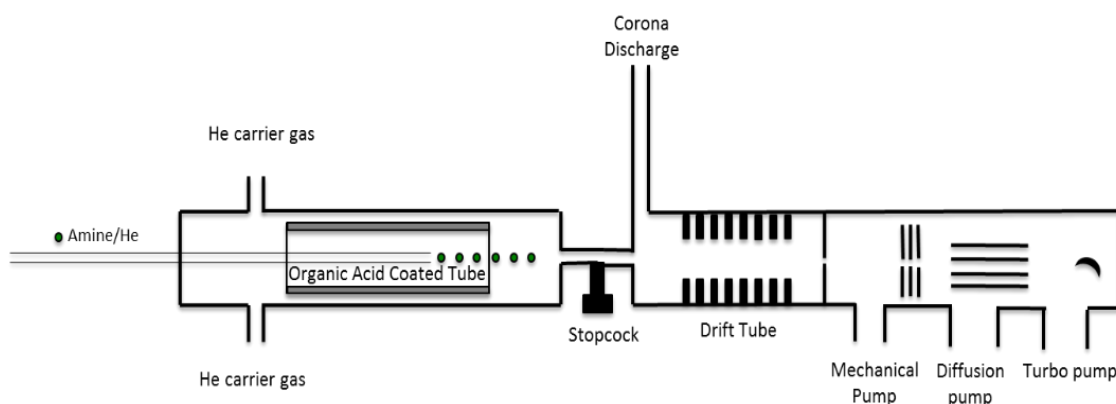
Figure 36: Schematic representation of the laminar fast-flow reactor coupled to the ID-CIMS.

The organic acid coatings were prepared with 10 – 30 wt% aqueous organic acid

solution, either TarAc (Sigma-Aldrich, ≥99.5%), SucAc (Sigma-Aldrich, ≥99.0%), or

Adipic (Sigma-Aldrich, ≥99%). Briefly, the sandblasted glass cylinder tube was held

vertically in the small beaker containing the acid solution, and only about 0.5 cm was

immersed [*Qiu et al.*, 2011]. A vacuum line with a critical orifice was connected to the other opening of the tube. The coating solution was drawn up to about 12 cm into the tube and allowed to drain back into the beaker. This process was repeated multiple times, depending on the final coating mass desire. Then, the coated tube was oriented horizontally, externally wiped to remove any excess solution, and dried with a particle-free N_2 flow. The dried tube resulted in a crystalline acid layer from 5 to 40 mg.

Anhydrous MA (Sigma-Aldrich, $\geq 98\%$), DA (Sigma-Aldrich, $\geq 99\%$), and TA (Sigma-Aldrich, $\geq 99\%$) anhydrous gases were diluted with ultrahigh-purity helium by a two-step dilution, and the final pressure was about 800 torr. The final dilution resulted in a mixing ratio of ~100 to 150 ppm. The concentration of the amine gas within the flow reactor was maintained on the order of 10^{-10} molecules cm^3 and a partial pressure of about 10^{-7} torr. Because the alkylamine gases did not stream from an online source, signal loss could be observed over the course of a single trial. To keep this loss at a minimum, the amine bulbs were replenished following nine independent experiments. Compressed helium was employed as the carrier gas, and all gas flows were monitored using calibrated electronic mass flow meters (Millipore Tylan 260 series). The combined gas flows exhibited flow velocities within 490 to 560 cm s^{-1}.

The ID-CIMS system has been previously described [*Fortner et al.*, 2004]. Two complementary ionization schemes were employed to evaluate the kinetics and mechanism of the heterogeneous reactions. Single-ion monitoring of the protonated amine signals was performed using a proton transfer ionization and protonated acetone monomer:

$$A + H_3O^+ \rightarrow AH^+ + H_2O$$

$$A + (C_3H_6O) \cdot H^+ \rightarrow (C_3H_6O) \cdot A \cdot H^+$$
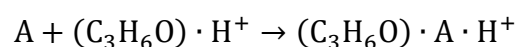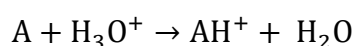
where A represents the unprotonated and AH^+, and $(C_3H_6O){\cdot}A{\cdot}H^+$ represents the protonated forms of the amine. The reagent ions were produced by flowing charcoal-filtered ambient air into a corona discharge ionization source. The hydronium ions then reacted with the amine molecules in the drift tube, followed by analyses using a quadrupole mass spectrometer. The signal intensities of the protonated MA, DA, and TA were monitored at protonated peaks of 32, 46, and 60 m/z, respectively. The H_3O^+ ions were monitored at 19 m/z in order to account for any fluctuations in the amine signal due to an unstable reagent ion flow. Sometimes the use of the protonated acetone monomer signal (59 m/z) was employed to obtain a better signal-to-noise ratio on the MA detection (90 m/z). To create the acetone reagent ion, a similar method for the hydronium ion was used, but with a bubbler containing acetone between the charcoal filter and the ionization source.

The flow reactor utilized a moveable injector, which facilitated amine exposure to the organic acid samples. The selectively monitored amine signal was used to measure the heterogeneous kinetics of the amine loss expressed as the initial-state, γ_0, and steady-state, γ_{ss}, uptake coefficients by employing the equation [*Qiu et al.*, 2011; *Zhang et al.*, 1994]:

$$\gamma = \frac{2rk_r}{\omega + rk_r} \qquad (8)$$

where r is the radius of the sample tube, ω is the mean thermal speed, and k_r is the pseudo-first-order rate constant. The pseudo-first-order rate constant (k_r) was calculated from the equation:

$$\frac{1}{k_{obs}} = \frac{1}{k_r} + \frac{1}{k_{diff}} \tag{9}$$

where k_{obs} is the observed first-order rate constant, and k_{diff} is the rate constant due to the gas phase diffusion of amines to the flow reactor wall [*Gershenzon et al.*, 1995; *Hanson et al.*, 1992] and is calculated using a diffusion coefficient ($D_{amine/He}$) estimate [*Fuller et al.*, 1966]:

$$k_{diff} = \frac{3.66 \times D_{amine/He}}{r^2} \tag{10}$$

The observed first-order rate constant (k_{obs}) is given by Equation 11:

$$k_{obs} = \frac{u}{l} \ln\left(\frac{I_o}{I_t}\right) \tag{11}$$

where u is the total carrier flow velocity, l is the distance that the injector is moved toward the sample tube, I_o is the initial signal intensity of the amine, and I_t is the intensity at a given time [*Qiu et al.*, 2011]. The total amine signal was corrected for background and unstable amine flow before performing the calculations.

Results and Discussion

Uptake experiments were performed by exposing the solid acid surface to the amine vapor while monitoring the protonated amine signal using the ID-CIMS. Figure 37 shows an example of the temporal profile behavior depending on the distance that the injector was moved inside the acid coating tube. Once a stable signal of the amines was achieved, the movable injector was withdrawn to expose the acid coating. Upon immediate exposure to the diacid surface, the amine signal decreased and gradually followed a recovery of the signal until reaching a steady state. The initial amine signal loss is indicative of the presence of easily accessible sites on the diacid surface, such as steps, edges, and defects. The asymptotic recovery to reach steady state after the initial signal loss indicates that the diacid coating was not completely saturated with amines. After a steady-state signal was achieved, the exposure was terminated by returning the movable injector to its initial position, resulting in an abrupt increase (desorption peak) of the amine signal and gradually decreasing to about the original intensity. Because the accommodation of gas molecules on a solid surface comprises both physical adsorption and surface reaction, the observation suggests a slower surface reaction rate than that of accommodation. Because physical adsorption is reversible, the desorption peak indicates the release of the adsorbed amines on the surface back to the gas phase. However, the desorption peaks have a smaller area than that of the uptake curve. Therefore, a significant fraction of the gas phase amines is irreversibly lost due to reactive uptake, while the remaining fraction of the lost amine signal was a result of the physical adsorption. Moreover, as the injector distance increases (i.e., moves toward the inside of the tube), the

more solid acid surface is available to react with the amines; therefore, a lower initial signal was observed. Also, it takes more time to reach a stable steady-state signal as the distance increases. Likewise, since the signal loss of each amine increases with the injector distance, it could be assumed that the acid-base interactions are time-dependent.
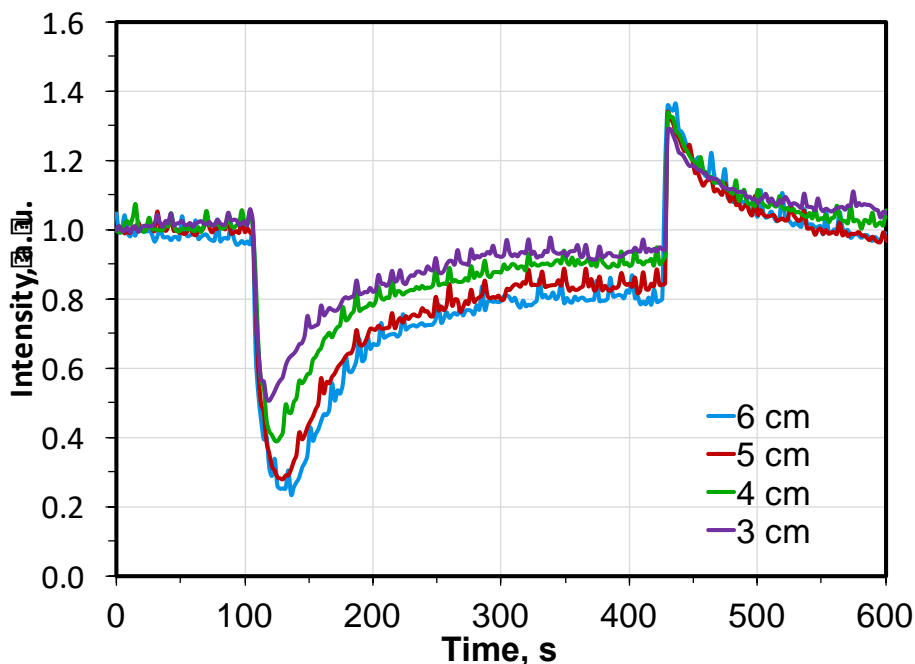
Figure 37: Normalized methylamine ($C_3H_6O \cdot [MA] \cdot H^+$) signal loss when exposed to 8-mg coating of succinic acid at several distances. As the exposure distance increases, the initial loss is greater and takes longer time to reach the steady state.

At the same distance, Figure 38 depicts the loss in amine signal intensity upon exposure to the diacid coating, with each row and column representing a different amine and diacid, respectively. All of the systems shared similar features with the signal loss and recovery, but the intensities varied. The initial loss for the TA signals was lower than the DA and MA signals with their respective acids. Also, the AdiAc samples showed a small

loss and rapid recovery, indicating a lower reactivity with all the amines compared with TarAc and SucAc.

To assess the kinetics of the acid-base neutralization reactions at steady state, the exposure distance was converted into a contact time between the amines and diacids. The decay of the amine signal was plotted as a function of the contact time (Figure 39). The purple circles, orange squares, and green diamonds correspond to TarAc, SucAc, and AdiAc, respectively, under similar experimental conditions with the same amine. The slope of the linear regression (forcing the intercept on zero) determines the observed first-order rate constant (k_{obs}) for each reaction. All decays follow the first-order kinetics, and the reaction rate increases with the O/C ratio for the same amine. The steady-state uptake coefficients were calculated from the first-order rate constants (k_r) with the gas diffusion corrections (k_{diff}). The gas diffusions (k_{diff}) were orders of magnitude larger than k_{obs}; therefore, this type of gas-solid interaction is not diffusion-controlled. The heterogeneous reaction rate is dependent on several factors such as mass transfer of the gas to the solid surface, adsorption of the gas on the surface, and chemical reaction rate [*Abbatt et al.*, 2012; *Davidovits et al.*, 2006]. Similar calculations were made for the kinetics of the initial exposure; however, this is more dependent on the experimental conditions rather than the identity and reactivity of the acid-base reaction.
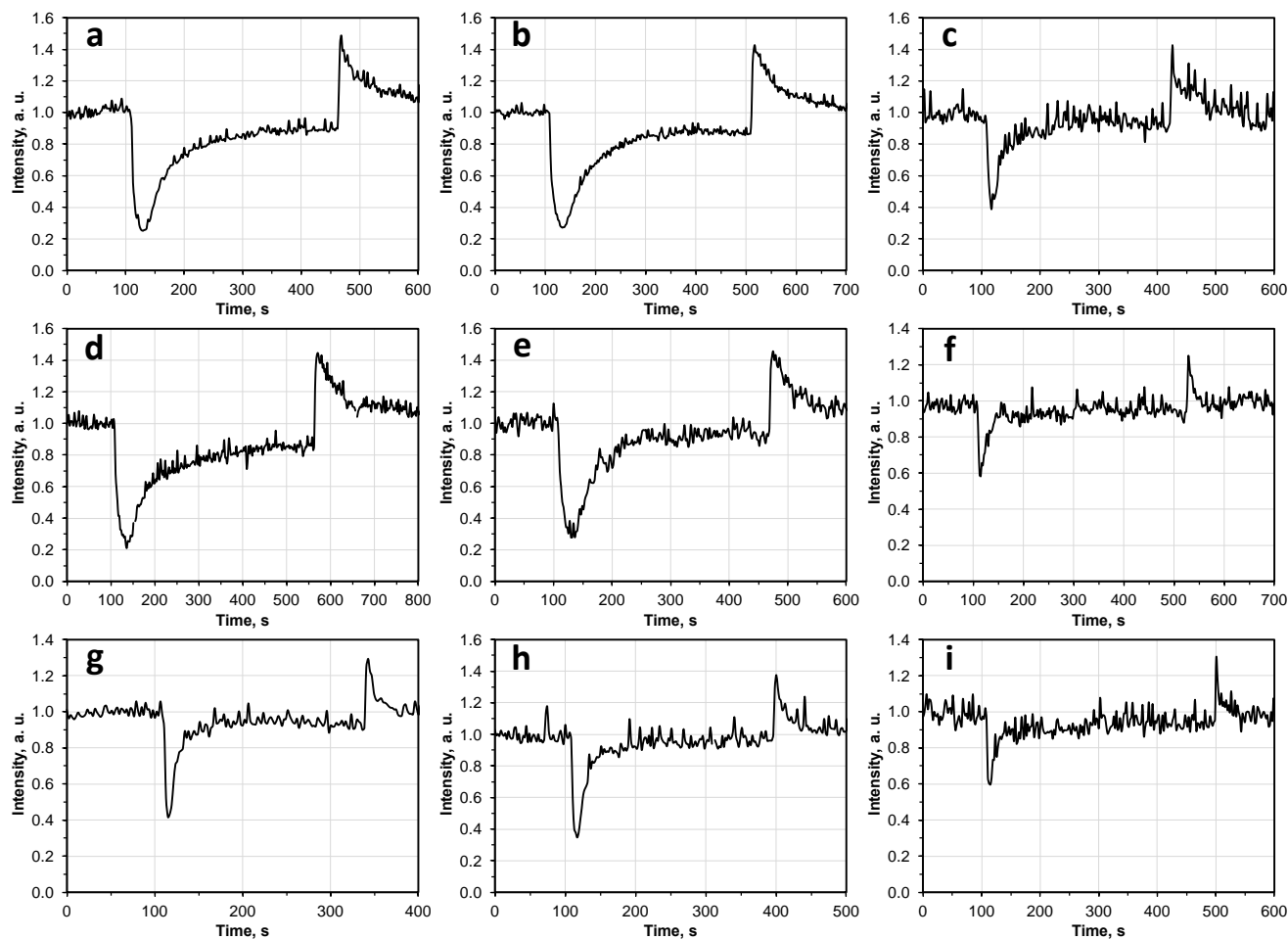
Figure 38: Normalized selected ion mass spectral profiles of amine signal loss when exposed to 5 cm of solid diacids at 298 K. The first (a, d, g), second (b, e, f), and third (c, f, i) columns represent tartaric acid, succinic acid, and adipic acid, respectively. The first (a, b, c), second (d, e, f), and third (g, h, i) rows represent methylamine, dimethylamine, and trimethylamine, respectively. The total helium/amine carrier gas flow velocities (u) were maintained between 490 and 560 cm s^{-1} and the flow reactor pressure between 1.4 and 1.6 torr

91
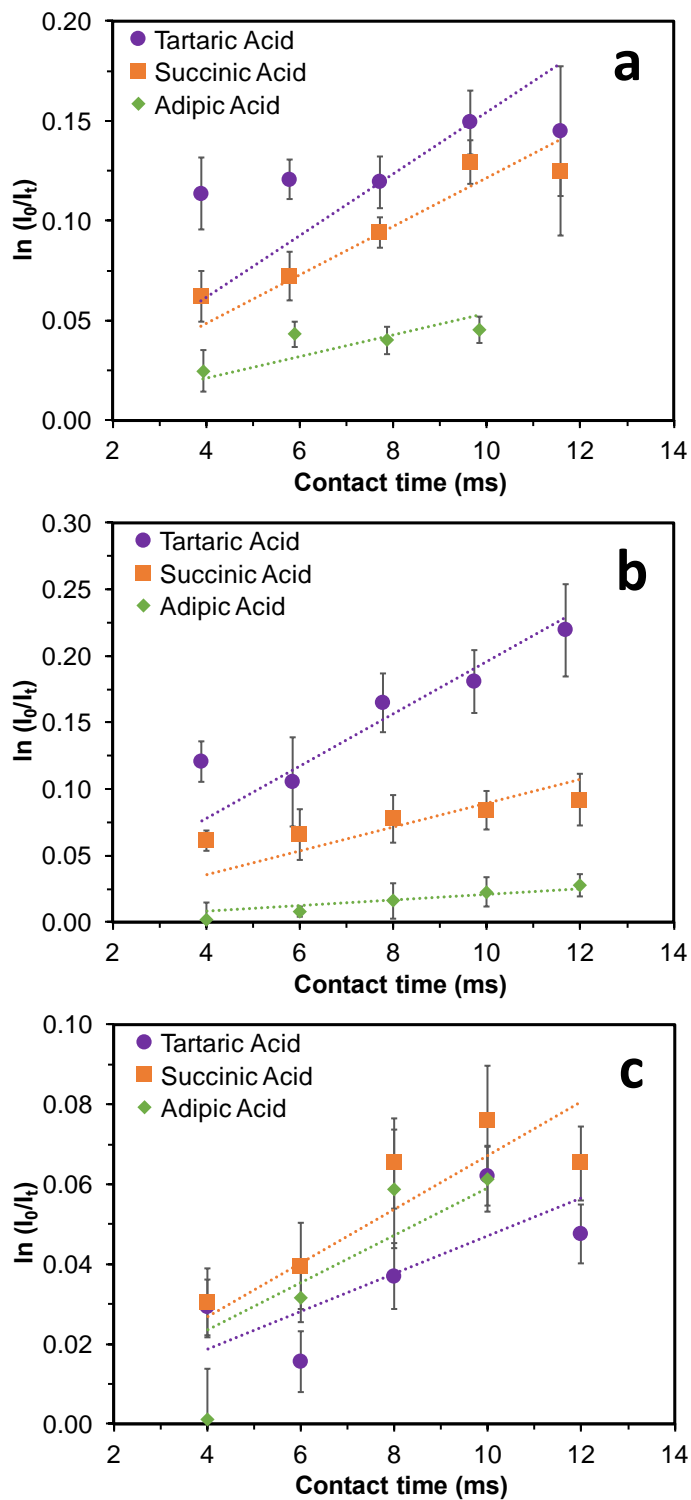
Figure 39: Steady-state amine signal loss as a function of the contact time when exposed to different diacids at 298 K. Panels a, b, and c, correspond to methylamine, dimethylamine, and trimethylamine, respectively.

The reactions studied here are fast acid-base reactions. The initial and steady-state uptakes are summarized in Table 14. At 293 K, the initial uptake coefficients are in the range of 10^{-3} and the steady state in the 10^{-4} range. For MA and DA, the values for the initial and steady-state uptake are largest for TarAc and smallest for AdiAc, indicating again an increasing rate with the O/C ratio. This O/C ratio is due to the multifunctional groups on the diacids relative to the carbon chain length. The increase in hydrophobicity of the diacids has an inverse correlation with the amine uptake coefficient. Although all of the diacids have comparable physical properties at room temperature, they differ in acidity (table 12). The pKa_1 of TarAc, SucAc, and AdiAc are 2.98, 4.2, and 4.40, respectively. Because low pKa_1 corresponds to high acidity, it is not surprising that TarAc is more reactive with a higher uptake coefficient relative to SucAc and AdiAc. By contrast, TarAc and SucAc are C_4, and the additional OH groups in TarAc attract electronic density by induction, making the H from the carboxylic group more acidic, comparable to SucAc. SucAc and AdiAc both are aliphatic straight chains with a two-carbon-atom difference. SucAc is C_4, and AdiAc is C_6; thus, the extra two carbons in AdiAc provide electronic density by induction to the carboxylic groups, making it less acidic and more stable. Another reason could be that the strong hydrophobicity of AdiAc makes the penetration of the amines disrupt the structure of the AdiAc and makes it energetically less favorable compared to TarAc and SucAc. Interestingly, the lowest uptake for TA is TarAc, a fact likely due to a competition between the steric effect of both the acid and the amine. However, the uptake differences between the diacids are rather insignificant due to uncertainties.

In terms of amine dependence, there is an interplay between the basicity strength and the steric effect as well. For SucAc, the steady-state uptake trend was MA > DA > TA, likely describing a dependence on the steric effect of the amines. However, for TarAc the uptake trend was DA > MA > TA, similar to the basicity strength in solution since TarAc also has higher acidity. Interestingly, the AdiAc uptake trend was TA > MA > DA, noting that the uptake values were low and had high uncertainties.

Table 14: Measured initial and steady-state uptake coefficients for amines and diacids

	Methylamine (MA)		Dimethylamine (DA)		Trimethylamine (TA)	
	γ_{ss} ($\times10^{-4}$)	γ_0 ($\times10^{-3}$)	γ_{ss} ($\times10^{-4}$)	γ_0 ($\times10^{-3}$)	γ_{ss} ($\times10^{-4}$)	γ_0 ($\times10^{-3}$)
Tartaric Acid (TarAc)	5.68 ± 1.43	5.99 ± 0.31	8.68 ± 2.71	7.13 ± 0.97	2.39 ± 0.95	4.77 ± 0.33
Succinic Acid (SucAc)	4.44 ± 1.24	4.84 ± 0.50	4.13 ± 1.89	5.28 ± 1.38	3.51 ± 1.42	7.07 ± 0.87
Adipic Acid (AdiAc)	1.96 ± 1.26	3.99 ± 0.77	1.03 ± 1.58	2.75 ± 0.85	3.18 ± 1.90	3.80 ± 1.05

The acidity dependence and the order of magnitude of the initial uptake coefficients are similar to those reported by Liu et al. with citric acid, but much higher than humic acid. The uptake values obtained in this study are similar to those obtained by Qiu et al. for DA and TA on ammonium sulfate in a displacement reaction (not acid-base). However, Fairhurst et al. showed that pKa alone cannot explain acidity behavior. For example, their uptake coefficient with DA was about 0.27, 0.7×10^{-4}, and 0.03 for malonic ($pK_a = 2.83$),

succinic ($pK_a = 4.16$), and glutaric ($pK_a = 4.31$) acids, respectively. Nevertheless, both studies used a Knudsen cell reactor while this study used a flow reactor.

If the interactions between the base and the acid were gas-liquid (instead of gas-solid), the uptake coefficients would be smaller than those observed because more time is required for gaseous species to diffuse into the solution to react with the acidic proton. Moreover, our uptake coefficients for all amines are independent of the mass of the diacid coating onto the sample tube, as shown in Figure 40. Therefore, the available area for reaction of the diacids may not be considerably different from its geometric area; otherwise, the uptake coefficient would increase with a larger coating mass. For a tube coated with 5 mg of diacid (like TarAc) there are $\sim \times 10^{19}$ active sites, which is one order of magnitude higher that all the amine filled in one bulb ($\sim \times 10^{18}$). Therefore, only a fraction of the diacid coating (outer layer) is consumed during the experimental exposures. Additionally, under the time scale of the experimental setup, the uptake coefficients do not decrease as a function of time; therefore, no surface passivation was observed [*Fairhurst et al.*, 2017a]. Also, since all our diacids were even (C_4 and C_6), they form a more stable crystal structure, and when they react with a base, a solid salt is produced; thus, no formation of ionic liquid was observed [*Fairhurst et al.*, 2017b; *Thalladi et al.*, 2000]. Since the reaction kinetics between diacids and amines are comparable to those of sulfates and nitrates, which are very important components to atmospheric aerosols, neutralization of organic acids could serve as an important mechanism for the formation of particulate nitrogen in SOA.
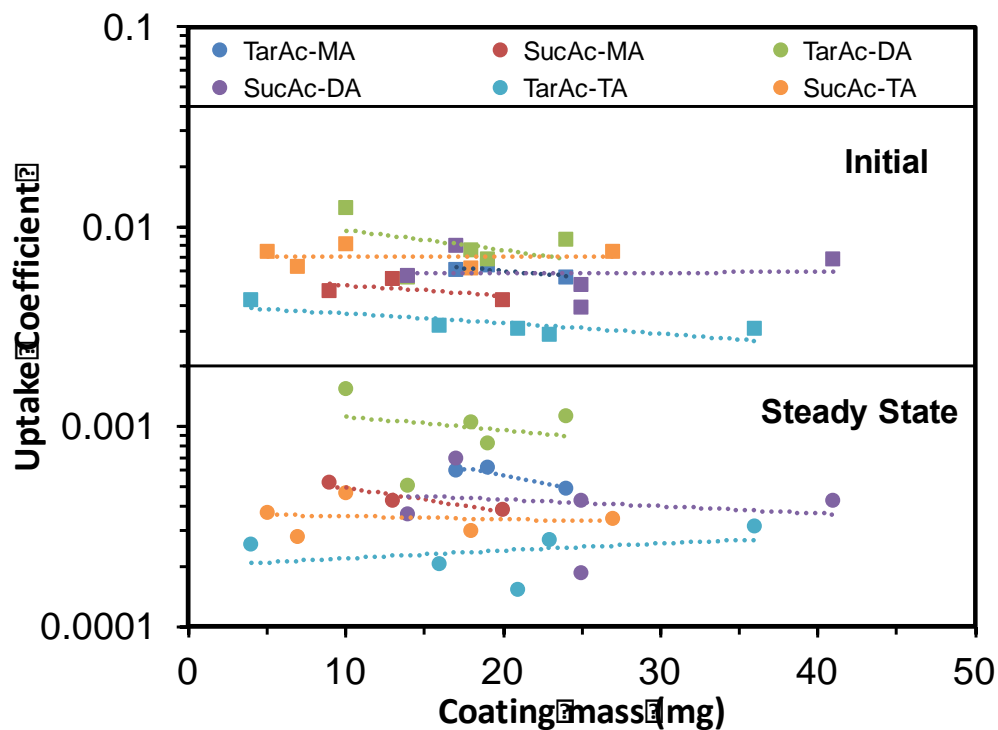
Figure 40: Initial and steady-state uptake coefficient as a function of the diacid coating mass on the tube.

Atmospheric Implications

Aerosols play a critical role in climate, directly by scattering and absorbing solar radiation and indirectly by altering cloud formation, but substantial uncertainties remain about their formation and growth mechanisms [*Zhang*, 2010; *Zhang et al.*, 2015b]. Organic acids are often found in the aerosol phase; therefore, the acid-base neutralization by gaseous amines produces low-volatility aminium salts that could contribute to the growth of aerosols, altering their physical and chemical properties [*Gomez-Hernandez et al.*, 2016; *Lavi et al.*, 2015; *Qiu and Zhang*, 2013]. A laminar fast-flow reactor coupled to an ID-CIMS was used to assess the uptake of gaseous amine on solid-phase diacids. The

heterogeneous uptake of amines on each acid occurred rapidly, resulting in uptake coefficients that denote comparable reactivity to common atmospheric aerosol components. The results demonstrate that the acid-base neutralization, under dry conditions, is governed by the steric effect and the acidity-basicity strength of both the diacids and the amines.

The findings from this work, along with the recent results by Fairhurst et al. and our previous works of uptake of amines on sulfuric acid and ammonium sulfate, suggest that amines contribute to neutralization and particle growth. The amines more efficiently neutralize the acidic aerosols than ammonia by orders of magnitude. However, the neutralization is dominated by ammonia due to it is abundance at ambient conditions, except close to the amine emission sources. Moreover, based on the uptake coefficients of amines with any diacids, MA dominates due to its low steric effect and DA dominates due to its strong basicity; however, under ambient conditions, TA concentration is higher by orders of magnitude.

The data suggest that multiple factors at the molecular level affect the gas-solid interactions and have implications for how atmospheric models treat the uptake. Highly oxidized organic acids are more common in the atmosphere than solid diacid salts. Therefore, further studies of multifunctional acids are needed to assess the steric effect and reactivity behaviors in the reaction kinetics. Accurate kinetic information will contribute to a better understanding of the sinks and evolution of the amines and organic acids leading to SOA formation.

CHAPTER VI

CONCLUSIONS AND FURTURE DIRECTIONS

Atmospheric aerosols profoundly impact human health, visibility, the ecosystem, and the climate. However, there are considerable uncertainties concerning their formation, transformation, and properties. In this doctoral research, a series of laboratory measurements were conducted to investigate various scientific questions, including the relation between the ambient aerosol mass concentration and light extinction, the oxidation of SO_2, the light absorption by organic aerosols, the aerosol reactivity, and the aerosol physiochemical properties. A series of analytical techniques were employed, from field to flow reactor, to understand those aerosol processes.

In chapter II, field measurements are presented during winter 2015 in Beijing to study the chemical and optical properties of aerosols during severe haze events. During the haze development, the contribution of the secondary inorganic components (NO_3^-, SO_4^{2-}, and NH_4^+) increases for both the $PM_{2.5}$ mass concentration and light-extinction. Moreover, BC is the dominant light absorber component, and there is no evidence for brown carbon formation. The anti-correlation between the $PM_{2.5}$ mass concentration and the MLH indicates that the meteorological conditions drive the accumulation process through the polluted period. The light extinction leads to the stabilization of the atmosphere that affects negatively to air quality. Future studies using ambient chamber will be helpful to distinguish the contribution of primary from secondary aerosols in the optical properties at wavelength smaller than 532 nm.

In chapter III, evidence of ambient sulfate concentration is provided, as well as its dependence on RH. The results from the field measurements, in combination with the laboratory chamber experiments, show that SO_2 oxidation by NO_2 into SO_4^{2-} is facilitated by high RH, low temperature, and large concentrations of NO_2 and NH_3, leading to significant secondary particle growth of pre-existing aerosols. The formation of various secondary organic and inorganic constituents in fine aerosols is mutually promoting, and severe haze development involves a transition from photochemical to aqueous phase pathway. The synergetic sulfate formation pathway from this work is likely widespread globally. The increase in emissions of SO_2, NO_x, VOC, and basic species (NH_3 and amines) contribute not only to deteriorated air quality but also to enhanced nitrogen or acid deposition with implications to ecosystems. Future studies to determine the particle phase-state and pH are needed to determine the dominant oxidation pathway in specific regions.

The mechanism for brown carbon formation and optical properties are explored in the chapter IV. BrC particles are formed from bulk reactions between small α-dicarbonyls and amines, and the compositional analyses reveal N-heterocycles as the dominant chromophore. In addition to alter the chemical composition, browning reactions have a pronounced effect on the optical properties. The extinction and absorption cross-sections increase with the particle size, and SSA for methylglyoxal is smaller than that of glyoxal and increases with the methyl substitution of amines. The refractive index retrieved by using the MIE theory can be used as upper and lower limit inputs of BrC in atmospheric models to refine estimates of organic aerosols radiative forcing for specific source regions. Further studies are needed to determine the exact chemical mechanism of the chromophore formation, as well as a radiative transfer model to determine the forcing efficiency.

Moreover, it is uncertain whether the optical properties are due to a mix of all the chromophores or due to supramolecular interactions.

In chapter V, kinetics measurements from organic acids and amines are presented. A laminar fast-flow reactor coupled to an ID-CIMS is used to measure the uptake of the gaseous amine on solid-phase diacids. The results demonstrate that the acid-base neutralization is governed by an interplay between the steric effect and the acidity/basicity strength of both the diacids and the amines. The data suggest that multiple factors at the molecular level affect the gas-solid interactions and have implications for how atmospheric models treat the uptake and particle growth. Future studies of multifunctional organic acids are needed to assess the steric effect and reactivity behaviors in the reaction kinetics. Accurate kinetic information is essential to better understand the sinks and evolution of the amines and organic acids leading to SOA formation.

In summary, this dissertation addresses several scientific questions regarding the aerosol formation and physicochemical properties using several advanced analytical methods. The field measurements lead to chemical apportionment between the mass concentration and light extinction. Moreover, the field data evaluate the SO_4^{2-} formation, the high concentration of NH_4^+, and the relation between low visibility and RH. Chambers experiments are conducted to mimic the polluted conditions in China, and the importance of aqueous reactions is revealed. A detail study is conducted to explore the aerosol aqueous formation (in bulk reactions) and the implications on the aerosol physical and optical properties. The model used for the bulk aqueous reactions is a mixture of α-dicarbonyls and amines; however, due to the amines high volatility and basicity, they are most likely to

react to react in the atmosphere on gas phase with solid organic acids. The last research project evaluates the uptake and heterogeneous kinetics by using a flow reactor.

The experiments presented in this dissertation provide a better understanding on how the atmospheric aerosol processes alter the physical, optical and chemical properties of aerosols and their implications to air quality and climate. Reducing the gap in knowledge on the aerosol processes has significant implications for the development and improvement of climate-related policies and risk assessments worldwide.

.

REFERENCES

Abbatt, J., C. George, M. Melamed, P. Monks, S. Pandis, and Y. Rudich (2014), New Directions: Fundamentals of atmospheric chemistry: Keeping a three-legged stool balanced, *Atmospheric Environment*, *84*, 390-391, doi:https://doi.org/10.1016/j.atmosenv.2013.10.025.

Abbatt, J., A. K. Y. Lee, and J. A. Thornton (2012), Quantifying trace gas uptake to tropospheric aerosol: recent advances and remaining challenges, *Chem. Soc. Rev.*, *41*(19), 6555-6581, doi:10.1039/C2CS35052A.

Abo Riziq, A., C. Erlick, E. Dinar, and Y. Rudich (2007), Optical properties of absorbing and non-absorbing aerosols retrieved by cavity ring down (CRD) spectroscopy, *Atmos. Chem. Phys.*, *7*(6), 1523-1536, doi:10.5194/acp-7-1523-2007.

Andreae, M. O. (2009), A New Look at Aging Aerosols, *Science*, *326*(5959), 1493-1494, doi:10.1126/science.1183158.

Andreae, M. O., and P. J. Crutzen (1997), Atmospheric Aerosols: Biogeochemical Sources and Role in Atmospheric Chemistry, *Science*, *276*(5315), 1052-1058, doi:10.1126/science.276.5315.1052.

Andreae, M. O., and V. Ramanathan (2013), Climate's Dark Forcings, *Science*, *340*(6130), 280-281, doi:10.1126/science.1235731.

Arnott, W. P., H. Moosmüller, P. J. Sheridan, J. A. Ogren, R. Raspet, W. V. Slaton, J. L. Hand, S. M. Kreidenweis, and J. L. Collett (2003), Photoacoustic and filter-based ambient aerosol light absorption measurements: Instrument comparisons and the role of relative humidity, *J. Geophys. Res.*, *108*(D1), AAC 15-11-AAC 15-11, doi:10.1029/2002JD002165.

Ault, A. P., and J. L. Axson (2017), Atmospheric Aerosol Chemistry: Spectroscopic and Microscopic Advances, *Anal. Chem.*, *89*(1), 430-452, doi:10.1021/acs.analchem.6b04670.

Bahadur, R., P. S. Praveen, Y. Xu, and V. Ramanathan (2012), Solar absorption by elemental and brown carbon determined from spectral observations, *Proc. Natl. Acad. Sci.*, *109*(43), 17366-17371, doi:10.1073/pnas.1205910109.

Barsanti, K. C., P. H. McMurry, and J. N. Smith (2009), The potential contribution of organic salts to new particle growth, *Atmos. Chem. Phys.*, *9*(9), 2949-2957, doi:10.5194/acp-9-2949-2009.

Bilde, M., K. Barsanti, M. Booth, C. D. Cappa, N. M. Donahue, E. U. Emanuelsson, G. McFiggans, U. K. Krieger, C. Marcolli, D. Topping, P. Ziemann, M. Barley, S. Clegg, B. Dennis-Smither, M. Hallquist, Å. M. Hallquist, A. Khlystov, M. Kulmala, D. Mogensen, C. J. Percival, F. Pope, J. P. Reid, M. A. V. Ribeiro da Silva, T. Rosenoern, K. Salo, V. P. Soonsin, T. Yli-Juuti, N. L. Prisle, J. Pagels, J. Rarey, A. A. Zardini, and I. Riipinen (2015), Saturation Vapor Pressures and Transition Enthalpies of Low-Volatility Organic Molecules of Atmospheric Relevance: From Dicarboxylic Acids to Complex Mixtures, *Chem. Rev.*, *115*(10), 4115-4156, doi:10.1021/cr5005502.

Bohren, C. F., and D. R. Huffman (2004), Appendix A: Homogeneous Sphere, in *Absorption and Scattering of Light by Small Particles*, edited, pp. 477-482, Wiley-VCH Verlag GmbH, doi:10.1002/9783527618156.app2.

Bond, T. C. (2001), Spectral dependence of visible light absorption by carbonaceous particles emitted from coal combustion, *Geophys. Res. Lett.*, *28*(21), 4075-4078, doi:10.1029/2001GL013652.

Bond, T. C., and R. W. Bergstrom (2006), Light Absorption by Carbonaceous Particles: An Investigative Review, *Aerosol Sci. Technol.*, *40*(1), 27-67, doi:10.1080/02786820500421521.

Bond, T. C., S. J. Doherty, D. W. Fahey, P. M. Forster, T. Berntsen, B. J. DeAngelo, M. G. Flanner, S. Ghan, B. Kärcher, D. Koch, S. Kinne, Y. Kondo, P. K. Quinn, M. C. Sarofim, M. G. Schultz, M. Schulz, C. Venkataraman, H. Zhang, S. Zhang, N. Bellouin, S. K. Guttikunda, P. K. Hopke, M. Z. Jacobson, J. W. Kaiser, Z. Klimont, U. Lohmann, J. P. Schwarz, D. Shindell, T. Storelvmo, S. G. Warren, and C. S. Zender (2013), Bounding the role of black carbon in the climate system: A scientific assessment, *J. Geophys. Res.*, *118*(11), 5380-5552, doi:10.1002/jgrd.50171.

Burkholder, J. B., J. P. D. Abbatt, I. Barnes, J. M. Roberts, M. L. Melamed, M. Ammann, A. K. Bertram, C. D. Cappa, A. G. Carlton, L. J. Carpenter, J. N. Crowley, Y. Dubowski, C. George, D. E. Heard, H. Herrmann, F. N. Keutsch, J. H. Kroll, V. F. McNeill, N. L. Ng, S. A. Nizkorodov, J. J. Orlando, C. J. Percival, B. Picquet-Varrault, Y. Rudich, P. W. Seakins, J. D. Surratt, H. Tanimoto, J. A. Thornton, Z. Tong, G. S. Tyndall, A. Wahner, C. J. Weschler, K. R. Wilson, and P. J. Ziemann (2017), The Essential Role for Laboratory Studies in Atmospheric Chemistry, *Environ. Sci. Technol.*, *51*(5), 2519-2528, doi:10.1021/acs.est.6b04947.

Burnett, R. T., C. A. Pope, M. Ezzati, C. Olives, S. S. Lim, S. Mehta, H. H. Shin, G. Singh, B. Hubbell, M. Brauer, H. R. Anderson, K. R. Smith, J. R. Balmes, N. G. Bruce, H. Kan, F. Laden, A. Prüss-Ustün, M. C. Turner, S. M. Gapstur, W. R. Diver, and A. Cohen (2014), An Integrated Risk Function for Estimating the Global Burden of Disease Attributable to Ambient Fine Particulate Matter Exposure, *Environmental Health Perspectives*, *122*(4), 397-403, doi:10.1289/ehp.1307049.

Cao, J. J., Q. Y. Wang, J. C. Chow, J. G. Watson, X. X. Tie, Z. X. Shen, P. Wang, and Z. S. An (2012), Impacts of aerosol compositions on visibility impairment in Xi'an, China, *Atmos. Environ.*, *59*, 559-566, doi:10.1016/j.atmosenv.2012.05.036.

Cappa, C. D., T. B. Onasch, P. Massoli, D. R. Worsnop, T. S. Bates, E. S. Cross, P. Davidovits, J. Hakala, K. L. Hayden, B. T. Jobson, K. R. Kolesar, D. A. Lack, B. M. Lerner, S.-M. Li, D. Mellon, I. Nuaaman, J. S. Olfert, T. Petäjä, P. K. Quinn, C. Song, R. Subramanian, E. J. Williams, and R. A. Zaveri (2012), Radiative Absorption Enhancements Due to the Mixing State of Atmospheric Black Carbon, *Science*, *337*(6098), 1078-1081, doi:10.1126/science.1223447.

Chan, C. K., and X. Yao (2008), Air pollution in mega cities in China, *Atmos. Environ.*, *42*(1), 1-42, doi:https://doi.org/10.1016/j.atmosenv.2007.09.003.

Chang, J. S., R. A. Brost, I. S. A. Isaksen, S. Madronich, P. Middleton, W. R. Stockwell, and C. J. Walcek (1987), A three-dimensional Eulerian acid deposition model: Physical concepts and formulation, *J. Geophys. Res.*, *92*(D12), 14681-14700, doi:10.1029/JD092iD12p14681.

Chen, J., S. Qiu, J. Shang, O. M. F. Wilfrid, X. Liu, H. Tian, and J. Boman (2014), Impact of Relative Humidity and Water Soluble Constituents of PM2.5 on Visibility Impairment in Beijing, China, *Aerosol and Air Quality Research*, *14*(1), 260-268, doi:10.4209/aaqr.2012.12.0360.

Cheng, Y., G. Zheng, C. Wei, Q. Mu, B. Zheng, Z. Wang, M. Gao, Q. Zhang, K. He, G. Carmichael, U. Pöschl, and H. Su (2016), Reactive nitrogen chemistry in aerosol water as a source of sulfate during haze events in China, *Sci. Adv.*, *2*(12), doi:10.1126/sciadv.1601530.

Chylek, P., and J. Wong (1995), Effect of absorbing aerosols on global radiation budget, *Geophys. Res. Lett.*, *22*(8), 929-931, doi:10.1029/95GL00800.

Clifton, C. L., N. Altstein, and R. E. Huie (1988), Rate constant for the reaction of nitrogen dioxide with sulfur(IV) over the pH range 5.3-13, *Environ. Sci. Technol.*, *22*(5), 586-589, doi:10.1021/es00170a018.

Cornell, S. E., T. D. Jickells, J. N. Cape, A. P. Rowland, and R. A. Duce (2003), Organic nitrogen deposition on land and coastal environments: a review of methods and data, *Atmos. Environ.*, *37*(16), 2173-2191, doi:https://doi.org/10.1016/S1352-2310(03)00133-X.

Corr, C. A., N. Krotkov, S. Madronich, J. R. Slusser, B. Holben, W. Gao, J. Flynn, B. Lefer, and S. M. Kreidenweis (2009), Retrieval of aerosol single scattering albedo at ultraviolet wavelengths at the T1 site during MILAGRO, *Atmos. Chem. Phys.*, *9*(15), 5813-5827, doi:10.5194/acp-9-5813-2009.

Correia, A. W., C. A. I. Pope, D. W. Dockery, Y. Wang, M. Ezzati, and F. Dominici (2013), Effect of Air Pollution Control on Life Expectancy in the United States: An Analysis of 545 U.S. Counties for the Period from 2000 to 2007, *Epidemiology*, *24*(1), 23-31, doi:10.1097/EDE.0b013e3182770237.

Davidovits, P., C. E. Kolb, L. R. Williams, J. T. Jayne, and D. R. Worsnop (2006), Mass Accommodation and Chemical Reactions at Gas−Liquid Interfaces, *Chem. Rev.*, *106*(4), 1323-1354, doi:10.1021/cr040366k.

De Haan, D. O., A. L. Corrigan, K. W. Smith, D. R. Stroik, J. J. Turley, F. E. Lee, M. A. Tolbert, J. L. Jimenez, K. E. Cordova, and G. R. Ferrell (2009a), Secondary Organic Aerosol-Forming Reactions of Glyoxal with Amino Acids, *Environ. Sci. Technol.*, *43*(8), 2818-2824, doi:10.1021/es803534f.

De Haan, D. O., L. N. Hawkins, J. A. Kononenko, J. J. Turley, A. L. Corrigan, M. A. Tolbert, and J. L. Jimenez (2011), Formation of Nitrogen-Containing Oligomers by Methylglyoxal and Amines in Simulated Evaporating Cloud Droplets, *Environ. Sci. Technol.*, *45*(3), 984-991, doi:10.1021/es102933x.

De Haan, D. O., L. N. Hawkins, H. G. Welsh, R. Pednekar, J. R. Casar, E. A. Pennington, A. de Loera, N. G. Jimenez, M. A. Symons, M. Zauscher, A. Pajunoja, L. Caponi, M. Cazaunau, P. Formenti, A. Gratien, E. Pangui, and J.-F. Doussin (2017), Brown Carbon Production in Ammonium- or Amine-Containing Aerosol Particles by Reactive Uptake of Methylglyoxal and Photolytic Cloud Cycling, *Environ. Sci. Technol.*, *51*(13), 7458-7466, doi:10.1021/acs.est.7b00159.

De Haan, D. O., M. A. Tolbert, and J. L. Jimenez (2009b), Atmospheric condensed-phase reactions of glyoxal with methylamine, *Geophys. Res. Lett.*, *36*(11), n/a-n/a, doi:10.1029/2009GL037441.

DeCarlo, P. F., J. R. Kimmel, A. Trimborn, M. J. Northway, J. T. Jayne, A. C. Aiken, M. Gonin, K. Fuhrer, T. Horvath, K. S. Docherty, D. R. Worsnop, and J. L. Jimenez

(2006), Field-Deployable, High-Resolution, Time-of-Flight Aerosol Mass Spectrometer, *Anal. Chem.*, *78*(24), 8281-8289, doi:10.1021/ac061249n.

Dinar, E., A. Abo Riziq, C. Spindler, C. Erlick, G. Kiss, and Y. Rudich (2008), The complex refractive index of atmospheric and model humic-like substances (HULIS) retrieved by a cavity ring down aerosol spectrometer (CRD-AS), *Faraday Discuss.*, *137*(0), 279-295, doi:10.1039/B703111D.

Docherty, K. S., A. C. Aiken, J. A. Huffman, I. M. Ulbrich, P. F. DeCarlo, D. Sueper, D. R. Worsnop, D. C. Snyder, R. E. Peltier, R. J. Weber, B. D. Grover, D. J. Eatough, B. J. Williams, A. H. Goldstein, P. J. Ziemann, and J. L. Jimenez (2011), The 2005 Study of Organic Aerosols at Riverside (SOAR-1): instrumental intercomparisons and fine particle composition, *Atmos. Chem. Phys.*, *11*(23), 12387-12420, doi:10.5194/acp-11-12387-2011.

Drakaki, E., C. Dessinioti, and C. V. Antoniou (2014), Air pollution and the skin, *Frontiers in Environmental Science*, *2*(11), doi:10.3389/fenvs.2014.00011.

Ervens, B., B. J. Turpin, and R. J. Weber (2011), Secondary organic aerosol formation in cloud droplets and aqueous particles (aqSOA): a review of laboratory, field and model studies, *Atmos. Chem. Phys.*, *11*(21), 11069-11102, doi:10.5194/acp-11-11069-2011.

Fairhurst, M. C., M. J. Ezell, and B. J. Finlayson-Pitts (2017a), Knudsen cell studies of the uptake of gaseous ammonia and amines onto C3-C7 solid dicarboxylic acids, *Phys. Chem. Chem. Phys.*, *19*(38), 26296-26309, doi:10.1039/C7CP05252A.

Fairhurst, M. C., M. J. Ezell, C. Kidd, P. S. J. Lakey, M. Shiraiwa, and B. J. Finlayson-Pitts (2017b), Kinetics, mechanisms and ionic liquids in the uptake of n-butylamine onto low molecular weight dicarboxylic acids, *Phys. Chem. Chem. Phys.*, *19*(6), 4827-4839, doi:10.1039/C6CP08663B.

Fan, J., D. Rosenfeld, Y. Zhang, S. E. Giangrande, Z. Li, L. A. T. Machado, S. T. Martin, Y. Yang, J. Wang, P. Artaxo, H. M. J. Barbosa, R. C. Braga, J. M. Comstock, Z. Feng, W. Gao, H. B. Gomes, F. Mei, C. Pöhlker, M. L. Pöhlker, U. Pöschl, and R. A. F. de Souza (2018), Substantial convection and precipitation enhancements by ultrafine aerosol particles, *Science*, *359*(6374), 411-418, doi:10.1126/science.aan8461.

Fan, J., R. Zhang, G. Li, and W.-K. Tao (2007), Effects of aerosols and relative humidity on cumulus clouds, *J. Geophys. Res.*, *112*(D14), n/a-n/a, doi:10.1029/2006JD008136.

Fan, J., R. Zhang, W.-K. Tao, and K. I. Mohr (2008), Effects of aerosol optical properties on deep convective clouds and radiative forcing, *J. Geophys. Res.*, *113*(D8), n/a-n/a, doi:10.1029/2007JD009257.

Fang, M., C. K. Chan, and X. Yao (2009), Managing air quality in a rapidly developing nation: China, *Atmos. Environ.*, *43*(1), 79-86, doi:https://doi.org/10.1016/j.atmosenv.2008.09.064.

Feng, Y., V. Ramanathan, and V. R. Kotamarthi (2013), Brown carbon: a significant atmospheric absorber of solar radiation?, *Atmos. Chem. Phys.*, *13*(17), 8607-8621, doi:10.5194/acp-13-8607-2013.

Fenger, J. (2009), Air pollution in the last 50 years – From local to global, *Atmos. Environ.*, *43*(1), 13-22, doi:https://doi.org/10.1016/j.atmosenv.2008.09.061.

Finlayson-Pitts, B. J., and J. N. Pitts Jr (2000), CHAPTER 1 - Overview of the Chemistry of Polluted and Remote Atmospheres, in *Chemistry of the Upper and Lower Atmosphere*, edited, pp. 1-14, Academic Press, San Diego, doi:https://doi.org/10.1016/B978-012257060-5/50003-4.

Flores, J. M., R. A. Washenfelder, G. Adler, H. J. Lee, L. Segev, J. Laskin, A. Laskin, S. A. Nizkorodov, S. S. Brown, and Y. Rudich (2014), Complex refractive indices in the near-ultraviolet spectral region of biogenic secondary organic aerosol aged with ammonia, *Phys. Chem. Chem. Phys.*, *16*(22), 10629-10642, doi:10.1039/C4CP01009D.

Flowers, B. A., M. K. Dubey, C. Mazzoleni, E. A. Stone, J. J. Schauer, S. W. Kim, and S. C. Yoon (2010), Optical-chemical-microphysical relationships and closure studies for mixed carbonaceous aerosols observed at Jeju Island; 3-laser photoacoustic spectrometer, particle sizing, and filter analysis, *Atmos. Chem. Phys.*, *10*(21), 10387-10398.

Fortner, E. C., J. Zhao, and R. Zhang (2004), Development of Ion Drift-Chemical Ionization Mass Spectrometry, *Anal. Chem.*, *76*(18), 5436-5440, doi:10.1021/ac0493222.

Freedman, M. A., C. A. Hasenkopf, M. R. Beaver, and M. A. Tolbert (2009), Optical Properties of Internally Mixed Aerosol Particles Composed of Dicarboxylic Acids and Ammonium Sulfate, *J. Phys. Chem. A*, *113*(48), 13584-13592, doi:10.1021/jp906240y.

Fuller, E. N., P. D. Schettler, and J. C. Giddings (1966), NEW METHOD FOR PREDICTION OF BINARY GAS-PHASE DIFFUSION COEFFICIENTS, *Industrial & Engineering Chemistry*, *58*(5), 18-27, doi:10.1021/ie50677a007.

Galloway, M. M., P. S. Chhabra, A. W. H. Chan, J. D. Surratt, R. C. Flagan, J. H. Seinfeld, and F. N. Keutsch (2009), Glyoxal uptake on ammonium sulphate seed aerosol: reaction products and reversibility of uptake under dark and irradiated conditions, *Atmos. Chem. Phys.*, *9*(10), 3331-3345, doi:10.5194/acp-9-3331-2009.

Gauderman , W. J., E. Avol , F. Gilliland , H. Vora , D. Thomas , K. Berhane , R. McConnell , N. Kuenzli , F. Lurmann , E. Rappaport , H. Margolis , D. Bates , and J. Peters (2004), The Effect of Air Pollution on Lung Development from 10 to 18 Years of Age, *New England Journal of Medicine*, *351*(11), 1057-1067, doi:10.1056/NEJMoa040610.

Ge, X., A. S. Wexler, and S. L. Clegg (2011), Atmospheric amines – Part I. A review, *Atmos. Environ.*, *45*(3), 524-546, doi:https://doi.org/10.1016/j.atmosenv.2010.10.012.

George, I. J., and J. P. D. Abbatt (2010), Heterogeneous oxidation of atmospheric aerosol particles by gas-phase radicals, *Nature Chemistry*, *2*, 713, doi:10.1038/nchem.806.

Gershenzon, Y. M., V. M. Grigorieva, A. V. Ivanov, and R. G. Remorov (1995), O3 and OH Sensitivity to heterogeneous sinks of HO and CH3O2 on aerosol particles, *Faraday Discuss.*, *100*(0), 83-100, doi:10.1039/FD9950000083.

Gomez, M. E., Y. Lin, S. Guo, and R. Zhang (2015), Heterogeneous Chemistry of Glyoxal on Acidic Solutions. An Oligomerization Pathway for Secondary Organic Aerosol Formation, *J. Phys. Chem. A*, *119*(19), 4457-4463, doi:10.1021/jp509916r.

Gomez-Hernandez, M., M. McKeown, J. Secrest, W. Marrero-Ortiz, A. Lavi, Y. Rudich, D. R. Collins, and R. Zhang (2016), Hygroscopic Characteristics of Alkylaminium Carboxylate Aerosols, *Environ. Sci. Technol.*, *50*(5), 2292-2300, doi:10.1021/acs.est.5b04691.

Guo, H., R. J. Weber, and A. Nenes (2017), High levels of ammonia do not raise fine particle pH sufficiently to yield nitrogen oxide-dominated sulfate production, *Sci. Rep.*, *7*(1), 12109, doi:10.1038/s41598-017-11704-0.

Guo, S., M. Hu, Q. Guo, X. Zhang, J. Schauer, and R. Zhang (2013), Quantitative evaluation of emission controls on primary and secondary organic aerosol sources during Beijing 2008 Olympics, *Atmos. Chem. Phys.*, *13*(16), 8303-8314.

Guo, S., M. Hu, M. L. Zamora, J. Peng, D. Shang, J. Zheng, Z. Du, Z. Wu, M. Shao, L. Zeng, M. J. Molina, and R. Zhang (2014), Elucidating severe urban haze formation in China, *Proc. Natl. Acad. Sci.*, *111*(49), 17373-17378, doi:10.1073/pnas.1419604111.

Haines, A., M. Amann, N. Borgford-Parnell, S. Leonard, J. Kuylenstierna, and D. Shindell (2017), Short-lived climate pollutant mitigation and the Sustainable Development Goals, *Nature Climate Change*, *7*(12), 863-869, doi:10.1038/s41558-017-0012-x.

Hallquist, M., J. C. Wenger, U. Baltensperger, Y. Rudich, D. Simpson, M. Claeys, J. Dommen, N. M. Donahue, C. George, A. H. Goldstein, J. F. Hamilton, H. Herrmann, T. Hoffmann, Y. Iinuma, M. Jang, M. E. Jenkin, J. L. Jimenez, A. Kiendler-Scharr, W. Maenhaut, G. McFiggans, T. F. Mentel, A. Monod, A. S. H. Prévôt, J. H. Seinfeld, J. D. Surratt, R. Szmigielski, and J. Wildt (2009), The formation, properties and impact of secondary organic aerosol: current and emerging issues, *Atmos. Chem. Phys.*, *9*(14), 5155-5236, doi:10.5194/acp-9-5155-2009.

Hanson, D. R., J. B. Burkholder, C. J. Howard, and A. Ravishankara (1992), Measurement of hydroxyl and hydroperoxy radical uptake coefficients on water and sulfuric acid surfaces, *J. Phys. Chem.*, *96*(12), 4979-4985.

Heald, C. L., D. J. Jacob, R. J. Park, L. M. Russell, B. J. Huebert, J. H. Seinfeld, H. Liao, and R. J. Weber (2005), A large organic aerosol source in the free troposphere missing from current models, *Geophys. Res. Lett.*, *32*(18), n/a-n/a, doi:10.1029/2005GL023831.

Heard, D. E., and A. Saiz-Lopez (2012), Atmospheric chemistry, *Chem. Soc. Rev.*, *41*(19), 6229-6230, doi:10.1039/C2CS90076A.

Hennigan, C. J., J. Izumi, A. P. Sullivan, R. J. Weber, and A. Nenes (2015), A critical evaluation of proxy methods used to estimate the acidity of atmospheric particles, *Atmos. Chem. Phys.*, *15*(5), 2775-2790, doi:10.5194/acp-15-2775-2015.

Herrmann, H., T. Schaefer, A. Tilgner, S. A. Styler, C. Weller, M. Teich, and T. Otto (2015), Tropospheric Aqueous-Phase Chemistry: Kinetics, Mechanisms, and Its Coupling to a Changing Gas Phase, *Chem. Rev.*, *115*(10), 4259-4334, doi:10.1021/cr500447k.

Hu, W., M. Hu, W. Hu, J. L. Jimenez, B. Yuan, W. Chen, M. Wang, Y. Wu, C. Chen, Z. Wang, J. Peng, L. Zeng, and M. Shao (2016), Chemical composition, sources, and aging process of submicron aerosols in Beijing: Contrast between summer and winter, *J. Geophys. Res.*, *121*(4), 1955-1977, doi:10.1002/2015JD024020.

Huang, R.-J., Y. Zhang, C. Bozzetti, K.-F. Ho, J.-J. Cao, Y. Han, K. R. Daellenbach, J. G. Slowik, S. M. Platt, F. Canonaco, P. Zotter, R. Wolf, S. M. Pieber, E. A. Bruns, M. Crippa, G. Ciarelli, A. Piazzalunga, M. Schwikowski, G. Abbaszade, J. Schnelle-Kreis, R. Zimmermann, Z. An, S. Szidat, U. Baltensperger, I. E. Haddad, and A. S. H. Prévôt (2014), High secondary aerosol contribution to particulate pollution during haze events in China, *Nature*, *514*, 218, doi:10.1038/nature13774 https://www.nature.com/articles/nature13774#supplementary-information.

Hung, H.-M., and M. R. Hoffmann (2015), Oxidation of Gas-Phase SO2 on the Surfaces of Acidic Microdroplets: Implications for Sulfate and Sulfate Radical Anion Formation in the Atmospheric Liquid Phase, *Environ. Sci. Technol.*, *49*(23), 13768-13776, doi:10.1021/acs.est.5b01658.

IPCC (2013), *Climate Change 2013: The Physical Science Basis. Contribution of Working Group I to the Fifth Assessment Report of the Intergovernmental Panel on Climate Change*, 1535 pp., Cambridge University Press, Cambridge, United Kingdom and New York, NY, USA, doi:10.1017/CBO9781107415324.

Jacob, D. J., and D. A. Winner (2009), Effect of climate change on air quality, *Atmos. Environ.*, *43*(1), 51-63, doi:https://doi.org/10.1016/j.atmosenv.2008.09.051.

Jang, M., N. M. Czoschke, S. Lee, and R. M. Kamens (2002), Heterogeneous Atmospheric Aerosol Production by Acid-Catalyzed Particle-Phase Reactions, *Science*, *298*(5594), 814-817, doi:10.1126/science.1075798.

Jimenez, J. L., M. R. Canagaratna, N. M. Donahue, A. S. H. Prevot, Q. Zhang, J. H. Kroll, P. F. DeCarlo, J. D. Allan, H. Coe, N. L. Ng, A. C. Aiken, K. S. Docherty, I. M. Ulbrich, A. P. Grieshop, A. L. Robinson, J. Duplissy, J. D. Smith, K. R. Wilson, V. A. Lanz, C. Hueglin, Y. L. Sun, J. Tian, A. Laaksonen, T. Raatikainen, J. Rautiainen, P. Vaattovaara, M. Ehn, M. Kulmala, J. M. Tomlinson, D. R. Collins, M. J. Cubison, J. Dunlea, J. A. Huffman, T. B. Onasch, M. R. Alfarra, P. I. Williams, K. Bower, Y. Kondo, J. Schneider, F. Drewnick, S. Borrmann, S. Weimer, K. Demerjian, D. Salcedo, L. Cottrell, R. Griffin, A. Takami, T. Miyoshi, S. Hatakeyama, A. Shimono, J. Y. Sun, Y. M. Zhang, K. Dzepina, J. R. Kimmel, D. Sueper, J. T. Jayne, S. C. Herndon, A. M. Trimborn, L. R. Williams, E. C. Wood, A. M. Middlebrook, C. E. Kolb, U. Baltensperger, and D. R. Worsnop (2009), Evolution of Organic Aerosols in the Atmosphere, *Science*, *326*(5959), 1525-1529, doi:10.1126/science.1180353.

Jung, J., H. Lee, Y. J. Kim, X. Liu, Y. Zhang, M. Hu, and N. Sugimoto (2009), Optical properties of atmospheric aerosols obtained by in situ and remote measurements during 2006 Campaign of Air Quality Research in Beijing (CAREBeijing-2006), *J. Geophys. Res.*, *114*(D2), n/a-n/a, doi:10.1029/2008JD010337.

Kampf, C. J., A. Filippi, C. Zuth, T. Hoffmann, and T. Opatz (2016), Secondary brown carbon formation via the dicarbonyl imine pathway: nitrogen heterocycle formation and synergistic effects, *Phys. Chem. Chem. Phys.*, *18*(27), 18353-18364, doi:10.1039/C6CP03029G.

Kampf, C. J., R. Jakob, and T. Hoffmann (2012), Identification and characterization of aging products in the glyoxal/ammonium sulfate system– implications for light-absorbing material in atmospheric aerosols, *Atmos. Chem. Phys.*, *12*(14), 6323-6333.

Kanakidou, M., J. H. Seinfeld, S. N. Pandis, I. Barnes, F. J. Dentener, M. C. Facchini, R. Van Dingenen, B. Ervens, A. Nenes, C. J. Nielsen, E. Swietlicki, J. P. Putaud, Y. Balkanski, S. Fuzzi, J. Horth, G. K. Moortgat, R. Winterhalter, C. E. L. Myhre, K. Tsigaridis, E. Vignati, E. G. Stephanou, and J. Wilson (2005), Organic aerosol and global climate modelling: a review, *Atmos. Chem. Phys.*, *5*, 1053-1123, doi:10.5194/acp-5-1053-2005.

Kawamura, K., H. Kasukabe, and L. A. Barrie (1996), Source and reaction pathways of dicarboxylic acids, ketoacids and dicarbonyls in arctic aerosols: One year of observations, *Atmos. Environ.*, *30*(10), 1709-1722, doi:https://doi.org/10.1016/1352-2310(95)00395-9.

Khalizov, A. F., H. Xue, L. Wang, J. Zheng, and R. Zhang (2009a), Enhanced Light Absorption and Scattering by Carbon Soot Aerosol Internally Mixed with Sulfuric Acid, *J. Phys. Chem. A*, *113*(6), 1066-1074, doi:10.1021/jp807531n.

Khalizov, A. F., R. Zhang, D. Zhang, H. Xue, J. Pagels, and P. H. McMurry (2009b), Formation of highly hygroscopic soot aerosols upon internal mixing with sulfuric acid vapor, *J. Geophys. Res.*, *114*(D5), n/a-n/a, doi:10.1029/2008JD010595.

Kirchstetter, T. W., T. Novakov, and P. V. Hobbs (2004), Evidence that the spectral dependence of light absorption by aerosols is affected by organic carbon, *J. Geophys. Res.*, *109*(D21), n/a-n/a, doi:10.1029/2004JD004999.

Koschmieder, H. (1924), Theorie der horizontalen Sichtweite, *Beitrage zur Physik der freien Atmosphare*, 33-53.

Kroll, J. H., N. M. Donahue, J. L. Jimenez, S. H. Kessler, M. R. Canagaratna, K. R. Wilson, K. E. Altieri, L. R. Mazzoleni, A. S. Wozniak, H. Bluhm, E. R. Mysak, J. D. Smith, C. E. Kolb, and D. R. Worsnop (2011), Carbon oxidation state as a metric for describing the chemistry of atmospheric organic aerosol, *Nature Chemistry*, *3*, 133, doi:10.1038/nchem.948 https://www.nature.com/articles/nchem.948#supplementary-information.

Kua, J., H. E. Krizner, and D. O. De Haan (2011), Thermodynamics and Kinetics of Imidazole Formation from Glyoxal, Methylamine, and Formaldehyde: A Computational Study, *J. Phys. Chem. A*, *115*(9), 1667-1675, doi:10.1021/jp111527x.

Kurtén, T., V. Loukonen, H. Vehkamäki, and M. Kulmala (2008), Amines are likely to enhance neutral and ion-induced sulfuric acid-water nucleation in the atmosphere more effectively than ammonia, *Atmos. Chem. Phys.*, *8*(14), 4095-4103, doi:10.5194/acp-8-4095-2008.

Kuwata, M., and S. T. Martin (2012), Phase of atmospheric secondary organic material affects its reactivity, *Proc. Natl. Acad. Sci.*, *109*(43), 17354-17359, doi:10.1073/pnas.1209071109.

Lack, D. A., J. M. Langridge, R. Bahreini, C. D. Cappa, A. M. Middlebrook, and J. P. Schwarz (2012), Brown carbon and internal mixing in biomass burning particles, *Proc. Natl. Acad. Sci.*, *109*(37), 14802-14807, doi:10.1073/pnas.1206575109.

Lambe, A. T., C. D. Cappa, P. Massoli, T. B. Onasch, S. D. Forestieri, A. T. Martin, M. J. Cummings, D. R. Croasdale, W. H. Brune, D. R. Worsnop, and P. Davidovits (2013), Relationship between Oxidation Level and Optical Properties of Secondary Organic Aerosol, *Environ. Sci. Technol.*, *47*(12), 6349-6357, doi:10.1021/es401043j.

Laskin, A., J. Laskin, and S. A. Nizkorodov (2015), Chemistry of Atmospheric Brown Carbon, *Chem. Rev.*, *115*(10), 4335-4382, doi:10.1021/cr5006167.

Laskin, J., A. Laskin, and S. A. Nizkorodov (2018), Mass Spectrometry Analysis in Atmospheric Chemistry, *Anal. Chem.*, *90*(1), 166-189, doi:10.1021/acs.analchem.7b04249.

Laskin, J., A. Laskin, S. A. Nizkorodov, P. Roach, P. Eckert, M. K. Gilles, B. Wang, H. J. Lee, and Q. Hu (2014), Molecular Selectivity of Brown Carbon Chromophores, *Environ. Sci. Technol.*, *48*(20), 12047-12055, doi:10.1021/es503432r.

Lavi, A., E. Segre, M. Gomez-Hernandez, R. Zhang, and Y. Rudich (2015), Volatility of Atmospherically Relevant Alkylaminium Carboxylate Salts, *J. Phys. Chem. A*, *119*(19), 4336-4346, doi:10.1021/jp507320v.

Lee, K. H., Z. Li, M. S. Wong, J. Xin, Y. Wang, W.-M. Hao, and F. Zhao (2007), Aerosol single scattering albedo estimated across China from a combination of ground and satellite measurements, *J. Geophys. Res.*, *112*(D22), n/a-n/a, doi:10.1029/2007JD009077.

Lee, Y., and S. Schwartz (1983), Kinetics of oxidation of aqueous sulfur IV by nitrogen dioxide, in *Precipitation Scavenging, Dry Deposition, and Resuspension*, edited.

Levy, M., R. Zhang, J. Zheng, A. L. Zhang, W. Xu, M. Gomez-Hernandez, Y. Wang, and E. Olaguer (2014), Measurements of nitrous acid (HONO) using ion drift-chemical ionization mass spectrometry during the 2009 SHARP field campaign, *Atmos. Environ.*, *94*, 231-240, doi:https://doi.org/10.1016/j.atmosenv.2014.05.024.

Lim, Y. B., Y. Tan, M. J. Perri, S. P. Seitzinger, and B. J. Turpin (2010), Aqueous chemistry and its role in secondary organic aerosol (SOA) formation, *Atmos. Chem. Phys.*, *10*(21), 10521-10539, doi:10.5194/acp-10-10521-2010.

Limbeck, A., Y. Kraxner, and H. Puxbaum (2005), Gas to particle distribution of low molecular weight dicarboxylic acids at two different sites in central Europe (Austria), *Journal of Aerosol Science*, *36*(8), 991-1005, doi:https://doi.org/10.1016/j.jaerosci.2004.11.013.

Lin, J., D. Pan, S. J. Davis, Q. Zhang, K. He, C. Wang, D. G. Streets, D. J. Wuebbles, and D. Guan (2014), China's international trade and air pollution in the United States, *Proc. Natl. Acad. Sci.*, *111*(5), 1736-1741, doi:10.1073/pnas.1312860111.

Lin, P., J. Laskin, S. A. Nizkorodov, and A. Laskin (2015), Revealing Brown Carbon Chromophores Produced in Reactions of Methylglyoxal with Ammonium Sulfate, *Environ. Sci. Technol.*, *49*(24), 14257-14266, doi:10.1021/acs.est.5b03608.

Liu, J., E. Scheuer, J. Dibb, L. D. Ziemba, K. L. Thornhill, B. E. Anderson, A. Wisthaler, T. Mikoviny, J. J. Devi, M. Bergin, and R. J. Weber (2014), Brown carbon in the continental troposphere, *Geophys. Res. Lett.*, *41*(6), 2191-2195, doi:10.1002/2013GL058976.

Liu, M., Y. Song, T. Zhou, Z. Xu, C. Yan, M. Zheng, Z. Wu, M. Hu, Y. Wu, and T. Zhu (2017), Fine particle pH during severe haze episodes in northern China, *Geophys. Res. Lett.*, *44*(10), 5213-5221, doi:10.1002/2017GL073210.

Liu, X., Y. Zhang, W. Han, A. Tang, J. Shen, Z. Cui, P. Vitousek, J. W. Erisman, K. Goulding, P. Christie, A. Fangmeier, and F. Zhang (2013), Enhanced nitrogen deposition over China, *Nature*, *494*, 459, doi:10.1038/nature11917 https://www.nature.com/articles/nature11917#supplementary-information.

Liu, Y., Q. Ma, and H. He (2012), Heterogeneous Uptake of Amines by Citric Acid and Humic Acid, *Environ. Sci. Technol.*, *46*(20), 11112-11118, doi:10.1021/es302414v.

Loeffler, K. W., C. A. Koehler, N. M. Paul, and D. O. De Haan (2006), Oligomer Formation in Evaporating Aqueous Glyoxal and Methyl Glyoxal Solutions, *Environ. Sci. Technol.*, *40*(20), 6318-6323, doi:10.1021/es060810w.

Ma, N., C. S. Zhao, T. Muller, Y. F. Cheng, P. F. Liu, Z. Z. Deng, W. Y. Xu, L. Ran, B. Nekat, D. van Pinxteren, T. Gnauk, K. Mueller, H. Herrmann, P. Yan, X. J. Zhou, and A. Wiedensohler (2012), A new method to determine the mixing state of light absorbing carbonaceous using the measured aerosol optical properties and number size distributions, *Atmos. Chem. Phys.*, *12*(5), 2381-2397, doi:10.5194/acp-12-2381-2012.

Malm, W. C., and J. L. Hand (2007), An examination of the physical and optical properties of aerosols collected in the IMPROVE program, *Atmos. Environ.*, *41*(16), 3407-3427, doi:https://doi.org/10.1016/j.atmosenv.2006.12.012.

McNeill, V. F. (2015), Aqueous Organic Chemistry in the Atmosphere: Sources and Chemical Processing of Organic Aerosols, *Environ. Sci. Technol.*, *49*(3), 1237-1244, doi:10.1021/es5043707.

McNeill, V. F. (2017), Atmospheric Aerosols: Clouds, Chemistry, and Climate, *Annu. Rev. Chem. Biomol. Eng.*, *8*(1), 427-444, doi:10.1146/annurev-chembioeng-060816-101538.

Meier, J., B. Wehner, A. Massling, W. Birmili, A. Nowak, T. Gnauk, E. Brüggemann, H. Herrmann, H. Min, and A. Wiedensohler (2009), Hygroscopic growth of urban aerosol particles in Beijing (China) during wintertime: a comparison of three experimental methods, *Atmos. Chem. Phys.*, *9*(18), 6865-6880.

Meng, J., G. Wang, J. Li, C. Cheng, Y. Ren, Y. Huang, Y. Cheng, J. Cao, and T. Zhang (2014), Seasonal characteristics of oxalic acid and related SOA in the free troposphere of Mt. Hua, central China: Implications for sources and formation mechanisms, *Science of The Total Environment*, *493*, 1088-1097, doi:https://doi.org/10.1016/j.scitotenv.2014.04.086.

Moise, T., J. M. Flores, and Y. Rudich (2015), Optical Properties of Secondary Organic Aerosols and Their Changes by Chemical Processes, *Chem. Rev.*, *115*(10), 4400-4439, doi:10.1021/cr5005259.

Moosmüller, H., R. K. Chakrabarty, and W. P. Arnott (2009), Aerosol light absorption and its measurement: A review, *Journal of Quantitative Spectroscopy and Radiative Transfer*, *110*(11), 844-878, doi:https://doi.org/10.1016/j.jqsrt.2009.02.035.

Munger, J. W., D. J. Jacob, B. C. Daube, L. W. Horowitz, W. C. Keene, and B. G. Heikes (1995), Formaldehyde, glyoxal, and methylglyoxal in air and cloudwater at a rural mountain site in central Virginia, *J. Geophys. Res.*, *100*(D5), 9325-9333, doi:10.1029/95JD00508.

Murphy, J. G., P. K. Gregoire, A. G. Tevlin, G. R. Wentworth, R. A. Ellis, M. Z. Markovic, and T. C. VandenBoer (2017), Observational constraints on particle acidity using measurements and modelling of particles and gases, *Faraday Discuss.*, *200*(0), 379-395, doi:10.1039/C7FD00086C.

Nakao, S., P. Tang, X. Tang, C. H. Clark, L. Qi, E. Seo, A. Asa-Awuku, and D. Cocker (2013), Density and elemental ratios of secondary organic aerosol: Application of a density prediction method, *Atmos. Environ.*, *68*(Supplement C), 273-277, doi:https://doi.org/10.1016/j.atmosenv.2012.11.006.

National Academies of Sciences, E., and Medicine (2016), *The Future of Atmospheric Chemistry Research: Remembering Yesterday, Understanding Today, Anticipating Tomorrow*, 226 pp., The National Academies Press, Washington, DC, doi:doi:10.17226/23573.

Nguyen, T. B., P. B. Lee, K. M. Updyke, D. L. Bones, J. Laskin, A. Laskin, and S. A. Nizkorodov (2012), Formation of nitrogen- and sulfur-containing light-absorbing compounds accelerated by evaporation of water from secondary organic aerosols, *J. Geophys. Res.*, *117*(D1), n/a-n/a, doi:10.1029/2011JD016944.

Nozière, B., P. Dziedzic, and A. Córdova (2007), Formation of secondary light-absorbing "fulvic-like" oligomers: A common process in aqueous and ionic atmospheric particles?, *Geophys. Res. Lett.*, *34*(21), n/a-n/a, doi:10.1029/2007GL031300.

Nozière, B., M. Kalberer, M. Claeys, J. Allan, B. D'Anna, S. Decesari, E. Finessi, M. Glasius, I. Grgić, J. F. Hamilton, T. Hoffmann, Y. Iinuma, M. Jaoui, A. Kahnt, C. J. Kampf, I. Kourtchev, W. Maenhaut, N. Marsden, S. Saarikoski, J. Schnelle-Kreis, J. D. Surratt, S. Szidat, R. Szmigielski, and A. Wisthaler (2015), The Molecular Identification of Organic Compounds in the Atmosphere: State of the Art and Challenges, *Chem. Rev.*, *115*(10), 3919-3983, doi:10.1021/cr5003485.

Oudin, A., L. Bråbäck, D. O. Åström, M. Strömgren, and B. Forsberg (2016), Association between neighbourhood air pollution concentrations and dispensed medication for psychiatric disorders in a large longitudinal cohort of Swedish children and adolescents, *BMJ Open*, *6*(6), doi:10.1136/bmjopen-2015-010004.

Pan, Y., S. Tian, D. Liu, Y. Fang, X. Zhu, Q. Zhang, B. Zheng, G. Michalski, and Y. Wang (2016), Fossil Fuel Combustion-Related Emissions Dominate Atmospheric Ammonia

Sources during Severe Haze Episodes: Evidence from 15N-Stable Isotope in Size-Resolved Aerosol Ammonium, *Environ. Sci. Technol.*, *50*(15), 8049-8056, doi:10.1021/acs.est.6b00634.

Peng, J., M. Hu, S. Guo, Z. Du, J. Zheng, D. Shang, M. Levy Zamora, L. Zeng, M. Shao, Y.-S. Wu, J. Zheng, Y. Wang, C. R. Glen, D. R. Collins, M. J. Molina, and R. Zhang (2016), Markedly enhanced absorption and direct radiative forcing of black carbon under polluted urban environments, *Proc. Natl. Acad. Sci.*, *113*(16), 4266-4271, doi:10.1073/pnas.1602310113.

Phillips, S. M., and G. D. Smith (2014), Light Absorption by Charge Transfer Complexes in Brown Carbon Aerosols, *Environ. Sci. Technol. Lett.*, *1*(10), 382-386, doi:10.1021/ez500263j.

Pitchford, M., W. Malm, B. Schichtel, N. Kumar, D. Lowenthal, and J. Hand (2007), Revised Algorithm for Estimating Light Extinction from IMPROVE Particle Speciation Data, *J. Air & Waste Manage. Assoc.*, *57*(11), 1326-1336, doi:10.3155/1047-3289.57.11.1326.

Pope, C. A., R. T. Burnett, M. J. Thun, E. E. Calle, D. Krewski, K. Ito, and G. D. Thurston (2002), Lung Cancer, Cardiopulmonary Mortality, and Long-term Exposure to Fine Particulate Air Pollution, *JAMA : the journal of the American Medical Association*, *287*(9), 1132-1141.

Pope, C. A., and D. W. Dockery (2006), Health Effects of Fine Particulate Air Pollution: Lines that Connect, *J. Air & Waste Manage. Assoc.*, *56*(6), 709-742, doi:10.1080/10473289.2006.10464485.

Pöschl, U. (2005), Atmospheric Aerosols: Composition, Transformation, Climate and Health Effects, *Angew. Chem.-Int. Edit.*, *44*(46), 7520-7540, doi:10.1002/anie.200501122.

Powelson, M. H., B. M. Espelien, L. N. Hawkins, M. M. Galloway, and D. O. De Haan (2014), Brown Carbon Formation by Aqueous-Phase Carbonyl Compound Reactions with Amines and Ammonium Sulfate, *Environ. Sci. Technol.*, *48*(2), 985-993, doi:10.1021/es4038325.

Prather, K. A., C. D. Hatch, and V. H. Grassian (2008), Analysis of Atmospheric Aerosols, *Annu. Rev. Anal. Chem.*, *1*(1), 485-514, doi:10.1146/annurev.anchem.1.031207.113030.

116

Prenni, A. J., P. J. DeMott, S. M. Kreidenweis, D. E. Sherman, L. M. Russell, and Y. Ming (2001), The Effects of Low Molecular Weight Dicarboxylic Acids on Cloud Formation, *J. Phys. Chem. A*, *105*(50), 11240-11248, doi:10.1021/jp012427d.

Qiu, C., L. Wang, V. Lal, A. F. Khalizov, and R. Zhang (2011), Heterogeneous Reactions of Alkylamines with Ammonium Sulfate and Ammonium Bisulfate, *Environ. Sci. Technol.*, *45*(11), 4748-4755, doi:10.1021/es1043112.

Qiu, C., and R. Zhang (2013), Multiphase chemistry of atmospheric amines, *Phys. Chem. Chem. Phys.*, *15*(16), 5738-5752, doi:10.1039/C3CP43446J.

Quan, J., Q. Liu, X. Li, Y. Gao, X. Jia, J. Sheng, and Y. Liu (2015), Effect of heterogeneous aqueous reactions on the secondary formation of inorganic aerosols during haze events, *Atmos. Environ.*, *122*, 306-312, doi:https://doi.org/10.1016/j.atmosenv.2015.09.068.

Ramanathan, V., and Y. Feng (2009), Air pollution, greenhouse gases and climate change: Global and regional perspectives, *Atmos. Environ.*, *43*(1), 37-50, doi:https://doi.org/10.1016/j.atmosenv.2008.09.063.

Ramanathan, V., F. Li, M. V. Ramana, P. S. Praveen, D. Kim, C. E. Corrigan, H. Nguyen, E. A. Stone, J. J. Schauer, G. R. Carmichael, B. Adhikary, and S. C. Yoon (2007), Atmospheric brown clouds: Hemispherical and regional variations in long-range transport, absorption, and radiative forcing, *J. Geophys. Res.*, *112*(D22), n/a-n/a, doi:10.1029/2006JD008124.

Ravishankara, A. R. (1997), Heterogeneous and Multiphase Chemistry in the Troposphere, *Science*, *276*(5315), 1058-1065, doi:10.1126/science.276.5315.1058.

RenHe, Z., Q. Li, and R. Zhang (2014), Meteorological conditions for the persistent severe fog and haze event over eastern China in January 2013, *Science China Earth Sciences*, *57*(1), 26-35, doi:10.1007/s11430-013-4774-3.

Rosenfeld, D., U. Lohmann, G. B. Raga, C. D. O'Dowd, M. Kulmala, S. Fuzzi, A. Reissell, and M. O. Andreae (2008), Flood or Drought: How Do Aerosols Affect Precipitation?, *Science*, *321*(5894), 1309-1313, doi:10.1126/science.1160606.

Sareen, N., A. N. Schwier, E. L. Shapiro, D. Mitroo, and V. F. McNeill (2010), Secondary organic material formed by methylglyoxal in aqueous aerosol mimics, *Atmos. Chem. Phys.*, *10*(3), 997-1016.

Sarwar, G., K. Fahey, R. Kwok, R. C. Gilliam, S. J. Roselle, R. Mathur, J. Xue, J. Yu, and W. P. L. Carter (2013), Potential impacts of two SO2 oxidation pathways on regional sulfate concentrations: Aqueous-phase oxidation by NO2 and gas-phase oxidation by Stabilized Criegee Intermediates, *Atmos. Environ.*, *68*, 186-197, doi:https://doi.org/10.1016/j.atmosenv.2012.11.036.

Schlag, P., F. Rubach, T. F. Mentel, D. Reimer, F. Canonaco, J. S. Henzing, M. Moerman, R. Otjes, A. S. H. Prevot, F. Rohrer, B. Rosati, R. Tillmann, E. Weingartner, and A. Kiendler-Scharr (2017), Ambient and laboratory observations of organic ammonium salts in PM1, *Faraday Discuss.*, *200*(0), 331-351, doi:10.1039/C7FD00027H.

Schlesinger, R. B., N. Kunzli, G. M. Hidy, T. Gotschi, and M. Jerrett (2006), The Health Relevance of Ambient Particulate Matter Characteristics: Coherence of Toxicological and Epidemiological Inferences, *Inhalation Toxicology*, *18*(2), 95-125, doi:10.1080/08958370500306016.

Sedehi, N., H. Takano, V. A. Blasic, K. A. Sullivan, and D. O. De Haan (2013), Temperature- and pH-dependent aqueous-phase kinetics of the reactions of glyoxal and methylglyoxal with atmospheric amines and ammonium sulfate, *Atmos. Environ.*, *77*(Supplement C), 656-663, doi:https://doi.org/10.1016/j.atmosenv.2013.05.070.

Seinfeld, J. H., and S. N. Pandis (2006), *Atmospheric Chemistry and Physics: From Air Pollution to Climate Change*, Wiley.

Shapiro, E. L., J. Szprengiel, N. Sareen, C. N. Jen, M. R. Giordano, and V. F. McNeill (2009), Light-absorbing secondary organic material formed by glyoxal in aqueous aerosol mimics, *Atmos. Chem. Phys.*, *9*(7), 2289-2300.

Shen, X., Y. Zhao, Z. Chen, and D. Huang (2013), Heterogeneous reactions of volatile organic compounds in the atmosphere, *Atmos. Environ.*, *68*, 297-314, doi:https://doi.org/10.1016/j.atmosenv.2012.11.027.

Shiraiwa, M., M. Ammann, T. Koop, and U. Pöschl (2011), Gas uptake and chemical aging of semisolid organic aerosol particles, *Proc. Natl. Acad. Sci.*, *108*(27), 11003-11008, doi:10.1073/pnas.1103045108.

Shiraiwa, M., Y. Li, A. P. Tsimpidi, V. A. Karydis, T. Berkemeier, S. N. Pandis, J. Lelieveld, T. Koop, and U. Pöschl (2017), Global distribution of particle phase state in atmospheric secondary organic aerosols, *Nature Communications*, *8*, 15002, doi:10.1038/ncomms15002
https://www.nature.com/articles/ncomms15002#supplementary-information.

Shiraiwa, M., C. Pfrang, T. Koop, U. Pöschl, and N. M. Donahue (2012), Kinetic multi-layer model of gas-particle interactions in aerosols and clouds (KM-GAP): linking condensation, evaporation and chemical reactions of organics, oxidants and water, *Atmos. Chem. Phys.*, *12*(5), 2777-2794, doi:10.5194/acp-12-2777-2012.

Shrivastava, M., C. D. Cappa, J. Fan, A. H. Goldstein, A. B. Guenther, J. L. Jimenez, C. Kuang, A. Laskin, S. T. Martin, N. L. Ng, T. Petaja, J. R. Pierce, P. J. Rasch, P. Roldin, J. H. Seinfeld, J. Shilling, J. N. Smith, J. A. Thornton, R. Volkamer, J. Wang, D. R. Worsnop, R. A. Zaveri, A. Zelenyuk, and Q. Zhang (2017), Recent advances in understanding secondary organic aerosol: Implications for global climate forcing, *Reviews of Geophysics*, *55*(2), 509-559, doi:10.1002/2016RG000540.

Smith, J. N., K. C. Barsanti, H. R. Friedli, M. Ehn, M. Kulmala, D. R. Collins, J. H. Scheckman, B. J. Williams, and P. H. McMurry (2010), Observations of aminium salts in atmospheric nanoparticles and possible climatic implications, *Proc. Natl. Acad. Sci.*, *107*(15), 6634-6639, doi:10.1073/pnas.0912127107.

Spaulding, R. S., G. W. Schade, A. H. Goldstein, and M. J. Charles (2003), Characterization of secondary atmospheric photooxidation products: Evidence for biogenic and anthropogenic sources, *J. Geophys. Res.*, *108*(D8), n/a-n/a, doi:10.1029/2002JD002478.

Srám, R. (1999), Impact of air pollution on reproductive health, *Environ. Health Perspect.*, *107*(11), A542-A543.

Stein, A.F., Draxler, R.R, Rolph, G.D., Stunder, B.J.B., Cohen, M.D., and Ngan, F., (2015). NOAA's HYSPLIT atmospheric transport and dispersion modeling system, *Bull. Amer. Meteor. Soc., 96*, 2059-2077, http://dx.doi.org/10.1175/BAMS-D-14-00110.1

Sun, Y. L., Z. F. Wang, P. Q. Fu, T. Yang, Q. Jiang, H. B. Dong, J. Li, and J. J. Jia (2013), Aerosol composition, sources and processes during wintertime in Beijing, China, *Atmos. Chem. Phys.*, *13*(9), 4577-4592, doi:10.5194/acp-13-4577-2013.

Tao, J., L. Zhang, J. Cao, and R. Zhang (2017), A review of current knowledge concerning PM2. 5 chemical composition, aerosol optical properties and their relationships across China, *Atmos. Chem. Phys.*, *17*(15), 9485-9518, doi:10.5194/acp-17-9485-2017.

Thalladi, V. R., M. Nüsse, and R. Boese (2000), The Melting Point Alternation in α,ω-Alkanedicarboxylic Acids, *J. Am. Chem. Soc.*, *122*(38), 9227-9236, doi:10.1021/ja0011459.

Tie, X., S. Madronich, S. Walters, R. Zhang, P. Rasch, and W. Collins (2003), Effect of clouds on photolysis and oxidants in the troposphere, *J. Geophys. Res.*, *108*(D20), n/a-n/a, doi:10.1029/2003JD003659.

U.S. Department of State (2018), Mission China air quality monitoring program, edited.

Volkamer, R., J. L. Jimenez, F. San Martini, K. Dzepina, Q. Zhang, D. Salcedo, L. T. Molina, D. R. Worsnop, and M. J. Molina (2006), Secondary organic aerosol formation from anthropogenic air pollution: Rapid and higher than expected, *Geophys. Res. Lett.*, *33*(17), n/a-n/a, doi:10.1029/2006GL026899.

Volkamer, R., F. San Martini, L. T. Molina, D. Salcedo, J. L. Jimenez, and M. J. Molina (2007), A missing sink for gas-phase glyoxal in Mexico City: Formation of secondary organic aerosol, *Geophys. Res. Lett.*, *34*(19), n/a-n/a, doi:10.1029/2007GL030752.

von Schneidemesser, E., P. S. Monks, J. D. Allan, L. Bruhwiler, P. Forster, D. Fowler, A. Lauer, W. T. Morgan, P. Paasonen, M. Righi, K. Sindelarova, and M. A. Sutton (2015), Chemistry and the Linkages between Air Quality and Climate Change, *Chem. Rev.*, *115*(10), 3856-3897, doi:10.1021/acs.chemrev.5b00089.

Wang, G., K. Kawamura, N. Umemoto, M. Xie, S. Hu, and Z. Wang (2009), Water-soluble organic compounds in PM2.5 and size-segregated aerosols over Mount Tai in North China Plain, *J. Geophys. Res.*, *114*(D19), n/a-n/a, doi:10.1029/2008JD011390.

Wang, G., K. Kawamura, T. Watanabe, S. Lee, K. Ho, and J. Cao (2006a), High loadings and source strengths of organic aerosols in China, *Geophys. Res. Lett.*, *33*(22), n/a-n/a, doi:10.1029/2006GL027624.

Wang, G., M. Xie, S. Hu, S. Gao, E. Tachibana, and K. Kawamura (2010a), Dicarboxylic acids, metals and isotopic compositions of C and N in atmospheric aerosols from inland China: implications for dust and coal burning emission and secondary aerosol formation, *Atmos. Chem. Phys.*, *10*(13), 6087-6096, doi:10.5194/acp-10-6087-2010.

Wang, G., R. Zhang, M. E. Gomez, L. Yang, M. Levy Zamora, M. Hu, Y. Lin, J. Peng, S. Guo, J. Meng, J. Li, C. Cheng, T. Hu, Y. Ren, Y. Wang, J. Gao, J. Cao, Z. An, W. Zhou, G. Li, J. Wang, P. Tian, W. Marrero-Ortiz, J. Secrest, Z. Du, J. Zheng, D. Shang, L. Zeng, M. Shao, W. Wang, Y. Huang, Y. Wang, Y. Zhu, Y. Li, J. Hu, B. Pan, L. Cai, Y. Cheng, Y. Ji, F. Zhang, D. Rosenfeld, P. S. Liss, R. A. Duce, C. E. Kolb, and M. J. Molina (2016), Persistent sulfate formation from London Fog to Chinese haze, *Proc. Natl. Acad. Sci.*, *113*(48), 13630-13635, doi:10.1073/pnas.1616540113.

Wang, G., B. Zhou, C. Cheng, J. Cao, J. Li, J. Meng, J. Tao, R. Zhang, and P. Fu (2013a), Impact of Gobi desert dust on aerosol chemistry of Xi'an, inland China during spring 2009: differences in composition and size distribution between the urban ground surface and the mountain atmosphere, *Atmos. Chem. Phys.*, *13*(2), 819.

Wang, J., Y.-H. Zhang, M. Shao, X.-L. Liu, L.-M. Zeng, C.-L. Cheng, and X.-F. Xu (2006b), *Quantitative relationship between visibility and mass concentration of PM2.5 in Beijing*, 475-481 pp.

Wang, L., A. F. Khalizov, J. Zheng, W. Xu, Y. Ma, V. Lal, and R. Zhang (2010b), Atmospheric nanoparticles formed from heterogeneous reactions of organics, *Nature Geoscience*, *3*, 238, doi:10.1038/ngeo778
https://www.nature.com/articles/ngeo778#supplementary-information.

Wang, Y., M. Hu, P. Lin, Q. Guo, Z. Wu, M. Li, L. Zeng, Y. Song, L. Zeng, Y. Wu, S. Guo, X. Huang, and L. He (2017a), Molecular Characterization of Nitrogen-Containing Organic Compounds in Humic-like Substances Emitted from Straw Residue Burning, *Environ. Sci. Technol.*, *51*(11), 5951-5961, doi:10.1021/acs.est.7b00248.

Wang, Y., A. Khalizov, M. Levy, and R. Zhang (2013b), New Directions: Light absorbing aerosols and their atmospheric impacts, *Atmos. Environ.*, *81*(Supplement C), 713-715, doi:https://doi.org/10.1016/j.atmosenv.2013.09.034.

Wang, Y., Q. Zhang, J. Jiang, W. Zhou, B. Wang, K. He, F. Duan, Q. Zhang, S. Philip, and Y. Xie (2014), Enhanced sulfate formation during China's severe winter haze episode in January 2013 missing from current models, *J. Geophys. Res.*, *119*(17), 10,425-410,440, doi:10.1002/2013JD021426.

Wang, Z., Z. Wu, D. Yue, D. Shang, S. Guo, J. Sun, A. Ding, L. Wang, J. Jiang, H. Guo, J. Gao, H. C. Cheung, L. Morawska, M. Keywood, and M. Hu (2017b), New particle formation in China: Current knowledge and further directions, *Science of The Total Environment*, *577*, 258-266, doi:https://doi.org/10.1016/j.scitotenv.2016.10.177.

Wang, Z. B., M. Hu, X. Y. Pei, R. Y. Zhang, P. Paasonen, J. Zheng, D. L. Yue, Z. J. Wu, M. Boy, and A. Wiedensohler (2015), Connection of organics to atmospheric new particle formation and growth at an urban site of Beijing, *Atmos. Environ.*, *103*, 7-17, doi:https://doi.org/10.1016/j.atmosenv.2014.11.069.

Wang, Z. B., M. Hu, D. L. Yue, J. Zheng, R. Y. Zhang, A. Wiedensohler, Z. J. Wu, T. Nieminen, and M. Boy (2011), Evaluation on the role of sulfuric acid in the mechanisms of new particle formation for Beijing case, *Atmos. Chem. Phys.*, *11*(24), 12663-12671, doi:10.5194/acp-11-12663-2011.

Washenfelder, R. A., J. M. Flores, C. A. Brock, S. S. Brown, and Y. Rudich (2013), Broadband measurements of aerosol extinction in the ultraviolet spectral region, *Atmos. Meas. Tech.*, *6*(4), 861-877, doi:10.5194/amt-6-861-2013.

Wu, Z., M. Hu, P. Lin, S. Liu, B. Wehner, and A. Wiedensohler (2008), Particle number size distribution in the urban atmosphere of Beijing, China, *Atmos. Environ.*, *42*(34), 7967-7980, doi:https://doi.org/10.1016/j.atmosenv.2008.06.022.

Wu, Z., M. Hu, S. Liu, B. Wehner, S. Bauer, A. Ma ßling, A. Wiedensohler, T. Petäjä, M. Dal Maso, and M. Kulmala (2007), New particle formation in Beijing, China: Statistical analysis of a 1-year data set, *J. Geophys. Res.*, *112*(D9), n/a-n/a, doi:10.1029/2006JD007406.

Xie, Y., A. Ding, W. Nie, H. Mao, X. Qi, X. Huang, Z. Xu, V.-M. Kerminen, T. Petäjä, X. Chi, A. Virkkula, M. Boy, L. Xue, J. Guo, J. Sun, X. Yang, M. Kulmala, and C. Fu (2015), Enhanced sulfate formation by nitrogen dioxide: Implications from in situ observations at the SORPES station, *J. Geophys. Res.*, *120*(24), 12679-12694, doi:10.1002/2015JD023607.

Xu, W., M. Gomez-Hernandez, S. Guo, J. Secrest, W. Marrero-Ortiz, A. L. Zhang, and R. Zhang (2014), Acid-Catalyzed Reactions of Epoxides for Atmospheric Nanoparticle Growth, *J. Am. Chem. Soc.*, *136*(44), 15477-15480, doi:10.1021/ja508989a.

Yao, L., W. Ming-Yi, W. Xin-Ke, L. Yi-Jun, C. Hang-Fei, J. Zheng, W. Nie, D. Ai-Jun, F.-H. Geng, and W. Dong-Fang (2016), Detection of atmospheric gaseous amines and amides by a high-resolution time-of-flight chemical ionization mass spectrometer with protonated ethanol reagent ions, *Atmos. Chem. Phys.*, *16*(22), 14527.

Yu, G., A. R. Bayer, M. M. Galloway, K. J. Korshavn, C. G. Fry, and F. N. Keutsch (2011), Glyoxal in Aqueous Ammonium Sulfate Solutions: Products, Kinetics and Hydration Effects, *Environ. Sci. Technol.*, *45*(15), 6336-6342, doi:10.1021/es200989n.

Yuan, J.-F., X.-F. Huang, L.-M. Cao, J. Cui, Q. Zhu, C.-N. Huang, Z.-J. Lan, and L.-Y. He (2016), Light absorption of brown carbon aerosol in the PRD region of China, *Atmos. Chem. Phys.*, *16*(3), 1433-1443.

Yue, D., M. Hu, R. Zhang, Z. Wang, J. Zheng, Z. Wu, A. Wiedensohler, L. He, X. Huang, and T. Zhu (2010), The roles of sulfuric acid in new particle formation and growth in the mega-city of Beijing, *Atmos. Chem. Phys.*, *10*(10), 4953-4960.

Zarzana, K. J., C. D. Cappa, and M. A. Tolbert (2014), Sensitivity of Aerosol Refractive Index Retrievals Using Optical Spectroscopy, *Aerosol Sci. Technol.*, *48*(11), 1133-1144, doi:10.1080/02786826.2014.963498.

Zarzana, K. J., D. O. De Haan, M. A. Freedman, C. A. Hasenkopf, and M. A. Tolbert (2012), Optical Properties of the Products of α-Dicarbonyl and Amine Reactions in Simulated Cloud Droplets, *Environ. Sci. Technol.*, *46*(9), 4845-4851, doi:10.1021/es2040152.

Zhang, D., and R. Zhang (2005), Laboratory Investigation of Heterogeneous Interaction of Sulfuric Acid with Soot, *Environ. Sci. Technol.*, *39*(15), 5722-5728, doi:10.1021/es050372d.

Zhang, Q., and C. Anastasio (2003), Free and combined amino compounds in atmospheric fine particles (PM2.5) and fog waters from Northern California, *Atmos. Environ.*, *37*(16), 2247-2258, doi:https://doi.org/10.1016/S1352-2310(03)00127-4.

Zhang, Q., F. Duan, K. He, Y. Ma, H. Li, T. Kimoto, and A. Zheng (2015a), Organic nitrogen in PM2.5 in Beijing, *Frontiers of Environmental Science & Engineering*, *9*(6), 1004-1014, doi:10.1007/s11783-015-0799-5.

Zhang, Q., J. Zhang, and H. Xue (2010), The challenge of improving visibility in Beijing, *Atmos. Chem. Phys.*, *10*(16), 7821-7827.

Zhang, R. (2010), Getting to the Critical Nucleus of Aerosol Formation, *Science*, *328*(5984), 1366-1367, doi:10.1126/science.1189732.

Zhang, R., J. T. Jayne, and M. J. Molina (1994), Heterogeneous interactions of nitryl hypochlorite and hydrogen chloride with sulfuric acid tetrahydrate: implications for the stratosphere, *J. Phys. Chem.*, *98*(3), 867-874, doi:10.1021/j100054a022.

Zhang, R., A. Khalizov, L. Wang, M. Hu, and W. Xu (2012), Nucleation and Growth of Nanoparticles in the Atmosphere, *Chem. Rev.*, *112*(3), 1957-2011, doi:10.1021/cr2001756.

Zhang, R., A. F. Khalizov, J. Pagels, D. Zhang, H. Xue, and P. H. McMurry (2008), Variability in morphology, hygroscopicity, and optical properties of soot aerosols during atmospheric processing, *Proc. Natl. Acad. Sci.*, *105*(30), 10291-10296, doi:10.1073/pnas.0804860105.

Zhang, R., P. Tian, Y. Ji, Y. Lin, J. Peng, B. Pan, Y. Wang, G. Wang, G. Li, W. Wang, F. Zhang, X. Feng, L. Duan, J. Hu, W. Marrero-Ortiz, J. Secrest, and M. Hu (2017),

Overview of Persistent Haze Events in China, in *Air Pollution in Eastern Asia: An Integrated Perspective*, edited by I. Bouarar, X. Wang and G. P. Brasseur, pp. 3-25, Springer International Publishing, Cham, doi:10.1007/978-3-319-59489-7_1.

Zhang, R., G. Wang, S. Guo, M. L. Zamora, Q. Ying, Y. Lin, W. Wang, M. Hu, and Y. Wang (2015b), Formation of Urban Fine Particulate Matter, *Chem. Rev.*, *115*(10), 3803-3855, doi:10.1021/acs.chemrev.5b00067.

Zhang, X., L. Wu, R. Zhang, S. Deng, Y. Zhang, J. Wu, Y. Li, L. Lin, L. Li, Y. Wang, and L. Wang (2013), Evaluating the relationships among economic growth, energy consumption, air emissions and air environmental protection investment in China, *Renewable and Sustainable Energy Reviews*, *18*, 259-270, doi:https://doi.org/10.1016/j.rser.2012.10.029.

Zhao, J., N. P. Levitt, R. Zhang, and J. Chen (2006), Heterogeneous Reactions of Methylglyoxal in Acidic Media: Implications for Secondary Organic Aerosol Formation, *Environ. Sci. Technol.*, *40*(24), 7682-7687, doi:10.1021/es060610k.

Zhao, J., R. Zhang, K. Misawa, and K. Shibuya (2005), Experimental product study of the OH-initiated oxidation of m-xylene, *Journal of Photochemistry and Photobiology A: Chemistry*, *176*(1), 199-207, doi:https://doi.org/10.1016/j.jphotochem.2005.07.013.

Zheng, G., F. Duan, H. Su, Y. Ma, Y. Cheng, B. Zheng, Q. Zhang, T. Huang, T. Kimoto, and D. Chang (2015), Exploring the severe winter haze in Beijing: the impact of synoptic weather, regional transport and heterogeneous reactions, *Atmos. Chem. Phys.*, *15*(6), 2969-2983.

Zhu, C.-S., J.-J. Cao, K.-F. Ho, L. W. Antony Chen, R.-J. Huang, Y.-C. Wang, H. Li, Z.-X. Shen, J. C. Chow, J. G. Watson, X.-l. Su, Q.-y. Wang, and S. Xiao (2015), The optical properties of urban aerosol in northern China: A case study at Xi'an, *Atmos. Res.*, *160*, 59-67, doi:https://doi.org/10.1016/j.atmosres.2015.03.008.